INVESTIGATION OF THE OPTICAL PROPERTIES, COMPOSITION AND LOCAL STRUCTURE OF InGaN

A Thesis Submitted to

The Department of Physics and Applied Physics

University of Strathclyde

For the Degree of

Doctor of Philosophy

By

Madeleine Eve White

April 2002

DECLARATION OF AUTHOR'S RIGHTS

ABSTRACT

This thesis presents work on the optical properties, composition and local structure of InGaN. Low temperature photoluminescence (PL) spectroscopy of InGaN epilayers was used to study linewidth, intensity and uniformity of the samples. Temperature dependence of the PL spectrum showed a decrease in the peak emission energy with increasing temperature for one epilayer sample and an 'S'-shape temperature dependence of peak emission energy for a second sample. Composition analysis of the epilayers using three different experimental techniques; Rutherford backscattering spectrometry (RBS), electron probe microanalysis (EPMA) and extended X-ray absorption fine structure (EXAFS), found that the indium nitride fraction varies linearly with the PL peak emission energy. Confocal microscopy of InGaN epilayer, quantum well (QW) and quantum box (QB) samples revealed that InGaN luminescence segregates into bright and dark spots, ~1μm in diameter, and indicates that the origin of InGaN luminescence is of sub μm-scale. InGaN local structure parameters were derived from EXAFS measurements. Epilayer samples exhibited a single-phase InGaN alloy while a QB sample showed a two-phase mixture of components, one of which is nearly pure InN. Photoluminescence excitation (PLE) spectroscopy on MOCVD epilayers and MBE QWs and QBs showed that the bandgap energy varies linearly with detected emission energy for an individual sample. The PLE results from the MOCVD samples were consistent with data taken using optical absorption spectroscopy. Two different linear relationships between Stokes' shift and detected emission energy were obtained for the MOCVD and MBE samples.

Analysis of the accumulated results suggests that InGaN luminescence may be related to the combined effects of exciton localisation in InN-rich QDs, formed as a result of phase segregation in InGaN, accompanied by strain-induced piezoelectric fields.

ACKNOWLEDGEMENTS

There are many people to whom I would like to extend my gratitude for their help and patience during my time at the University of Strathclyde.

Firstly, thanks go to my supervisor Professor Kevin O'Donnell for sharing his extensive knowledge of III-nitrides and semiconductor physics and for his guidance throughout the course of my PhD. I am also grateful to Dr Robert Martin for his help and useful discussions as well as to our collaborators at the Daresbury Laboratories, Warrington, University of Leuven, Belgium, University of Montpellier, France and to the many different crystal growers, without whom there would be no samples to test.

Many thanks are also due to all members of 'level 2', past and present, in particular to Carol, Dave, Paul, Frank and Raúl. Thanks to Dr. Carol Trager-Cowan for her great company during our conference trips abroad and her extreme enthusiasm for physics. I cannot thank enough Dave Clark and Jim Barrie for all their expertise, time and great patience, as I systematically broke most pieces of equipment in the lab. To Paul Edwards, Francis Sweeney and Raúl Pecharromán-Gallego, thanks for all their help and more importantly their friendship. Special thanks go to Paul for proof reading this thesis and for letting me share his office during the thesis write up.

On a more personal note, I would like to thank Gail McConnell and Justyna Zawadzka. Their essential cups of tea and gossip sessions, which I still hope to continue when we have long-since departed University, were as enjoyable and valuable as our friendships.

Lastly, but most importantly I would like to thank all my friends and family, especially my mum and big brother Eric. Without their love and encouragement I would never have continued or ever completed my studies.

Thanks again to all involved and apologies to anyone not mentioned by name, believe me your contribution to this thesis is greatly appreciated!!!

Madeleine Eve White

April 2002

TABLE OF CONTENTS

CHAPTER 3: EXPERIMENTAL PROCEDURES

CHAPTER 1: INTRODUCTION

1.1 General Introduction to III-Nitrides

In this thesis the luminescence properties, composition and local structure of the III-nitride material InGaN will be described. There has been much interest in III-nitrides over the past decade. Efficient luminescence and the high melting points of these materials make them ideal for use in optoelectronic devices and high temperature transistors. III-nitride materials include the binary compounds aluminum, gallium and indium nitrides, AlN, GaN and InN respectively. This work looks at the ternary alloy of GaN and InN, InGaN. Other III-nitride ternary alloys such as AlGaN and quarternary alloys such as InGaAsN can also be produced.

The large tunable optical bandgap of the III-nitrides mean they can be used in applications across the entire visible spectrum. However, they are primarily used at present to make devices that emit in the blue and violet. Applications of III-nitride optoelectronics range from: light emitters in full colour displays [1], laser diodes in high-density information storage systems [1] and high-speed electronic field effect transistor (FET) structures in RF/microwave power amplifiers [2]. If the current upward trend in the fortunes of these materials continues, then it is predicted that by the year 2009, III-nitrides will be a $4.8 billion industry [3].

1.2 History of III-Nitrides

III-nitride materials do not occur naturally, they must be artificially produced. The development of the material can be traced back to 1938, when attempts were first made by Juza and Hahn to synthesize GaN by passing ammonia over gallium at high temperature (>800°C) [4]. Small micron-sized GaN needles and platelets were grown. Grimmeiss et al. used the same method in 1959 to obtain small crystals of GaN on which the first photoluminescence (PL) spectroscopy measurements were taken [5].

In 1969, Maruska and Tietjen, assistants of Professor Jacques Pankove at RCA Laboratories, became the first to grow large area GaN layers by depositing GaN onto sapphire using hydride vapour phase epitaxy (HVPE) [6]. The material produced provided the first good electrical and optical evaluation of the compound. The direct energy optical bandgap of GaN was determined to be ~3.39eV at room temperature and the material was n-type with electron concentrations typically above $10^{19}/cm^3$ [6]. GaN was now considered a potential material for optoelectronic devices. Many important studies in GaN were carried out at this time, including surface acoustic wave generation [7], fabrication of solar blind UV detectors [8] and optical gain measurements to study stimulated emission from GaN crystals [9].

Unfortunately, the poor quality of the HVPE material hindered research progress, since many experimental results were found to be irreproducible. With the development of GaN growth using molecular beam epitaxy (MBE) and metallorganic chemical vapour deposition (MOCVD) the material quality improved.

In 1983 good quality MBE growth of GaN epilayers was achieved by Yoshida et al. [10] who deposited an AlN buffer layer between the GaN film and the sapphire substrate. The quality of the GaN improved because the buffer layer reduced the high strain lattice mismatch between the GaN and sapphire. This promotes two-dimensional growth of good quality GaN at high temperature (1050°C). By 1986, Akasaki and Amano had refined this technique for MOCVD growth [11]. In 1989, the same team produced the first p-type GaN. After scanning magnesium doped GaN with an electron beam, they found parts of the sample to be conducting [12].

On November 29th 1993, Nichia Chemical Industries announced the development of the world's first high brightness InGaN blue LED. Nichia researcher Shuji Nakamura and co-workers quickly took the lead; developing the world's first InGaN green LED in 1994, InGaN violet laser diode in 1995, InGaN-based white LED in 1996 and InGaN yellow LED in 1998 [13]. A selection of commercially available Nichia InGaN LEDs is shown in Figure 1.1 [14].

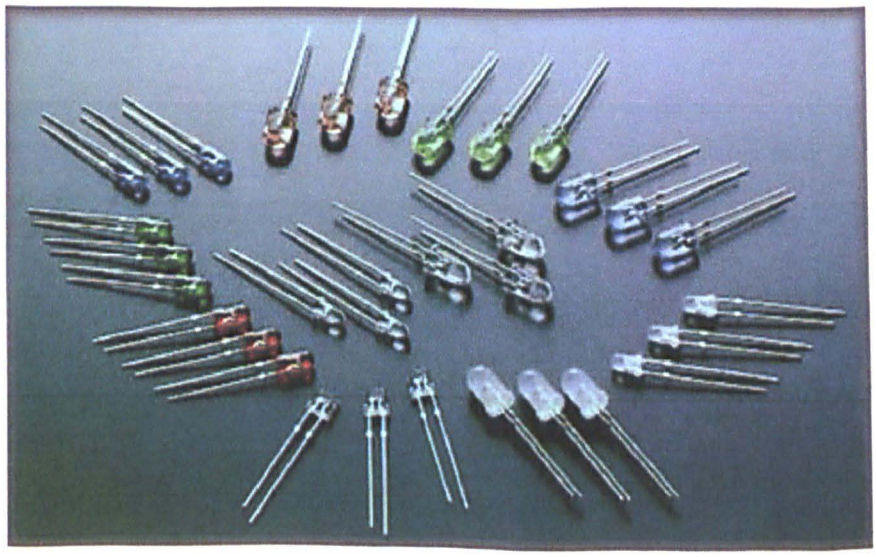

Figure 1.1: Nichia LEDs

By 1999 Nichia also became the world's only commercial supplier of InGaN LDs [13]. At the time of writing, 7 other major companies produce InGaN LEDs in addition to Nichia. These companies are Sony, Toyoda Gosei, Osram, Cree, GELcore, LumiLEDs and Rohm.

1.3 Current Applications and Recent Developments in III-Nitrides

Lighting is the most important and well-known application of III-nitride devices. GaN and InGaN LEDs are used to make full colour, high resolution, and high intensity graphic displays. InGaN LEDs have also found use in traffic lighting, as shown in Figure 1.2.

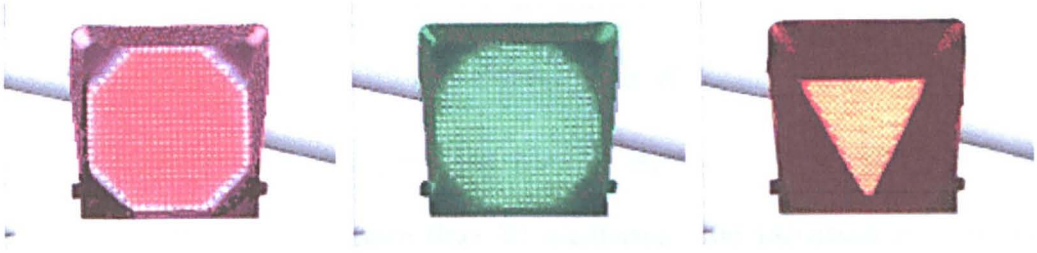

Figure 1.2: T. T. I. LED traffic lights in operation.

Companies, such as Traffic Technologies Inc. (T.T.I), are so confident as to the cost efficiency of using LEDs in place of incandescent lighting, that they have offered free LED traffic lights to every city in America [15]. The only condition on the offer is that the money saved in power costs is paid back to T.T.I for the next five years. This saving is estimated to be approximately $110 per year, per unit, and over $570 per year in maintenance costs. Reduction in the power costs is due to the high efficiencies of LEDs compared to conventional lighting sources. In a comparative

study of a 70W incandescent light bulb and 120 Nichia LEDs, the array of LEDs consumed only 8.6W. In addition, LEDs offer further benefits due to their robustness, reliability and long lifetime [16].

III-nitride LEDs are also used as a UV curing source in dentistry [17], as a true blue light source in colour scanners and colour facsimile machines and in car dashboard displays and mobile phone backlighting [18].

III-nitride LDs are currently under development for new optical data storage systems. InGaN LDs are beginning to replace the 650nm AlInGaP LDs in today's Digital Versatile Disc (DVD) players [13]. The shorter wavelength of GaN and InGaN LDs produces a smaller spot on the surface of the disc which means more information can be read or written on a given area. By using the new Nichia violet LDs manufacturers hope to expand the storage capacity of next generation DVD discs from 4.7 gigabytes to more than 20 gigabytes. The increased storage would allow each DVD disc to hold up to 10 hours of video data as opposed to the current 2 hours [13].

III-nitride LDs are also to be found in laser printers and scanners, computer video games and underwater optical communications systems.

We conclude this section with highlights from the Fourth International Conference on Nitride Semiconductors (ICNS-4). This was held in Denver, Colorado in July

2001. The conference ended with a session of talks covering some of the very latest developments in the III-nitride field. Toyoda Gosei discussed their new GaN-based UV LEDs for use in deodorising air cleaners, yet another application of III-nitride devices. Air passed through UV light to kill bacteria and viruses has been found to be much cleaner than air passed through carbon filters [19]. Nichia discussed their new GaN-based LEDs and LDs, including a UV LD with a single quantum well GaN active layer grown on an ELOG substrate, the first of its type grown. The UV LD operates at room temperature with an output power of 2mW and has a lifetime of ~ 2000 hours [20]. LumiLEDs closed the conference with an impressive light show of their new 1000mW 'powerLEDs'. These 'powerLEDs' have an external quantum efficiency up to 40% greater than those previously manufactured [21].

1.4 InGaN

Despite the technological advances made in luminescent III-nitrides, the underlying physics of the light-emitting material is not yet fully understood. Most of the III-nitrides devices described in Section 1.3 incorporate InGaN, the material studied in this thesis. Although there has been a great deal of research on its optical properties, there is a lot of uncertainty surrounding the structure and ordering of InGaN. In particular, the relationship between nanostructure and the optical properties is unclear. In this work, the optical properties are correlated with measurements taken to determine the composition and investigate local structure. The results of these measurements are discussed with an aim to provide a better understanding as to the origin of InGaN luminescence.

1.4.1 The Optical Properties of InGaN

InGaN is ideal for use in optoelectronic applications because the optical bandgap of $In_xGa_{(1-x)}N$ alloys covers the visible spectrum from UV (GaN) to red (InN). InGaN LEDs that emit across the entire range of the visible spectrum are currently mass-produced [14] and are already used in many different applications. By varying the indium/gallium ratio, determined in the alloy formula by x where $0 \leq x \leq 1$, the optical bandgap of the material can be controlled between that of GaN and InN.

The optical bandgap of GaN is found to be ~3.39eV [6,22], while the optical bandgap of InN has proved more difficult to define. A standard value of ~1.89eV is generally accepted to be the bandgap of InN [23]. However, Inushima et al. have determined the bandgap to be ~1.1eV from transmission measurements of InN [24] and more recently Davydov et al. calculated the bandgap to be as low as ~0.7eV, on analysis of PL data taken from single crystalline InN material [25]. A luminescence band from InN previously measured by Inushima et al. was centered ~1.86eV at 14K [26] and from Davydov et al. luminescence was seen in the range of 0.75eV to 0.9eV at 77K [27].

There has also been much confusion in determining the composition of InGaN. Early measurements, based upon X-ray diffraction (XRD) measurements of the lattice constant by Nakamura [28,29], appear to overestimate the indium nitride fraction for a given emission energy by a factor of approximately two.

Both of these points will be addressed in this thesis.

1.4.2 InGaN – a direct bandgap semiconductor

One important requirement of materials to be used in light emitting devices is to have a direct bandgap. In a direct bandgap semiconductor, the minimum energy level in the conduction band and the maximum energy level in the valence band occur at the same value of pseudomomentum, **k**.

An electron in the conduction band relaxes non-radiatively to the minimum energy level of the band at $\mathbf{k} = 0$. This electron may have been excited either optically, by a photon with sufficient energy to bridge the gap between the valence and the conduction band, or electrically by current injection. The electron can then recombine with a hole, which has relaxed to the top of the valence band, as shown in Figure 1.3a). Energy released during this recombination is radiative.

If a material has an indirect bandgap, the electrons and holes relax to energy minima that have different values of momentum. As momentum has to be conserved in band-to-band transitions, recombination is less likely to occur. Phonon assisted recombination may take place whereby a phonon with adequate momentum can provide enough energy for recombination, as shown in Figure 1.3b). Unfortunately this relies on a suitable passing phonon; meanwhile the electron may encounter a defect or become trapped. As a result of this, luminescence from indirect bandgap materials can be quenched [30]. Direct bandgap materials are therefore much more desirable for use in optoelectronics devices.

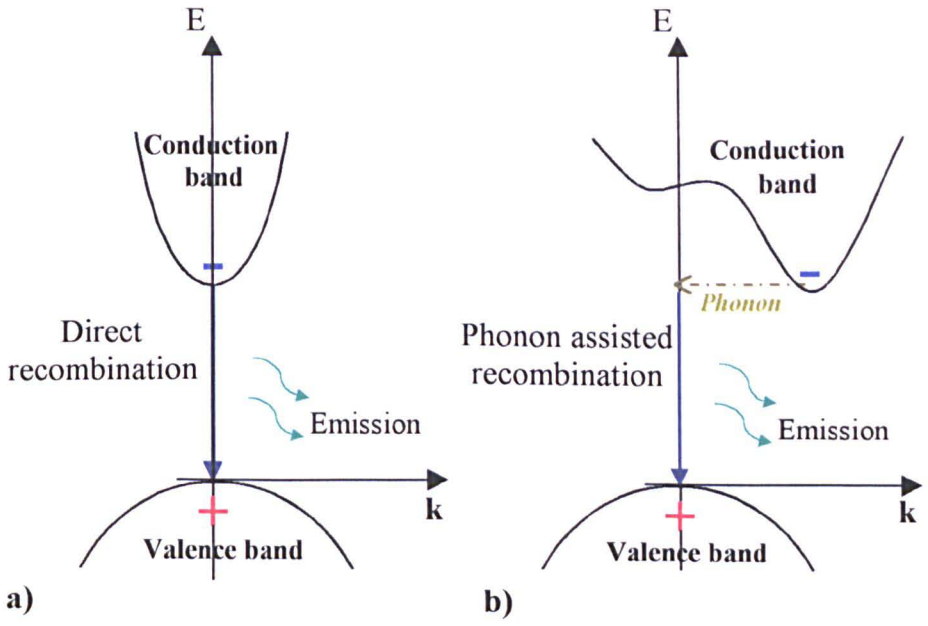

Figure 1.3: Simplified band diagram of a) direct and b) indirect bandgap recombination.

Luminescence from a direct bandgap material can also be influenced by defects. As the excited electron has a non-zero radiative lifetime, it may become trapped by a defect before radiative recombination has had a chance to occur.

1.4.3 Luminescence, defects and growth of InGaN

The radiative quantum efficiency of InGaN is surprisingly good despite its high defect density. Microscopic images show an extremely high number of dislocations and defects, far higher than could be tolerated in any other III-V or II-VI material system [31].

The poor quality of InGaN material is mainly due to the unavailability of a suitable substrate for growth. The substrate generally used is sapphire, Al_2O_3, although others being investigated include silicon carbide, zinc oxide and bulk GaN. Due to

high costs or growth problems associated with these alternatives, sapphire remains the most common nitride substrate to-date. Sapphire is not an ideal substrate material for InGaN because of its large lattice mismatch and high thermal mismatch with the III-nitrides. During post growth cooling the mismatching induces a significant amount of strain into the material which can in turn lead to the formation of dislocations.

In an attempt to counteract this problem a buffer layer is first grown on top of the sapphire. A thin layer of either GaN or AlN is deposited at low temperature (500°C) before the temperature is ramped up to ~1000 °C and a thicker layer of GaN grown [11,32]. The buffer layer is of poor crystalline quality but covers the surface of the substrate. During the ramp up to higher temperatures the buffer layer undergoes re-crystallisation and high quality GaN is grown on top of it.

Problems also occur in the growth of InGaN because of the 11% lattice mismatch between the two main constituents, InN and GaN. Furthermore, as indium is highly volatile only a small amount of it is incorporated at typical GaN growth temperatures. For this reason, InGaN growth is carried out at lower temperatures (~500–850°C) [30]. Unfortunately, the lower growth temperatures allow more defects to be incorporated into the material.

In this thesis two different techniques used to produce InGaN are described. A GaN buffer layer is deposited to improve the material quality in both techniques.

1.4.4 InGaN Crystal Structure

The crystal structure of InGaN may be wurtzite (hexagonal) or zincblende (cubic), as shown in Figure 1.4. The wurtzite structure is the more common; it is easier to grow and has given the better results to date in optoelectronic applications [1].

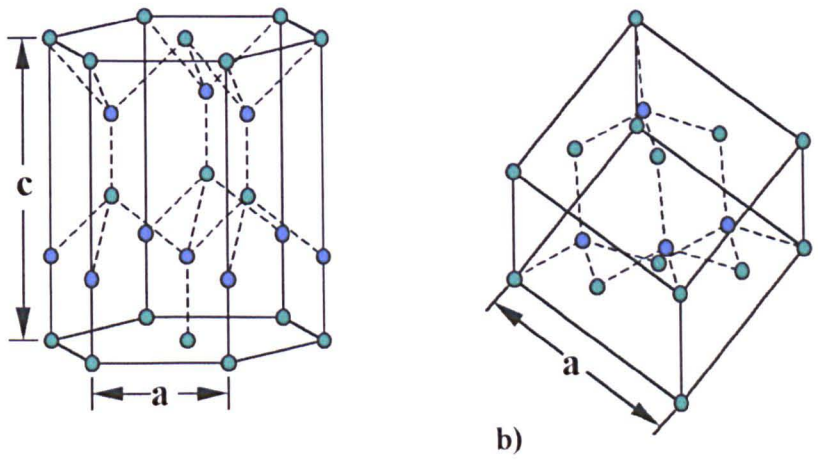

Figure 1.4: a) Wurtzite and b) Zincblende crystal structure of III-nitrides.

In both structures the bonding between nearest neighbours is tetrahedral. In the wurtzite structure the Bravais lattice is hexagonal. The structure can be thought of as a sequence of layers of atoms of the same element built up from regular hexagons [1]. The axis perpendicular to the hexagons, the c-axis, is usually the growth axis. The a and c lattice constants in the wurtzite crystal structure are shown in Figure 1.4a).

In ternary alloys, the constituent binary compounds influence the distance between the atoms [33]. Experimental values of the lattice constants a and c in GaN are 3.189Å and 5.185Å and in InN are 3.544Å and 5.718Å [33]. Ternary alloys are also expected to follow Vegard's Law whereby the lattice constant is directly proportional to the composition value.

It has been found that the polarity of the GaN buffer layer can affect the luminescence efficiency of InGaN [34]. The most common crystallographic orientation of GaN is to have faces perpendicular to the c-axis. These faces are polar: one is nitrogen-terminated, the other one is gallium-terminated [22]. The polarity is dependent on the growth technique used. In MOCVD samples Ga-faced polarity films are generally obtained, while in MBE material N-faced polarity is predominant. MBE-grown InGaN with a Ga-faced polarity GaN buffer layer has also been produced under specific growth conditions. The InGaN was found to have better crystalline quality and more efficient luminescence than that grown on the N-faced polarity films [34].

1.4.5 InGaN Nanostructure

Although the crystal structure of InGaN is easily determined, the nanostructure of the material is not fully understood. InGaN is thermodynamically unstable and has a tendency towards indium clustering and phase segregation [35]. This is attributed mainly to the large difference in the lattice constant of GaN and InN.

Nanostructure in InGaN was first reported by Chichibu et al. in 1996 [36]. Cross-sectional transmission electron microscopy (TEM) images showed a number of distinct dark spots typically ~3nm in diameter. The spots, termed quantum dots, were attributed to indium rich regions resulting from the partial phase separation of the InGaN alloy. In 1996, Narukawa et al. [37] and in 1998, McCluskey et al. [38] used energy-dispersive X-ray (EDX) microanalysis to confirm that the dots were In-rich in comparison to the rest of the material. The localisation of excited electrons

within such regions was suggested to explain the efficient optical properties of InGaN [37]. These ideas were further expanded in 1999, when it was reported that an extreme form of phase segregation occurs in InGaN [39,40]. This produces QDs of uniform composition, close to that of pure InN: therefore it is nanostructure rather than composition, which defines the material properties [39].

Evidence to suggest atomic ordering of the cation and anions within the InGaN crystal structure was recorded in 1998 using TEM and XRD [41,42]. The driving force for ordering in InGaN is believed to be the high lattice strain in the alloy. In the ordered phase, the system can accommodate the two different bond lengths in a more coherent fashion, producing less strain than would be present in a random alloy. However, atomic ordering has been found to be dependent on growth rate, composition and substrate orientation [41,42]. Furthermore, competition between atomic ordering and phase segregation in InGaN is believed to occur.

Intentionally grown InGaN quantum structures were first produced on AlGaN surfaces in 1997 [43]. In 1998, self-assembled InGaN QDs were grown on GaN layers [44]. InGaN QDs can either be fabricated by self-assembled growth or selective-growth. Self-assembled InGaN QDs produced by the Stranski-Krastanov growth mode form 3-D InGaN islands as an efficient way of relaxing the material strain [45]. The material produced was found to have very efficient luminescent properties with strong emission persisting up to room temperature [46,47]. Selective growth by photolithography and ion beam etching has been used to produce InGaN mircodisks for use in semiconductor microdisk lasers [48].

Despite the fabricated growth of InGaN nanostructures, there is still much uncertainty as to whether it is the actual fabricated structure or smaller structures within these that give InGaN its luminescent properties.

1.5 Objective of Thesis

In this thesis an investigation of the optical properties, composition and local structure of InGaN will be presented. Optical experiments and structural measurements were carried out to address the issues outlined in Section 1.4. The origin of InGaN luminescence is as yet unknown as the nanostructure of the material remains ill defined. The relationship between luminescence and composition and also the excitation/emission cycle of InGaN are discussed.

The thesis is split into nine chapters. Chapter 1 covers the history and applications of III-nitrides and the properties of InGaN. In Chapter 2 the growth, structure and main theories on InGaN luminescence are discussed. Chapter 3 outlines the experimental procedures used. Analysis of the optical characterisation results is given in Chapters 4, 6 and 8. In Chapter 5, composition measurements are related to the photoluminescence spectroscopy results of Chapter 4. Images taken using confocal microscopy to examine InGaN are presented in Chapter 6 and extended X-ray absorption fine structure measurements to look at the interatomic spacing of the material in Chapter 7. Chapter 8 discusses photoluminescence excitation spectroscopy measurements on InGaN samples produced by two different growth techniques. Finally, a short conclusion to summarise the work is given in Chapter 9 with some suggestions as to how it could be continued.

1.6 References

[1] S. Nakamura and G. Fasol, *The Blue Laser Diode*, Springer, Berlin (1997).

[2] M. Asif Khan, J. N. Kuznia, A. R. Bhattarai and D. T. Olson, Appl. Phys. Lett. **62**, 1786 (1993).

[3] Robert V. Steele, Compound Semiconductor, **6** (5) (July 2000), *Update on GaN Technology and Markets*.

[4] R. Juza and H. Hahn, Z. Anorg. Allg. Chem. **239**, 282 (1938); R. Juza and H. Hahn, Z. Anorg. Allg. Chem. **244**, 133 (1940).

[5] H. Grimmeiss and Z. H.-Koelmans, Nature (London) **14a**, 264 (1959).

[6] H. P. Maruska and J. J. Tietjen, Appl. Phys. Lett. **15**, 327 (1969).

[7] M. T. Duffy, C. C. Wang, G. D. O'Clock, S. H. McFarlane and P. Z. Zanzucchi, J. Electron Mater. **2**, 359 (1973).

[8] J. I. Pankove, *GaN and Related Materials*, Gordon and Breach, New York, (1997).

[9] R. Dingle, K. L. Shaklee, R. F. Leheny and R. B. Zetterstrain, Appl. Phys. Lett. **19**, 5 (1971).

[10] S. Yoshida, S. Misawa and S. Gonda, Appl. Phys. Lett. **42**, 427 (1983).

[11] H. Amano, N. Sawaki, I. Akasaki and Y. Toyoda, Appl. Phys. Lett. **48**, 353 (1986).

[12] H. Amano, M. Kito, K. Hiramatsu and I. Akasaki, Jpn. J. Appl. Phys. **28**, L2112 (1989).

[13] Matthew Quint, Quint Public Relations, Internet Press Release (June 18 2001), *Nichia Moves Into Volume Production of High Power Violet Laser Diodes*.

[14] Nichia website, http://www.nichia.com/led/InGaN.shtml (2001).

[15] Compound Semiconductor Press Release, (July 2000), *Arizona Trafficlight Technologies Inc. Offers Free Traffic Signals to Every US City.*

[16] Stephen J. Matthews, Laser Focus World, (April 2001), Back to Basics; III-V Light Emitting Diodes, *New Light From Old Sources.*

[17] R. W. Mills and K. D. Jandt, IEEE, LEOS Newsletter, (June 1998), *Blue LEDs for Curing Polymer-Based Dental Filling Materials.*

[18] K. Daly and A. Bierman IAEEE newsletter, (1999), *Energy Efficiency and LEDs.*

[19] Sanuvox website, http://www.sanuvox.com/FQA.htm (2001).

[20] S.-I. Nagahama, T. Yanamoto, M. Sano and T. Mukai, Jpn. J. Appl. Phys. **40**, L785 (2001).

[21] LumiLEDs homepage, http://www.lumileds.com/news/wallplug.html (2001).

[22] J. H. Edgar, *Properties of Group III Nitrides*, No. 11 EMIS Datareview, INSPEC, London (1994).

[23] B. Gil and M. Leroux, *Properties of Indium Nitride*, EMIS Datareview 23 (1999).

[24] T. Inushima, V. V. Mamutin, V. A. Vekshin, S. V. Ivanov, T. Sakon, M. Motokawa and S. Ohoya, J. Cryst. Growth **227-228**, 481 (2001).

[25] V. Yu. Davydov, A. A. Klochikhin, V. V. Emtsev, S. V. Ivanov, V. V. Vekshin, F. Bechstedt, J. Furthmüller, H. Harima, A. V. Mudryi, A. Hashimoto, A. Yamamoto, J. Aderhold, J. Graul and E. E. Haller, phys. stat. sol. (b) **230**, R4 (2002).

[26] T. Inushima, T. Yaguchi, A. Nagase, A. Iso and T. Shiraishi, Inst. Phys. Conf. Ser. No. **142**: Chapter 5, 971 (1995).

[27] V. Yu. Davydov, A. A. Klochikhin, R. P. Seisyan, V. V. Emtsev, S. V. Ivanov, F. Bechstedt, J. Furthmüller, H. Harima, A. V. Mudryi, J. Aderhold, O. Semchinova and J. Graul, phys. stat. sol. (b) **229**, R1 (2002).

[28] S. Nakamura and T. Mukai, Jpn. J. Appl. Phys. **31**, L1457 (1992).

[29] S. Nakamura, J. Vac. Sci. Technol. A **13(3)**, 705 (1995).

[30] B. Gil, *Group III Nitride Semiconductor Compounds*, Oxford University Press, New York (1998).

[31] S. D. Lester, F. A. Ponce, M. G. Craford and D. A. Steigerwald, Appl. Phys. Lett. **66**, 1249 (1995).

[32] S. Nakamura, T. Mukai and M. Senoh, J. Appl. Phys. **71**, 5543 (1992).

[33] J. H. Edgar, *Gallium Nitride and Related Semiconductors*, No. 23 EMIS Datareview, INSPEC, London (1998).

[34] X. Q. Shen, T. Ide, M. Shimizu and H. Okumura, J. Appl. Phys. **89**, 5731 (2001).

[35] I.-H. Ho and G. B. Stringfellow, Appl. Phys. Lett. **69**, 2701 (1998).

[36] S. Chichibu, T. Azuhata, T. Sota and S. Nakamura, Appl. Phys. Lett. **69**, 4188 (1996).

[37] Y. Narukawa, Y. Kawakami, M. Funato, S. Fujita, S. Fujita and S. Nakamura, Appl. Phys. Lett. **70**, 981 (1997).

[38] M. D. McCluskey, L. T. Romano, B. S. Krusor, D. P. Bour and N. M. Johnson, Appl. Phys. Lett. **72**, 1730 (1998).

[39] K. P. O'Donnell, R. W. Martin and P. G. Middleton, Phys. Rev. Lett. **82**, 237 (1999).

[40] R. W. Martin, P. G. Middleton, K. P. O'Donnell and W. Van der Stricht, Appl. Phys. Lett. **74**, 263 (1999).

[41] D. Doppalapudi, S. N. Basu, K. F. Ludwig and T. D. Moustakas, J. Appl. Phys. **84**, 1389 (1998).

[42] P. Ruterana, G. Nouet, W. Van der Stricht, I. Moerman and L. Considine, Appl. Phys. Lett. **72**, 1742 (1998).

[43] H. Hirayama, S. Tanaka, P. Ramvall and Y. Aoyagi, Appl. Phys. Lett. **72**, 1736 (1998).

[44] K. Tachibana, T. Someya and Y. Arakawa, Appl. Phys. Lett. **74**, 383 (1999).

[45] B. Damilano, S. Vezian, N. Grandjean and J. Massies, Jpn. J. Appl. Phys. **38**, L1357 (1999).

[46] B. Damilano, N. Grandjean, S. Dalmasso and J. Massies, Appl. Phys. Lett. **75**, 3751 (1999).

[47] C. Adelmann, J. Simon, G. Feuillet, N. T. Pelekanos and B. Daudin, Appl. Phys. Lett. **76**, 1570 (2000).

[48] L. Dai, B. Zhang, J. Y. Lin and H. X. Jiang, J. Appl. Phys. **89**, 4951 (2001).

CHAPTER 2: GROWTH, STRUCTURE AND LUMINESCENT PROPERTIES OF InGaN

2.1 Introduction

The two growth techniques used to produce InGaN are metallorganic chemical vapour deposition (MOCVD) and molecular beam epitaxy (MBE). The structure of the InGaN samples can take a variety of different forms. The InGaN active layer may be grown as a bilayer on GaN (epilayer), sandwiched between GaN barriers (QW) or intentionally fabricated into nanostructures (QB). In this work InGaN epilayer and QW samples grown by MOCVD and QW and QB samples grown by MBE were investigated.

There has been much speculation on the origin of InGaN luminescence. A number of theories have been presented to explain the high luminescent efficiencies and the spectral properties of the material in its several different structural forms. Composition fluctuations, nanostructure, piezoelectric and spontaneous polarisation fields all seem capable of influencing InGaN emission. In this chapter the growth, structure and luminescent properties of InGaN are discussed.

2.2 InGaN Growth Techniques

A general description of the MOCVD and MBE growth techniques used to produce the samples investigated in this work is outlined in the following sections.

2.2.1 MOCVD Growth

MOCVD has developed over the past ten years as the most commonly used method for the epitaxial growth of good quality III-nitride material [1]. The elements required for MOCVD growth are produced by the thermal decomposition of source gases on a heated substrate. Organometallic source materials used to produce InGaN are typically trimethylgallium, trimethylindium and ammonia, to provide gallium, indium and nitrogen respectively. The trimethylgallium (TMG) is stored as a liquid and the trimethylindium (TMI) as a solid in separate containers termed bubblers. The TMG and TMI are passed through the bubbler by means of a carrier gas, such as hydrogen or nitrogen, to the substrate, which is held in a reaction chamber. Ammonia is introduced directly into the chamber from a separate gas cylinder. The reagents are then dissociated in the reaction chamber and deposited onto the substrate. A diagram of a typical MOCVD growth reactor system is shown in Figure 2.1 [2].

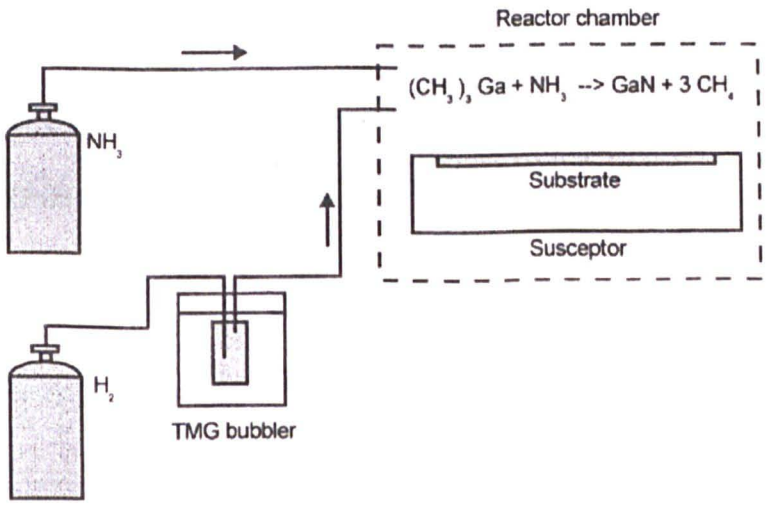

Figure 2.1: A typical III-nitride MOCVD growth reactor system.

The substrate temperature, V/III ratio, gas flow rate and even the type of carrier gas have been found to influence the material growth [1,3]. Problems encountered producing MOCVD InGaN include the difficulty of incorporating indium and nitrogen into the material. The volatility of indium above ~1000°C limits the upper growth temperature that can be used [4], while the temperature must also be low enough to stop indium droplets forming on the surface. Using nitrogen as opposed to hydrogen as the carrier gas has also been found to reduce In droplet formation [1]. Typical MOCVD growth temperatures for InGaN are ~800°C, compared to over 1000°C for GaN. Unfortunately, the cracking efficiency of ammonia is very poor at low temperatures, consequently a high V ratio is required to avoid the formation of nitrogen vacancies.

A number of modifications have been applied to the MOCVD process to improve the quality of the InGaN material produced. Two of the most successful techniques that have been applied are the use of showerheads and the two-flow growth process. Showerheads are used to prevent pre-reaction of the reagents in the reaction chamber [5], and the two flow growth process has, in addition to the main gas flow parallel to the substrate, another subflow perpendicular to the substrate [6].

2.2.2 MBE Growth

MBE growth is a refined form of ultrahigh vacuum (UHV) evaporation [7]. Although well established for the growth of semiconductors since its invention in 1958 [8], the development of MBE for the III-nitrides has been slow. This is mainly because the low growth temperatures involved make it difficult to incorporate

nitrogen into the growing layer. The source elements are heated in Knudsen cells. The atoms or molecules are then directed onto a heated substrate where they react to form the layers. A diagram showing the typical layout of an MBE system is given in Figure 2.2 [7].

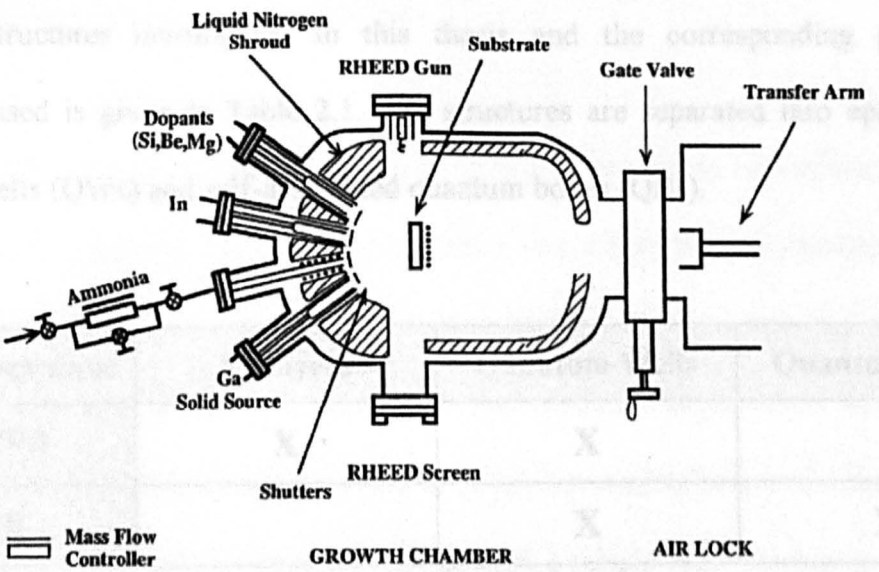

Figure 2.2: A typical III-nitride MBE growth reactor system.

For InGaN growth, solid sources are often used for the Ga and In supply. However, due to the extremely high binding energy of the N_2 molecule, nitrogen cannot be supplied directly and is provided in the form of ammonia. InGaN MBE growth can be performed at much lower temperatures than MOCVD, typically ~600°C. This suits the conditions required to incorporate indium into the material. Furthermore, the UHV environment reduces the level of background contamination in the growth chamber. The UHV also makes possible the use of in-situ electron-beam characterisation. Techniques such as reflection high-energy electron diffraction

(RHEED) can be used to monitor the evolving surface structure of the material and to determine its composition [9].

2.3 Structure

InGaN may be incorporated in a variety of different structures. A table outlining the different structures investigated in this thesis and the corresponding growth technique used is given in Table 2.1. The structures are separated into epilayers, quantum wells (QWs) and self-assembled quantum boxes (QBs).

Growth Technique	Epilayers	Quantum Wells	Quantum Boxes
MOCVD	X	X	
MBE		X	X

Table 2.1: Structure and the growth technique used to produce the InGaN samples investigated.

2.3.1 Epilayers

In an ideal material, epilayer growth is where a thin, single-crystal layer of material is grown on the surface of a single-crystal substrate [10]. However for InGaN, epilayer growth is more complicated than as described in the idealised system. The InGaN epilayer is typically grown on top of a GaN or AlN buffer layer which is deposited onto a sapphire substrate. The buffer layer is grown two-dimensionally from a large number of nucleation sites, created by the deposition of a nucleation

layer onto the substrate. The resulting epilayer films frequently show a columnar habit, composed of hexagonal columns with approximately the same orientation. The InGaN layer is then grown in a similar fashion onto the buffer layer. Defects and dislocations in the material are mainly generated at the boundaries between grains. The strain induced by the large lattice and thermal mismatch between GaN and InN produces a large number of defects.

The state of strain in the material has been shown to be mainly dependent on the thickness of the epilayer [11]. InGaN epilayers can either be pseudomorphically strained, relaxed or a mix of the two. Pseudomorphic growth is where the in-plane lattice constant of one epilayer matches that of the material it is grown on. In InGaN, the material undergoes compressive strain to match the smaller lattice constant of its GaN buffer layer. It has been reported that beyond a certain layer thickness, termed the critical layer thickness, no more strain can be accommodated in the lattice [11]. At this point defects and dislocations form and the InGaN layer begins to relax. An estimated value for the critical layer thickness in InGaN, with indium nitride content, $x = 0.15$, is ~65nm [12].

Despite their large defect density InGaN epilayers have high luminescence efficiency. Localisation of the excited electron-hole pair, also referred to as an exciton, has been suggested to account for this. The exact nature of localisation in InGaN will be discussed in more detail in Section 2.4.1.

2.3.2 Quantum Wells

In a quantum well (QW) structure, the sample can be thought of as a sandwich (ABA) composed of two different semiconductor materials, A and B. If the two semiconductors have different optical bandgap values then discontinuities in the conduction and valence band form at the interfaces. When the material placed in the middle of the sandwich has a lower optical bandgap value than those surrounding it then a 'potential well' is formed, as shown in Figure 2.3. In this case, known as a type I QW, the electrons and holes are both confined in the same layer. The material with the smaller bandgap is termed the 'well', while the larger bandgap material is the 'barrier'. In InGaN/GaN QWs, the InGaN layer is the well and the GaN the barrier. This structure creates a two dimensional quantum confinement of the excited electron and hole within series of discrete energy levels in the well. The width and depth of the well determines the values of these energy levels.

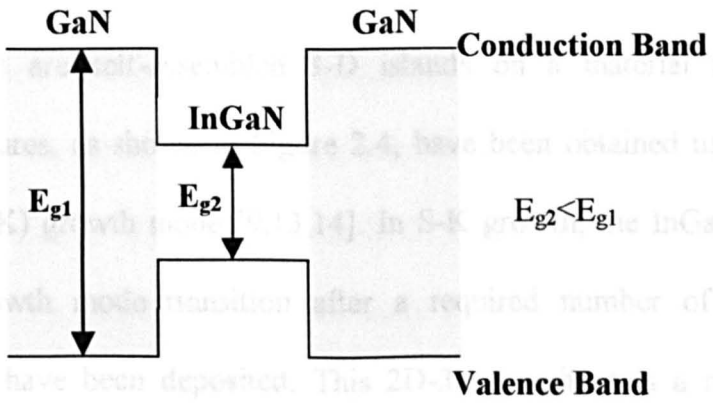

Figure 2.3: An InGaN QW Structure.

InGaN/GaN QWs are usually grown on top of a GaN barrier layer which is deposited on a sapphire substrate. For a QW structure with a single InGaN active layer, the material is referred to as a single quantum well (SQW). For a sample with a number of active layers, each separated by a barrier layer, the structure is termed a multiple quantum well (MQW). In a MQW, assuming the barrier layer is thick enough to prevent coupling of the electrons between wells, then each well will act independently. This effectively amplifies the optical properties of the structure while maintaining the original confinement conditions of a SQW. Typical thickness of the InGaN active layer is of the order of a few nm. The optical properties of the material are dependent on the well dimensions through the quantum confinement effect. The small thickness of the well also suggests that for a typical InGaN/GaN QW, the InGaN layer is grown pseudomorphically with the GaN barrier.

2.3.3 Quantum Boxes

Quantum boxes (QBs) are self-assembled 3-D islands on a material surface. InGaN/GaN QB structures, as shown in Figure 2.4, have been obtained using the Stranski-Krastanov (S-K) growth mode [9,13,14]. In S-K growth, the InGaN alloy exhibits a 2D-3D growth mode transition after a required number of InGaN molecular monolayers have been deposited. This 2D-3D transition is a result of compressive strain produced by the large lattice mismatch between GaN and InN. The 2D-3D transition relaxes the compressive strain acting on the InGaN material. QBs are also often referred to as quantum dot (QD) structures in the literature. However, to avoid confusion between the deliberately produced S-K QD structures

and the QDs to be discussed in Section 2.4.1, the S-K type QDs will be referred to as QBs throughout this thesis.

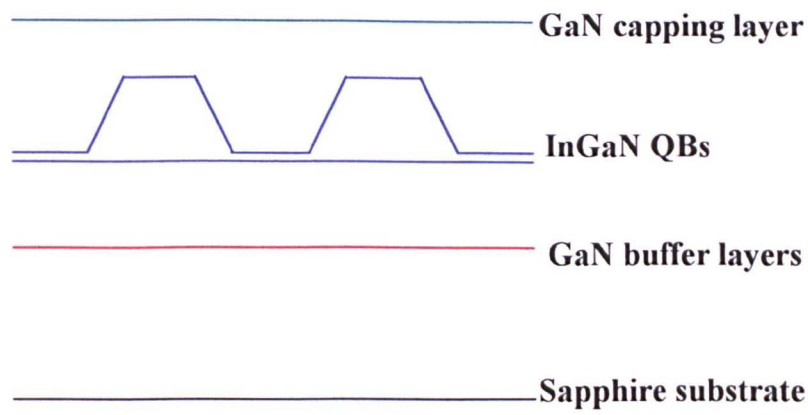

Figure 2.4: A Typical InGaN QB Structure.

The number of monolayers required to produce InGaN QBs has been found to be dependent on the indium nitride content; the lower the indium nitride fraction the greater the number of monolayers [9]. Furthermore, for an indium nitride fraction <12% no 2D-3D transition is observed, just a roughening of the sample surface [9]. Typical dimensions of the InGaN QBs, measured by atomic force microscopy (AFM), were found to be 10 to 40 nm in diameter by 2 to 4 nm high. The density of the QBs also measured by AFM was approximately 5-9x10^{10} cm^{-2}, an order of magnitude larger than the dislocation density of the material [13,14]. Nevertheless, the luminescence of InGaN QB structures has been found to be highly efficient. Temperature dependent photoluminescence (PL) measurements showed that on comparison with InGaN QWs and epilayers, all grown by MBE, the QBs maintained substantially higher luminescence output, even at room temperature [13,14]. At 10K, the PL intensity was found to be 30 times stronger from a QB sample than from a

comparable epilayer [13]. The authors suggest that the high luminescence efficiency is due to strong localisation effects in the QB structures.

The InGaN layers are grown onto a GaN buffer deposited on a sapphire substrate. After the 2D-3D transition is completed, a GaN capping layer is grown over the QBs to protect the QBs and recover the smooth surface layer of the material. The QB samples investigated in this thesis were all grown by MBE using the S-K growth mode. S-K QBs have to-date only been successfully produced by MBE. However, InGaN nanometer-scale self-assembled structures have also been produced by MOCVD [15].

2.4 Properties influencing InGaN Luminescence

When radiative recombination of an exciton occurs, luminescence is emitted by the material. An exciton with radius R, usually much greater than the lattice constant, termed a Wannier exciton, samples a local region of the crystal potential as it decays. In an alloy, the emission energy is therefore dependent on the local composition of the alloy within the Wannier exciton orbit [16]. In materials such as InGaN, the situation is further complicated by the effects of phase segregation and internal electric fields produced in the material as a result of its lattice and thermal mismatch.

Excitons are attracted to regions where the recombination energy is lowered. A value for the radius of the Wannier exciton in InGaN is difficult to estimate, although an indication of its sampling region can be approximated from the Wannier

exciton radius in GaN, 3.0nm [17]. Therefore, for a typical InGaN epilayer structure of thickness >50nm, or an InGaN QW or QB with an active layer thickness on the order of a few nm, the exciton recombination process will be influenced by the effects of nanostructure, piezoelectric and polarisation fields acting within the material structure. The effects of each of these on the recombination process can be observed in the luminescence properties of InGaN. Localisation of the exciton in nanostructures that allow radiative recombination to occur may explain the high quantum efficiency of the material, despite its large defect density. Localisation and the influence of the electric fields may be responsible for the lowering of the emission energy with respect to the absorption energy, the Stokes' shift, which has been experimentally obtained in InGaN. High quantum efficiencies and the Stokes' shift have been observed in InGaN epilayer, QW and QB samples.

Nevertheless, the emission mechanisms of InGaN are not yet fully understood. This section discusses the main theories currently proposed to explain the influences acting on the exciton recombination process in InGaN. The section is split into three parts; localisation effects, the effects of piezoelectric and spontaneous polarisation fields and the combined effects of both.

2.4.1 Localisation Effects in InGaN

An exciton trapped in a potential well is said to be localised. Exciton localisation in InGaN is the main theory used to explain the efficient optical properties of the material in all of its structural forms.

InGaN is a thermodynamically unstable material [18]; it has at least a theoretical tendency to phase-segregate, form indium clusters and produce large numbers of defects, each of which will result in sites for possible exciton localisation. The nature of localisation in InGaN is unclear and attempts to explain the experimental results obtained have produced a number of different localisation models.

One model postulates that InGaN luminescence is produced as a result of a distribution of localised states (tail states). These states extend downwards from the bottom of the conduction band and upwards from the top of the valence band, with the density of states decreasing exponentially from the optical bandedge [19]. The excitons may lose energy non-radiatively as a result of tunneling between states [20]. However, when the non-radiative and radiative lifetimes are of the same order, a significant amount of radiative emission occurs.

Single localisation states at a fixed energy below the InGaN bandgap have also been proposed as possible sites for radiative recombination. In 1996, Chichibu et al. reported evidence of such sites in an InGaN QW [21]. A number of distinct dark spots, typically ~3nm in diameter, were observed using TEM microscopy and were attributed to indium rich regions produced from the partial phase segregation of the InGaN alloy. Each dark spot, or quantum dot (QD), was said to represent a potential fluctuation of the composition in the QW [21]. If the potential gap is large enough, then the electron can be confined laterally and therefore localised by the QD. In 1997, Narukawa et al. measured the same material using TEM-based energy dispersive X-ray (EDX) analysis and found the dots to be indium rich in comparison

to the rest of the material [22]. Spatially resolved cathodoluminescence studies on InGaN QWs by Chichibu et al. in 1997 produced images of the InGaN sample in which the structure was seen to exhibit a granular texture [23]. These images showed that regions of the sample were luminescent over a range of wavelengths, indicating the possibility of internal structure within the grains. The authors attributed this result to a variety of QDs of differing InN molar fractions produced by compositional undulations within the QW active layer [23]. Further TEM-based EDX measurements by McCluskey et al. also show In-rich nanoscale regions in InGaN; this was presented as evidence of InGaN phase segregation [24].

In 1998, it was reported that localisation in QDs produced by an extreme form of phase segregation, rather than compositional fluctuations, occurs in InGaN. This results in QDs of uniform composition close to that of pure InN and indicates that it is nanostructure rather than composition that define the light emission characteristics of the material [25,26]. By increasing the InN molar fraction, the diameter of the QDs would also increase. As the larger QD diameter results in a reduction in the quantum confinement energy, then a shift towards red emission would be observed in InGaN material with higher In fractions.

Temperature dependent studies of photo- and electroluminescence measurements on InGaN have also suggested the presence of localised states [27,28]. Furthermore, excitation and time-resolved spectra exhibiting bandtails indicate localisation, as the bandtail states are believed to be formed due to the local potential minima of the QDs [25,26,29].

2.4.2 Piezoelectric and Spontaneous Polarisation Field Effects in InGaN

Strong electric fields acting on the exciton have also been proposed to influence InGaN emission. Electric fields occur in III-nitride materials as a result of very strong spontaneous and piezoelectric polarisation effects. Spontaneous polarisation occurs due to the non-centrosymmetry of the wurtzite III-nitride structure and the large ionicity factor of the covalent metal to nitrogen bond [30]. It has been shown to be very large in III-nitride materials [31]. Piezoelectric polarisation arises because of external stresses acting on the non-centrosymmetric structure. In InGaN stress-induced polarisation is a consequence of the large lattice and thermal mismatch between GaN and InN. The direction of the polarisation is determined by the strain acting on the material. For compressively strained InGaN both spontaneous and piezoelectric polarisations are orientated along the hexagonal c-axis [30].

The influence of the electric field on the recombination process can be described using the quantum-confined Stark effect (QCSE) [32]. For an InGaN QW, or QB structure, the QCSE operates as follows. If the electric field, orientated perpendicular to the layers, is strong enough then spatial separation of the exciton, between the electron and hole wavefunctions will occur, as shown in Figure 2.5 [32,33]. As the electrons and holes are pulled towards opposite ends of the InGaN active layer, the charge density concentrates near the walls of the well and the wavefunction overlap is reduced. Providing the electron-hole correlation is still strong enough, radiative recombination can be maintained. This broadening effect is referred to as the QCSE and is dependent on the strength of the electric field and the

width of the QW. Typical electric field strengths in InGaN have been calculated to be of the order 10^8V/m [34,35].

For epilayer materials a similar explanation to the QCSE may be applied. In the epilayer the induced electric field still produces a separating effect on the electron and hole wavefunctions, although the electron and hole are not confined by the constraints of a potential well. This is referred to as the quantum-confined Franz-Keldish effect (QCFKE) [36].

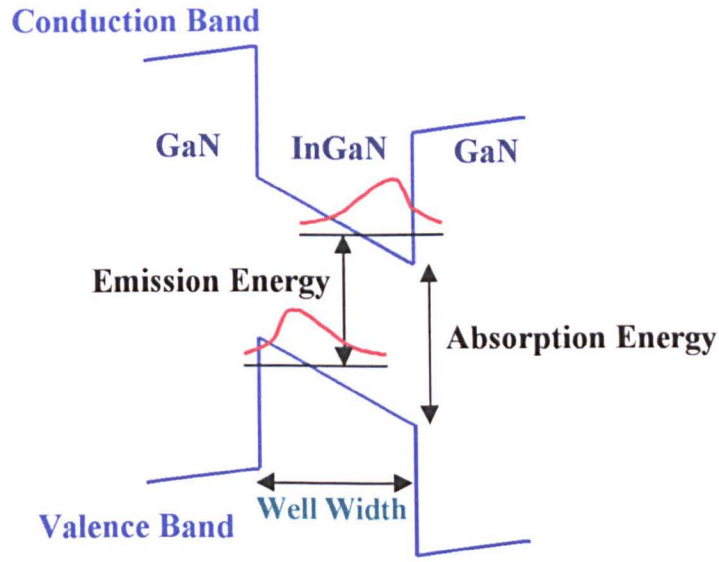

Figure 2.5: The QCSE on an InGaN QW.

2.4.3 A Combination of Both Localisation and Electric Fields

The properties of InGaN luminescence may be explained using either the localisation or the electric field argument. However, it has also been proposed that it

is in fact a combination of both effects that determines InGaN emission [25,26,33,37].

The ideas of localisation and piezoelectric fields are not in contradiction and may be thought of as influencing each other. The presence of a localisation site, such as a QD, would effect the strain acting on the material and subsequently effect the piezoelectric field induced. Similarly, the piezoelectric field will effect the recombination process in the localisation site by means of the QCSE, as discussed earlier.

2.5 Summary

In this chapter a brief description of the growth techniques used and an outline of the structure of the samples investigated was presented. Furthermore, the main theories currently proposed to explain the exciton recombination process and subsequently the emission properties of InGaN were discussed. The discussion was split into three main parts; localisation of the exciton, the effects of spontaneous and strain-induced electric fields and a combination of both effects. Each section was described with respect to the different possible sample structures.

2.6 References

[1] J. H. Edgar, *Gallium Nitride and Related Semiconductors*, No. 23 EMIS Datareview, INSPEC, London (1998).

[2] Wim Van der Stricht, PhD Thesis, University of Ghent, *Development of group III nitride technology for the realisation of light emitting diodes*, unpublished (1998-1999).

[3] A. Sohmer, J. Off, H. Bolay, V. Härle, V. Syganow, Jin Seo Im, V. Wagner, F. Adler, A. Hangleiter, A. Dörnen, F. Scholz, D. Brunner, O. Ambacher and H. Lakner, MRS Int. J. Semi. Res. **2**, Article 14 (1997).

[4] S. Nakamura, T. Mukai and M. Senoh, Appl. Phys. Lett. **64**, 1687 (1994).

[5] Thomas Swan homepage,
http://www.thomasswan.co.uk/TS_CCS_GaN_App_1.html.

[6] S. Nakamura and G. Fasol, *The Blue Laser Diode*, Springer, Berlin (1997).

[7] B. Gil, *Group III Nitride Semiconductor Compounds*, Oxford University Press, New York (1998).

[8] K. G. Günther, Z. Nat. forsch. A, **13**, 1081 (1958).

[9] N. Grandjean and J. Massies, Appl. Phys. Lett. **72**, 1078 (1998).

[10] D. Neaman, *Semiconductor Physics and Devices Basic Principles*, IRWIN, USA (1992).

[11] S. Pereira, M. R. Correia, E. Pereira, K. P. O'Donnell, R. W. Martin, M. E. White, E. Alves, A. D. Sequeira and N. Franco, Mat. Sci. Eng. B **93**, 163 (2002).

[12] C. A. Parker, J. C. Bedair, S. M. Bedair, M. J. Reed, S. X. Liu and N. A. El-Masry, Appl. Phys. Lett. **75**, 2776 (1999).

[13] B. Damilano, N. Grandjean, S. Dalmasso and J. Massies, Appl. Phys. Lett. **75**, 3751 (1999).

[14] C. Adelmann, J. Simon, G. Feuillet, N. T. Pelekanos and B. Daudin, Appl. Phys. Lett. **76**, 1570 (2000).

[15] K. Tachibana, T. Someya and Y. Arakawa, Appl. Phys. Lett. **74**, 383 (1999).

[16] K. P. O'Donnell, phys. stat. sol. (a), **183**, 117 (2001).

[17] F. Binet, J. Y. Duboz, E. Rosencher, F. Scholz and V. Härle, Phys. Rev. B **54**, 8116 (1996).

[18] I.-H. Ho and G. B. Stringfellow, Appl. Phys. Lett. **69**, 2701 (1998).

[19] A. Satake, Y. Masumoto, T. Miyajima, T. Asatsuma, F. Nakamura and M. Ikeda, Phys. Rev. B **57**, R2041 (1998).

[20] C. Gourdon and P. Lavallard, phys. stat. sol. (b), **153**, 641 (1989).

[21] S. Chichibu, T. Azuhata, T. Sota and S. Nakamura, Appl. Phys. Lett. **69**, 4188 (1996).

[22] Y. Narukawa, Y. Kawakami, M. Funato, S. Fujita, S. Fujita and S. Nakamura, Appl. Phys. Lett. **70**, 981 (1997).

[23] S. Chichibu, K. Wada and S. Nakamura, Appl. Phys. Lett. **71**, 2346 (1997).

[24] M. D. McCluskey, L. T. Romano, B. S. Krusor, D. P. Bour and N. M. Johnson, Appl. Phys. Lett. **72**, 1730 (1998).

[25] R. W. Martin, P. G. Middleton, K. P. O'Donnell and W. Van der Stricht, Appl. Phys. Lett. **74**, 263 (1999).

[26] K. P. O'Donnell, R. W. Martin and P. G. Middleton, Phys. Rev. Lett. **82**, 237 (1999).

[27] Y.-H. Cho, G. H. Gainer, A. J. Fischer, J. J. Song, S. Keller, U. K. Mishra and S. P. DenBaars, Appl. Phys. Lett. **73**, 1370 (1998).

[28] P. Eliseev, P. Perlin, J. Lee and M. Osiński, Appl. Phys. Lett. **71**, 569 (1997).

[29] Y. Narukawa, Y. Kawakami, S. Fujita, S. Fujita and S. Nakamura, Phys. Rev. B **55**, R1938 (1997).

[30] O. Ambacher, R. Dimitrov, M. Stutzmann, B. E. Foutz, M. J. Murphy, J. A. Smart, J. R. Shealy, N. G. Weimann, K. Chu, M. Chumbes, B. Green, A. J. Sierakowski, W. J. Schaff and L. F. Eastman, phys. stat. sol (b), **216**, 381 (1999).

[31] F. Bernardini, V. Fiorentini and D. Vanderbilt, Phys. Rev. B **56**, R10024 (1997).

[32] D. A. B. Millar, D. S. Chemla, T. C. Damen, A. C. Gossard, W. Wiegmann, T. H. Wood and C. A. Burrus, Phys. Rev. Lett. **53**, 2173 (1984).

[33] M. Buongiorno Nardelli, K. Rapcewicz and J. Bernholc, Appl. Phys. Lett. **71**, 3135 (1997).

[34] F. D. Sala, A. Di Carlo, P. Lugli, F. Bernadini, V. Fiorentini, R. Scholz and J.-M. Jancu, Appl. Phys. Lett. **74**, 2002 (1999).

[35] J. A. Davidson, P. Dawson, T. Wang, T. Sugahara, J. W. Orton and S. Sakai, Semicond. Sci. Technol. **15**, 497 (2000).

[36] D. A. B. Miller, D. S. Chemla and S. Schmitt-Rink, Phys. Rev. B **33**, 6976 (1986).

[37] S. Chichibu, A. C. Abare, M. S. Minsky, S. Keller, S. B. Fleischer, J. E. Bowers, E. Hu, U. K. Mishra, L. A. Coldren and S. P. DenBaars, Appl. Phys. Lett. **73**, 2006 (1998).

CHAPTER 3: EXPERIMENTAL PROCEDURES

The optical characterisation and compositional measurement techniques used in the investigation of InGaN materials as described in this thesis are outlined in the following sections.

3.1 OPTICAL CHARACTERISATION TECHNIQUES

3.1.1 Introduction

A series of experiments was carried out to determine the optical properties of InGaN epilayer, QW and QB samples. The experimental techniques used were photoluminescence spectroscopy, confocal microscopy and photoluminescence excitation spectroscopy. By analysing the results obtained using each of these techniques, the emission properties, surface morphology and excitation/emission cycle of InGaN could be characterised.

3.1.2 Photoluminescence Spectroscopy

When optical excitation excites electrons across the bandgap of a semiconductor, photons emitted during the radiative decay process give rise to photoluminescence (PL). In PL spectroscopy, the spectral distribution of the emitted photons is referred to as the emission spectrum of the material.

By measuring the emission spectrum of InGaN, the radiative properties of the material may be determined. Information on the presence and concentrations of any impurities and defects can be extracted from the spectrum.

The experimental set-up for the PL spectroscopy measurements is shown in Figure 3.1.

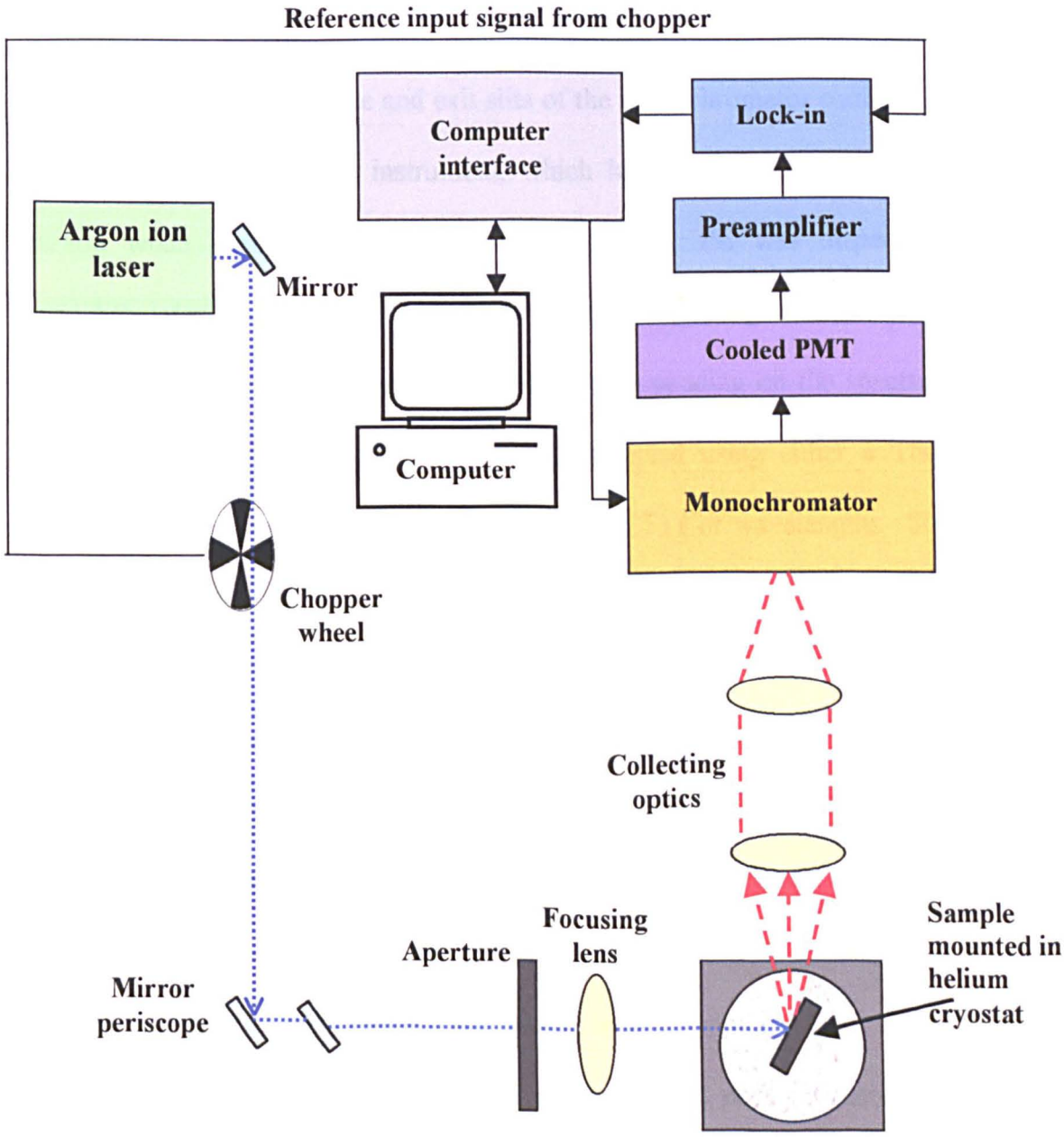

Figure 3.1: Experimental set-up for the PL spectroscopy measurements.

PL was excited using a loosely focused Coherent Innova 90 argon ion laser, which produces a spot of diameter approximately 100μm on the sample. The InGaN samples were mounted on the moveable cold head of a closed-cycle helium refrigerator, set on a moveable XYZ stage. InGaN luminescence was collected with a lens at f/0.1 and focused on the entrance slits of a McPherson 0.67m monochromator. The luminescence was collected at an angle of 30 degrees to the excitation beam in order to reduce the intensity of reflected laser light entering the monochromator. The entrance and exit slits of the monochromator could be adjusted to set the resolution of the instrument, which has a nominal dispersion of 0.83 nm/mm when used with a 1800 line/mm grating. PL was dispersed in the monochromator by a computer-controlled diffraction grating, blazed for either the visible (350-850nm) or infra-red (600-1200nm). Depending on the spectral region, the light output of the monochromator was detected using either a Thorn EMI Gencom Inc 3365 cooled photomultiplier tube (PMT) (for wavelengths <800nm) or a liquid nitrogen cooled, Edinburgh Instruments EI germanium detector (for wavelengths >600nm). The PMT was connected via a Stanford SR570 current preamplifier to a Stanford SR810 DSP lock-in amplifier and the germanium detector via a Stanford SR560 voltage preamplifier. A reference signal from a chopper was also connected to the lock-in and used to distinguish PL emission from background noise. The digital lock-in measured the amplitude of the AC input signal from the detector and relayed the resultant DC signal to a computer via a built-in RS232 interface on the lock-in. The computer's second RS232 port was used to supply a train of pulses to control the stepper motor unit to drive the monochromator. The measurements were recorded using in-house software and presented in the form of

an emission spectrum, plotting signal voltage against wavelength selected. Prior to recording each spectrum, the PL signal was optimised at its peak energy by adjusting the collecting optics to best position the sample image on the monochromator slits.

3.1.3 Photoluminescence Mapping

Photoluminescence mapping of the InGaN sample was carried out to determine the uniformity (or frequently the lack of uniformity) of the emission properties across the sample surface. PL was taken at a number of positions on each sample, and for samples that showed macroscopic inhomogeneities, measurements were recorded at small regular intervals approximately 1mm apart. Using the results from the PL mapping, a 2-D contour map of the peak emission energy or the PL intensity could be plotted across the sample plane.

3.1.4 Temperature Dependence of Photoluminescence

As most InGaN based devices are required to operate at room temperature or will be subjected to heat as a result of use, it is important to measure the effects of temperature on the optical properties of the material. From the results of temperature dependent PL measurements, information on the exciton recombination process and the effects of exciton localisation can be deduced.

Temperature dependent PL measurements were carried out using the set-up as described in Section 3.1.2. The position of the PL spot on the sample was fixed and the temperature of the sample changed using an Oxford Instruments ITC 4

temperature controller. This allows the temperature of the sample to be varied between 10K and 300K. During each run of measurements, the sample was first cooled to 10K and the PL spectrum recorded at this and increased values of temperature until the signal had dropped to ~0.1% of the initial peak intensity or could no longer be detected above background noise. From a set of measurements on a given sample, the peak emission energy, luminescence intensity and optical linewidth of the emission spectrum could then be plotted as a function of temperature.

3.1.5 Confocal Microscopy

Confocal microscopy (CM) is a planar imaging technique that uses spatial filtering by pinhole apertures to remove out-of-focus contributions to a microscopic image. Moreover, the lateral resolution of the image can be improved by a factor of up to 1.4x that compared to a standard conventional microscope [1]. CM has been applied widely to the study of biological materials, however it is still not commonly used in the study of semiconductors.

Confocal microscopy (CM) was used to examine the surface morphology of InGaN epilayer, QW and QB samples at the Daresbury Laboratories, Warrington under the guidance of Dr. Mark Tobin on the scanning confocal microscope, SYCLOPS*. The experimental set-up of the SYCLOPS scanning confocal microscope is shown in Figure 3.2 [2]. This system allows the collection of two optical images at the same

* SYnchrotron radiation for ConfocaL OPtical Scanning.

time, one due to laser light reflected from the sample surface and the other due to sample fluorescence.

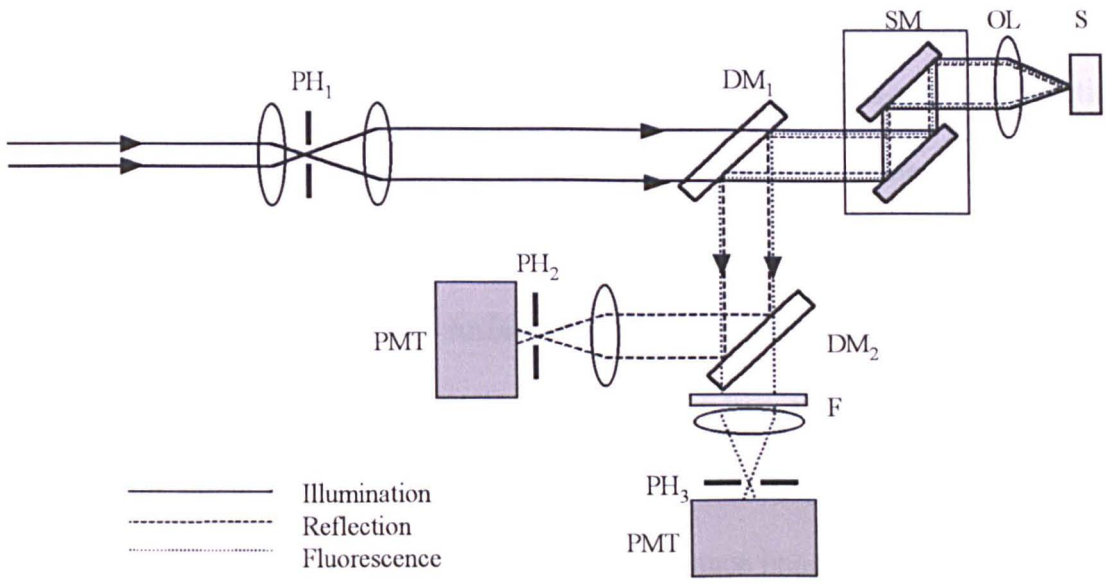

Figure 3.2: Experimental set-up of the confocal microscope, SYCLOPS.

A laser beam is focused on a source pinhole (PH_1) and collimated to a parallel beam, which is passed through a short-pass dichroic mirror (DM_1). The beam then passes onto two UV-enhanced scanning mirrors (SM) before being focused by the objective lens (OL) to a point on the sample surface (S). Reflected and fluorescence light from the sample are collected by the objective lens and retrace the path back through the scanning mirrors. At DM_1 the reflection coating on the mirror, selected for an appropriate cut-off wavelength, deflects the reflected and fluorescence light towards the detection channels. The light then travels to a second dichroic mirror (DM_2) where the coating on the mirror separates out the reflected and fluorescence light into orthogonal detection channels. Each detection channel includes a focusing lens and a pinhole aperture (PH_2 and PH_3) positioned in front of a cooled Hamamatsu R3896 PMT. The apertures are placed at the focal point of each lens, resulting in the spatial selection of light which originates only from the focal point of the objective

lens collecting light from the sample. The axial resolution of the image is therefore maintained, as light above or below the plane is rejected at the second pinhole.

A HeCd or argon ion laser was used to excite the InGaN samples with a diffraction limited laser spot focused down to approximately 1μm in diameter. To create an image of the sample, the focused beam was moved by the two scanning mirrors in a raster pattern over the sample surface and the time reference of the waveform generator, which drives the mirrors, used to trigger two slow-scan framegrabbers. The current signal from the two PMTs was then converted to voltage input to the framegrabbers to produce the reflected and fluorescence images simultaneously [1].

The area of the sample that the confocal image surveyed was dependent on the focal length of the objective lens used. The dimensions of the images were calibrated using a glass slide with a 50μm by 50μm grid pattern drawn onto it as a reference. On comparing the images obtained on the InGaN samples, high-resolution information on the spatial distribution of the sample luminescence was determined down to a length scale of ~1μm.

The SYCLOPS confocal microscope was adapted during the course of my thesis to allow PL spectroscopy and reflectance imaging to be carried out simultaneously. Placing a spectrometer with a CCD detector array in the fluorescence channel instead of the PMT, the emission spectrum from the sample was recorded. PL measurements could then be taken as either an average across the scanned sample surface or at selected points on the reflectance image by stopping the scanning at

selected points, monitored using the reflectance image on the sample surface. An initial cruder form of spectroscopy was also carried out, using the original set-up as shown in Figure 3.2 by placing a bandpass filter (F) in the path of the fluorescence beam. A series of 10nm bandpass filters ranging from 480nm to 800nm were used.

The temperature dependence of the CM images was also investigated. Using a Linkam HFS91 liquid nitrogen cooled sample stage, the temperature of the sample could be varied from 77K to room temperature.

3.1.6 Photoluminescence Excitation Spectroscopy

In photoluminescence excitation (PLE) spectroscopy, optical excitation is used to excite electrons across the bandgap of a semiconductor. However, unlike PL spectroscopy, in PLE a range of energies is used to systematically excite the semiconductor, while the intensity of emission at a selected energy is monitored. The PLE spectrum is a plot of intensity of emission as a function of the excitation energy [3].

The PLE spectrum gives similar information to an absorption spectrum: for example, it can be used to determine a value for the optical bandgap of a luminescent material. PLE spectroscopy has advantages over optical absorption techniques, as it does not require the sample substrate to be transparent at the excitation energy and is not dependent on the thickness of the material so can be used to investigate samples with thin active layers. Furthermore, features present in

a PLE spectrum can be interpreted to provide information on the absorption edge of the buffer layer or substrate material in the sample.

PLE spectroscopy was used to investigate the excitation/emission cycle of InGaN epilayer, QW and QB samples. The experimental set-up for the PLE spectroscopy measurements is shown in Figure 3.3.

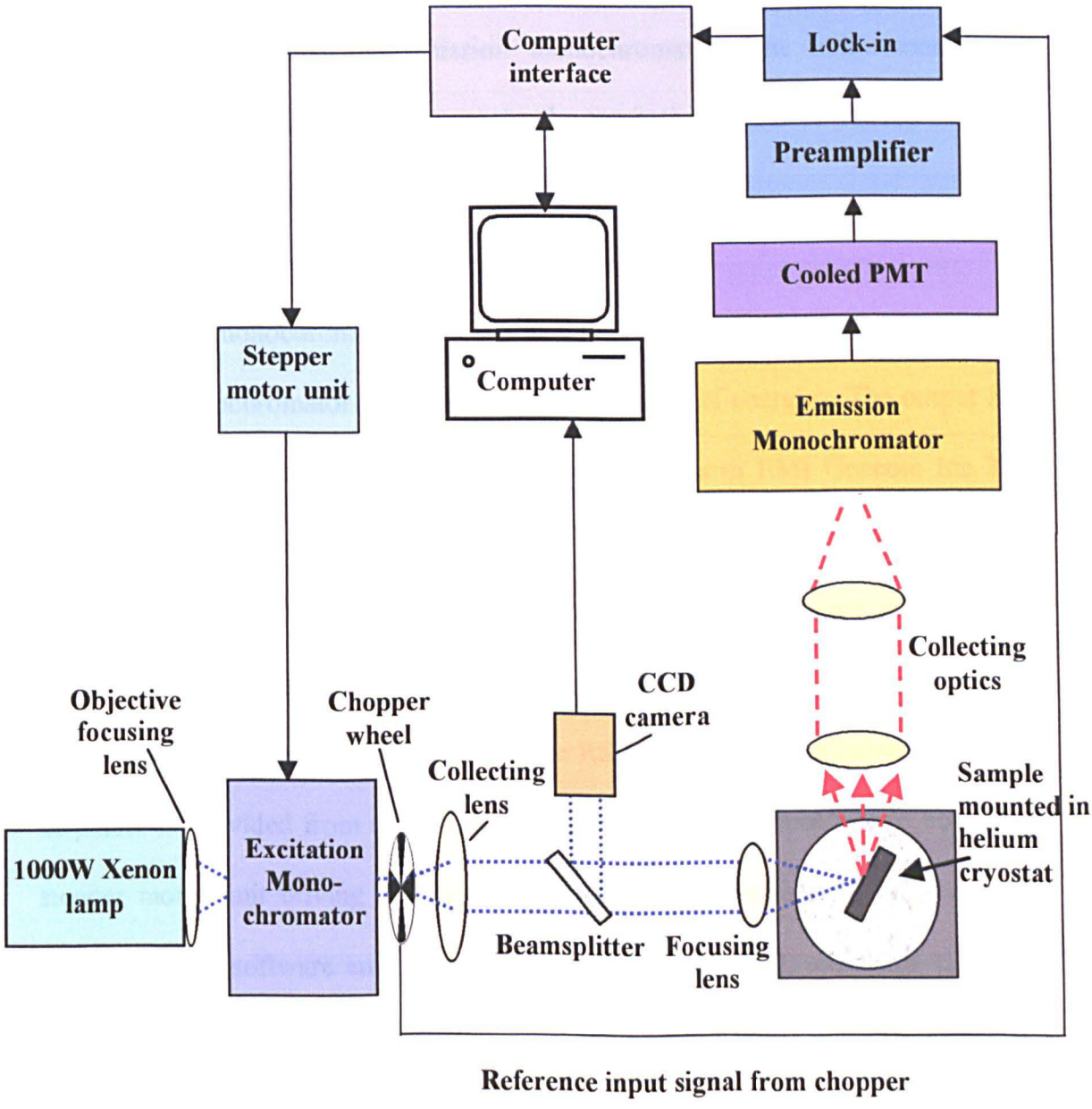

Figure 3.3: Experimental set-up for the PLE spectroscopy measurements.

A 1000W xenon lamp was used as the excitation light source. The lamp emits continuous wide band light, which was focused onto the slits of a Jobin Yvon 0.25m monochromator. This excitation monochromator scans the wide band light to produce a range of excitation energies. The output from the monochromator was then focused to a spot size of approximately 1mm square on the sample, which was mounted on the cold head of a closed-cycle helium refrigerator. Luminescence from the sample was collected and focused onto the slits of a McPherson 0.67m monochromator, termed the emission monochromator. The luminescence was collected at an angle of 60 degrees to the excitation beam to reduce reflected excitation light entering the monochromator.

The emission monochromator was set to detect light of given energy, while the excitation monochromator was scanned across a range of energies. The output from the emission monochromator was detected using a Thorn EMI Gencom Inc 3365 cooled PMT. The PMT was connected via a Stanford SR570 current preamplifier to a Stanford SR810 DSP lock-in amplifier, which used a reference signal from a chopper to distinguish emission from background noise. The resultant DC signal from the lock-in was then sent via a built in RS232 interface to a computer. A train of pulses is provided from the computer via another RS232 interface to control the stepper motor unit driving the monochromator. The measurements were recorded using in-house software and presented in the form of a PLE spectrum, the signal voltage as a function of the wavelength of the exciting light. A CCD camera was used to capture an image of the sample in the cryostat and to ensure that the position of the PLE excitation spot matched that of PL measurements from the sample. A

mirrored beamsplitter reflected an image of the sample to the camera while still allowing the excitation spot to pass through. The beamsplitter was removed before taking each PLE measurement as it reduced the excitation beam intensity.

The PLE spectroscopy experimental set-up was easily interchanged with the PL spectroscopy set-up as shown in Figure 3.1. PL measurements were taken on the InGaN sample prior to any PLE measurement in order to determine the detection energy at which the emission monochromator should be set. PLE measurements were carried out with the detection energy set at the peak emission energy of the sample and also at selected values from across the PL spectrum on either side of the peak. All the PLE spectra were corrected for the combined throughput of the xenon lamp and the excitation monochromator.

3.2 COMPOSITIONAL MEASUREMENT TECHNIQUES

3.2.1 Introduction

A series of experiments was carried out to determine the InN fraction of InGaN epilayer and QB samples. The experimental techniques used were Rutherford backscattering spectrometry (RBS), electron probe microanalysis (EPMA) and extended X-ray absorption fine structure (EXAFS). Results obtained using each of these techniques provide additional information on the sample crystallinity, surface morphology and interatomic spacing respectively.

3.2.2 Rutherford Backscattering Spectrometry

Rutherford backscattering spectrometry (RBS) is widely used as a technique for determining the composition of semiconductor alloys [4]. RBS is an important compositional measurement technique for epilayers as it allows composition values to be obtained free from the effects of strain.

All RBS measurements presented in this thesis were carried out and analysed at the University of Leuven, Belgium by Dr Andre Vantomme. RBS was used to investigate the InN fraction at different points on inhomogeneous InGaN epilayers. An ion-beam accelerator (5SDH-2 Pelletron) was used to produce an RBS probe beam of collimated 1.57MeV He^+ ions [5]. This was then directed at the InGaN sample region under investigation, with a spot size of order $1mm^2$. The probe beam was directed along a specific crystal axis, in this case aligned along the c-axis, and in a random direction, ~5° off axis. As the probe beam travels through the sample the He^+ ions have a probability of colliding elastically with the nuclei of the lattice atoms within the material. A small fraction of these ions are then scattered through a sufficiently large angle to reach a detector, which counts the number of scattered particles and measures their energy loss. An RBS spectrum can then be plotted in the form of the backscattering yield as a function of particle energy. The energy loss of the He^+ ions was measured in this way for both the aligned and random directions.

The energy of the backscattered ion depends on the mass of the nucleus it collides with: the smaller the atom, the less energy the backscattered ion has. In addition, as the scattering probability depends on the energy of the ions and as the ions lose

energy continuously as a result of electronic interactions, then the probability of a collision occurring increases as the probe beam travels further through the sample. By using a multi-layer model computer simulation of an RBS spectrum, values for the composition and layer thickness of the material can therefore be estimated. The simulation model generated, using the experimental conditions as input parameters, was varied by changing the composition and thickness values in the model until it matched the measured RBS spectrum taken in the random direction.

Information on the crystalline quality of the material was also obtained from the data fitting. The crystalline quality of a semiconductor is quantified by χ_{min}, the ratio of the backscattering yield along the aligned direction, to that in the random direction, in the near surface region. χ_{min} is usually given as a percentage: a value of a few percent indicates good crystalline quality and 100% an amorphous or polycrystalline material.

PL spectroscopy measurements taken on InGaN epilayers were carried out in advance of the RBS measurements. This was done because long exposure to the RBS probe beam was found to lower the PL efficiency of the addressed spot.

3.2.3 Electron Probe Microanalysis

The electron probe microanalyser (EPMA) is a non-destructive diagnostic technique that can be used to determine compositional information, with a spatial resolution on order of 1μm. The EPMA works by bombarding materials with a focused electron probe beam and analysing the X-ray photons emitted by the various elements in the

material [6,7]. As the wavelengths of X-ray lines are characteristic of the emitting species, the material composition can be identified. EPMA has major applications in geochemistry, microelectronics, biochemistry and material science [6].

All the EPMA measurements presented in this thesis were taken at the University of Montpellier, France under the guidance of Dr. Claude Merlet. A CAMECA SX100 EPMA, as shown in Figure 3.4 [8], was used to measure the indium nitride content of a macroscopically inhomogeneous InGaN epilayer at several different positions on the sample. Correction of the EPMA raw data was performed by Dr. Merlet using the CAMECA 'Layers' programme.

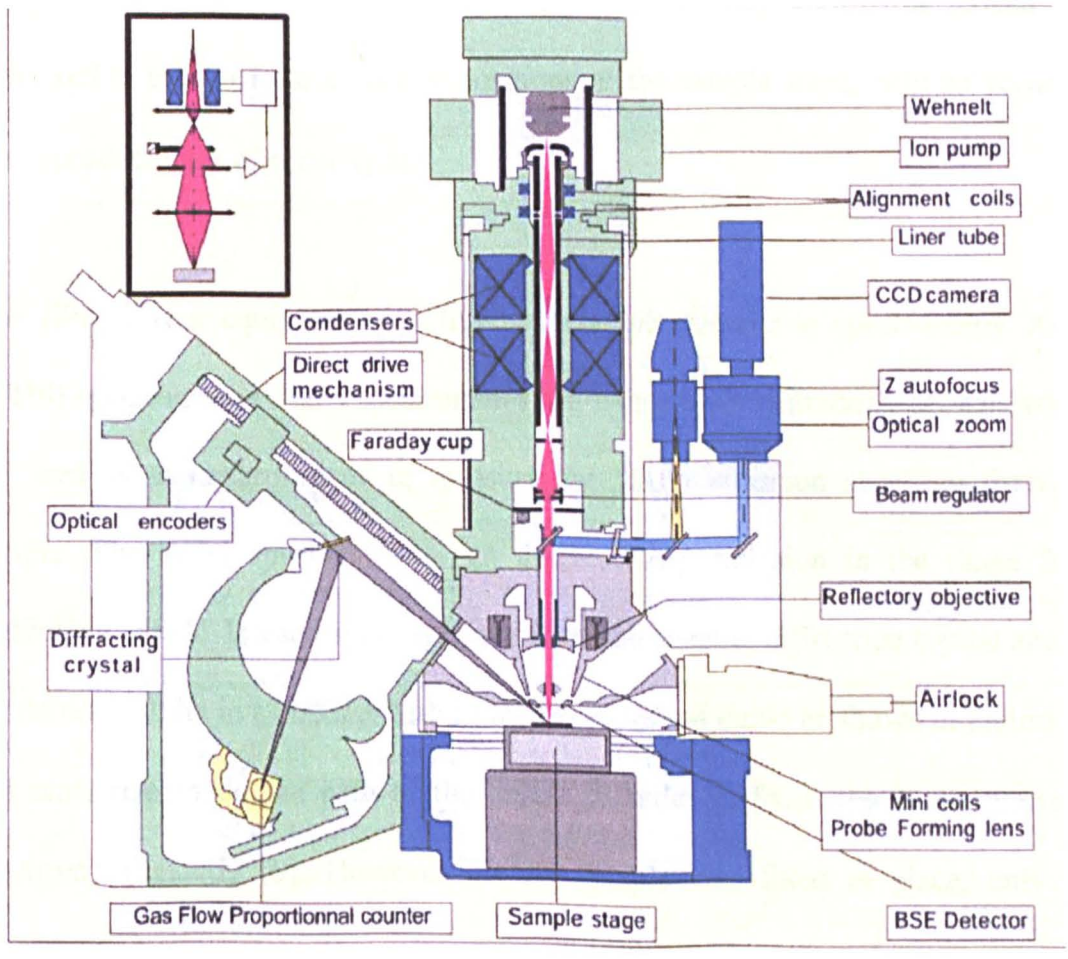

Figure 3.4: Schematic diagram of the SX100 EPMA.

The accelerating voltage of the EPMA electron probe beam can be adjusted in steps from 1kV up to 50kV. In these measurements accelerating voltages of 5kV and 10kV were selected. X-ray emission was excited using a stationary focused electron probe beam ~100nm in diameter, with a beam current of only 10nA to avoid irradiation damage and heating of the sample. The sample was placed on a stage and put under vacuum. During the experimental set-up the sample was viewed optically in reflected light by a CCD camera with high magnification (x2000) to observe the surface quality of the material and to select an area for measurement. Cathodoluminescence of the sample was simultaneously observed in this set-up and monitored as the position of the probe beam was moved across the sample surface. Computer automation of the instrument allowed the beam spot to be moved and measured in terms of the x- and y- positions of the sample stage, with an accuracy and reproducibility of order 1μm.

The EPMA was equipped with five wavelength dispersive spectroscopy X-ray (WDS) spectrometers. Each spectrometer has two or four diffraction crystals which are used as monochromators to measure the X-ray emission spectrum from the sample. The WDS spectrometers can detect X-ray emission in the range from ~100eV to 14keV. In each WDS spectrometer, the sample, diffraction crystal and X-ray detector all lie in a circular path called the Rowland circle as shown in Figure 3.5 and must remain on the path of this circle in order to focus the X-ray emission spectrum efficiently [9]. However, as the sample was fixed in place, only the diffraction crystal and the X-ray detector could be moved.

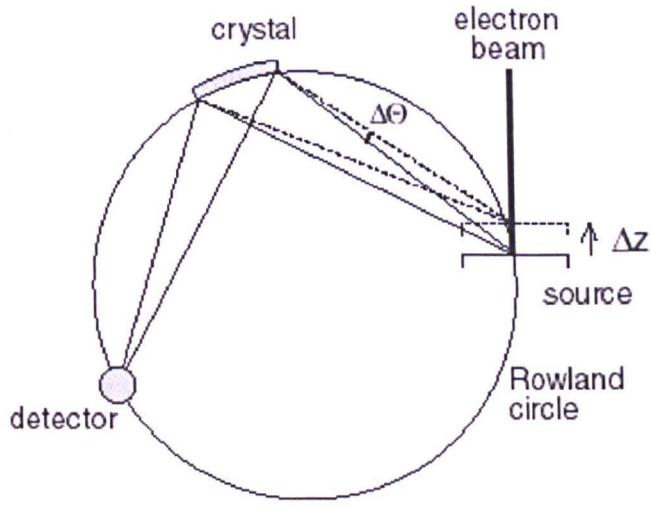

Figure 3.5: WDS spectrometer set-up with the components positioned at points on the Rowland circle.

The diffraction crystal is curved to focus the diverging beam of emitted X-rays and only diffracts those X-rays that satisfy the Bragg condition [10]. An appropriate diffraction crystal must therefore be selected to diffract the required X-ray emission from the sample.

The X-ray emission of gallium (1.098keV) and indium (3.287keV) were measured by the diffraction crystals TAP (thallium acid phthalate; 2d: 25.75Å) and LPET (large pentaerythritol; 2d: 8.74Å). The diffraction crystal is rotated about the centre of the Rowland circle until the input to the X-ray detector is maximised. The high spectral resolution of the WDS system produced high peak to background ratios; 40:1 and 50:1 for gallium and indium respectively for the InGaN sample at a probe beam energy of 10keV. A 40-second counting time on the peak detection intensity and 20 seconds on the background was used. Furthermore, for some spots, the X-ray emission of carbon was measured on a PC2 pseudocrystal (a Ni/C multilayer;

2d: 100Å). This was done to estimate a value for any carbon contamination that may have occurred on the sample surface and to minimise the error in the measurement of the indium nitride fraction that could be related to the presence of a surface contamination layer.

The sample signals were compared with the X-ray intensities from materials with known composition, namely standard samples of GaAs and InSb. The intensity ratio of the sample signal against the standard signal was converted to atomic fractions using both analytical and numerical models. These models were based on the calculation of the distribution profile of the X-rays emitted from a target point on the sample. Composition values at selected points across the sample surface were thus obtained.

3.2.4 Extended X-Ray Absorption Fine Structure

In an X-ray absorption spectrum there may be additional fine structure present above the absorption edge of the spectrum. This effect, known as extended X-ray absorption fine structure (EXAFS), is due to the interference between outgoing and backscattered photoelectrons produced by the absorption of X-rays in a target atom. An EXAFS measurement is a non-destructive method to determine the local structure of materials, however its use in the investigation of III-nitrides is at present fairly uncommon.

EXAFS was used to probe the local nanostructure of InGaN epilayers and an uncapped QB sample on an atomic length scale. The EXAFS measurements

presented in this thesis were obtained at Station 9.2 of the Daresbury Laboratories, Warrington. Modelling of the EXAFS spectra were carried out by Dr. Fred Mosselmans using the Daresbury laboratories computer programmes EXCALIB and EXBROOK and analysed in EXCURV98 [11].

During an EXAFS measurement the photon energy of the X-ray beam incident on the sample is scanned through a chosen elemental edge. When the photon energy is sufficient to excite the electrons of the element then a large increase in X-ray absorption occurs, labelled by the electron shell letter, K, L, M... which denotes the initial state. The absorbed X-rays ionize the atom and an electron is emitted as a spherical wave with energy equal to that of the incoming photon minus the binding energy of the electron. Self-interference of the photoelectrons occurs as they propagate from the target atom and scatter back from neighbouring atomic shells, as shown in Figure 3.6 [12].

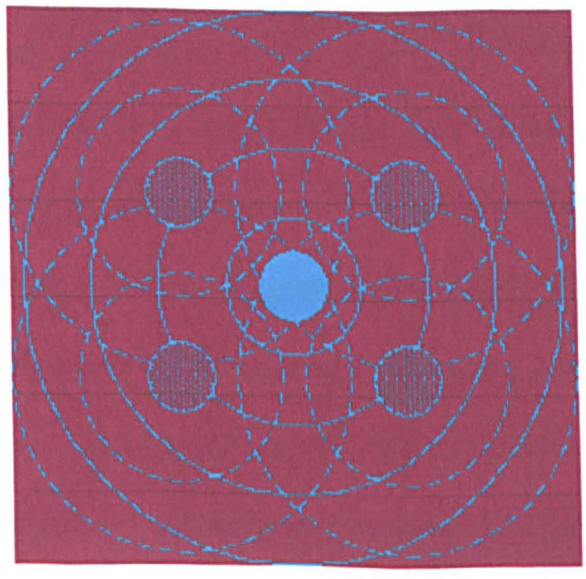

Figure 3.6: Diagram of the photoelectron spherical wave (solid line) being backscattered by the neighbouring atoms (dotted lines).

These interference effects produce regions of constructive and destructive interference and result in the EXAFS oscillations above the edge in the X-ray absorption spectrum. The amplitude and phase of the scattered photoelectron wave depends on the number and type of scattering atom and the distance between the emitting and scattering atoms, the shell radii [12]. Therefore, the EXAFS can be used to determine the atomic number, radial separation and co-ordination number of the atoms surrounding those atoms whose absorption edge is being examined.

The most common X-ray source for EXAFS is synchrotron radiation as it provides an intense and tunable source to scan over the absorption edge of the selected element. The Daresbury laboratories' synchrotron storage ring operates at 2GeV with currents between 120 and 250mA. The EXAFS measurements were carried out above the indium absorption edge, subsequently referred to as the indium K-edge, to investigate the local nanostructure surrounding the indium atom. The incident X-ray beam was swept through the indium K-edge near 27,800eV. The EXAFS spectrum was monitored in the fluorescence mode where the fluorescent X-ray flux is measured as a function of the incident X-ray flux. This is similar to PLE. A Canberra solid state Ge detector was used to record each EXAFS spectrum and a silicon (220) double-crystal monochromator detuned to 70% of its maximum response to suppress harmonic contamination of the signal. The monochromator was calibrated using a piece of indium foil, and EXAFS taken on a high quality sputtered layer of pure InN used as a calibration standard for both the data acquisition and modelling. Individual EXAFS scans were summed in order to obtain adequate quality data for modelling.

The InGaN samples were kept at room temperature during the EXAFS measurements. Only samples with an InN fraction of 10% or above were investigated. This is because the sample absorption decreases with indium content, making the EXAFS signal more difficult to obtain. Furthermore, when the indium content is low, the data fitting fails to discriminate between atomic configurations with similar structures [13].

EXAFS of a model environment is synthesised and then systematically refined, shell by shell, in an attempt to match the experimental results or its Fourier Transform. The ratio of atoms present in each of the shells fitted to the results allows the InN composition of the sample to be determined.

3.3 Summary

In this chapter, the optical characterisation and compositional measurement techniques used to investigate InGaN epilayer, QW and QB samples are described. PL spectroscopy measures the emission spectrum of the sample. PLE spectroscopy is used to determine the optical bandgap of the sample. In conjunction with PL, PLE can be used to investigate the excitation/emission cycle of the sample. Confocal microscopy examines surface morphology. From the microscope images the spatial distribution of the sample luminescence can be determined down to a length scale of ~1μm; whereas in PL and PLE spectroscopies, the spectrum is taken from an area of the sample excited by a beam spot ≥100μm. The composition of the samples was obtained using three different techniques RBS, EPMA and EXAFS. These techniques can determine the composition free from the effects of strain on the

material. RBS measurements give additional information on crystalline quality, however it has been found to lower the PL emission of the sample. EPMA has the advantage that it has spatial resolution on the order of 1μm. From EXAFS the interatomic spacing and disorder effects in the material can be determined. The results from each of these different techniques can be compared and analysed for trends.

3.4 References

[1] M. J. Tobin, M. Martin-Fernandez and G. R. Jones, Synchrotron Radiation News, **11**, 24 (1998).

[2] K. P. O'Donnell, M. J. Tobin, S. C. Bayliss and W. Van der Stricht, Jnl. of Microscopy, **193**, 1 (1998).

[3] P. Y. Yu and M. Cardona, *Fundamentals of Semiconductors, Physics and Materials Properties*, Springer, Germany (1996).

[4] W. K. Chu, J. W. Mayer and M. A. Nicolet, *Backscattering Spectrometry*, Academic, New York (1978).

[5] M. F. Wu, S. Yao, A. Vantomme, S. M. Hogg, G. Langouche, J. Li and G. Y. Zhang, J. Vac. Sci. Technol. B **17**, 1502 (1999).

[6] CAMECA website: http://www.cameca.fr/html/epma_technique.html.

[7] J. I. Goldstein, D. E. Newbury, P. Echlin, D. C. Joy, A. D. Romig, Jr., C. E. Lyman, C. Fiori and E. Lifshin, *Scanning Electron Microscopy and X-ray Microanalysis*, Second Edition, Plenum Press, USA (1992).

[8] CAMECA website: http://www.cameca.fr/doc_en_pdf/sxsynoptique.pdf.

[9] CAMECA website link: http://jan.ucc.nau.edu/~wittke/Microprobe/WDS.html.

[10] P. E. J. Flewitt and R. K. Wild, *Physical Methods For Materials Characterisation*, IOP Publishing Ltd., London (1994).

[11] N. Binsted, EXCURV98, CCLRC Daresbury Laboratories Computer Program (1998).

[12] Daresbury Laboratories website: http://srs.dl.ac.uk/XRS/Theory/theory2.html.

[13] K. P. O'Donnell, J. F. W. Mosselmans, R. W. Martin, S. Pereira and M. E. White, J. Phys.: Condens. Matter. **13**, 6977 (2001).

CHAPTER 4: PHOTOLUMINESCENCE CHARACTERISATION OF InGaN EPILAYERS

4.1 Introduction

Photoluminescence (PL) spectroscopy of InGaN yields information on the radiative properties of the material. Low temperature PL spectroscopy was carried out with the exciting laser, incident at different points across the surface of selected samples, to determine the degree of uniformity of the emission. Temperature dependent PL measurements were taken on two of the InGaN samples to discover how the peak emission energy, spectral linewidth and the integrated emission intensity vary with temperature. The recombination processes occurring in the material could then be interpreted.

PL spectroscopy was performed using the experimental set-up described in Chapter 3, Section 3.1.2. Growth and structural details on each of the investigated InGaN epilayers are given in Appendix A, Section A.1.1.

4.2 PL Spectroscopy Results

Typical PL spectra taken at 10K from several InGaN samples are shown in Figure 4.1. The peak emission energies were measured directly from the graph to be ~3.30eV, 2.61eV, 2.36eV and 1.53eV for samples InGaN 131, 85, 331 and 336 respectively. As is evident from Figure 4.1, the peak emission energy of InGaN PL can be tuned across the entire range of the visible spectrum and beyond. It is this property, along with the high quantum efficiency of the material, which make the

use of InGaN in optoelectronic devices so attractive. A decrease in the peak emission energy of InGaN has been found to scale with an increase in the indium nitride content in the material; this observation will be discussed in detail in Chapter 5. Each PL spectrum presented in Figure 4.1 has been normalised to unit intensity and corrected for the wavelength variation of the monochromator and detector responses. Details of the monochromator and detector response correction procedure are outlined in Appendix B, Section B.1.

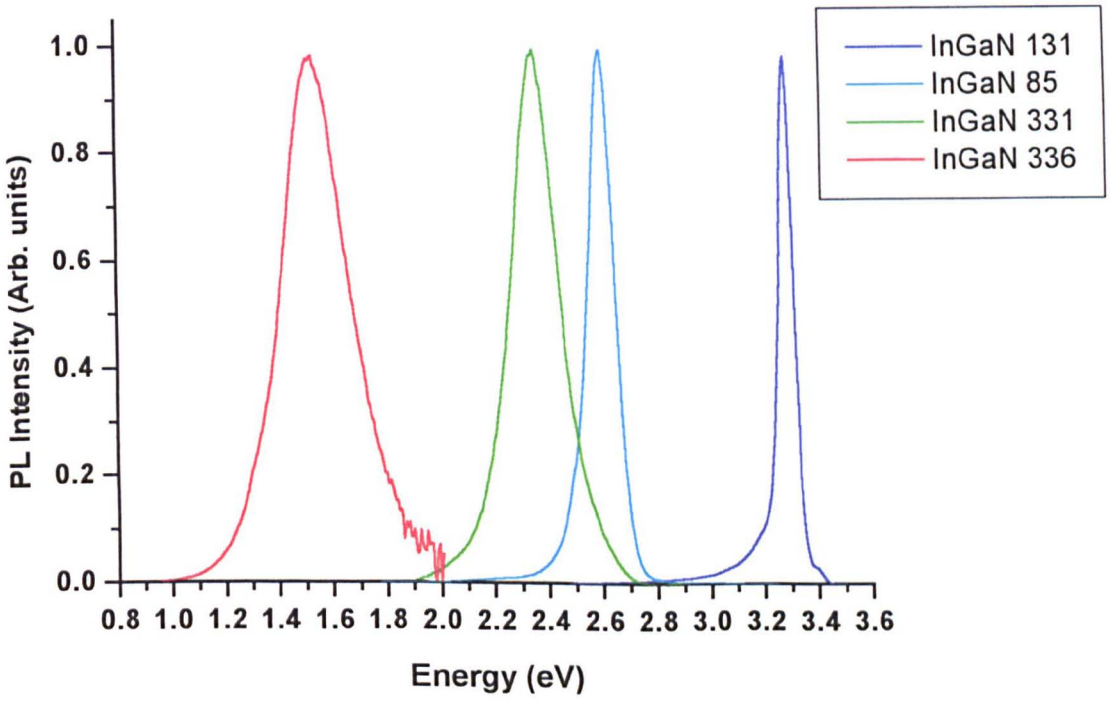

Figure 4.1: Typical PL spectra taken at 10K from a number of InGaN epilayer samples.

The PL spectra in Figure 4.1 all possess the same general shape: a single broadband feature with approximately exponential tails on both the high and low energy sides.

The linewidth of the emission spectrum measured at half of the peak intensity, referred to as the full width at half maximum (FWHM), broadens from 0.06eV, 0.115eV, 0.20eV to 0.29eV for samples InGaN 131, 85, 331 and 336 respectively. As shown in Figure 4.2 there is a notable increase in the linewidth with decreasing peak emission energy.

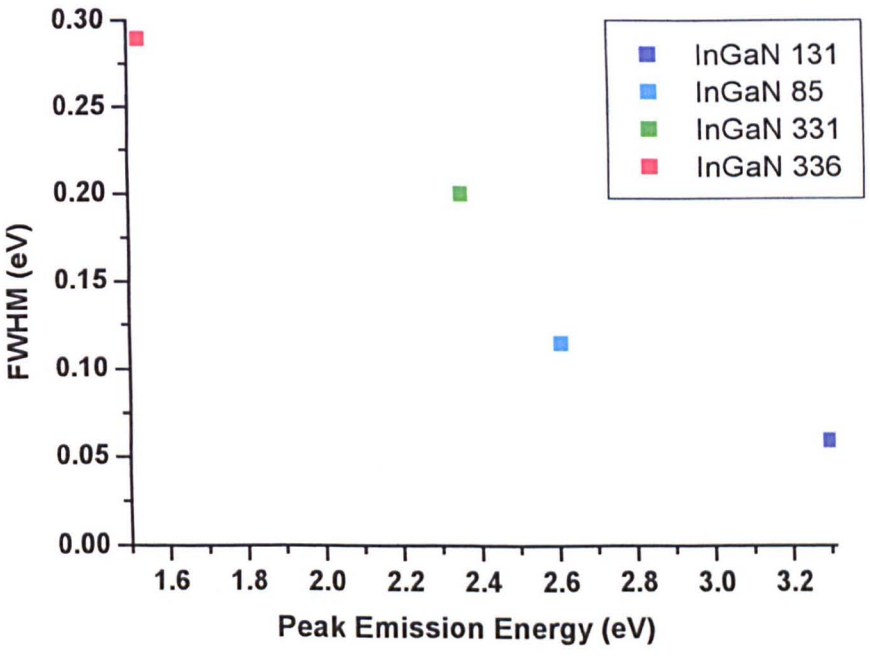

Figure 4.2: Linewidth plotted against peak emission energy for the PL spectra shown in Figure 4.1.

4.3 Low Temperature PL Mapping Results

PL mapping as outlined in Chapter 3, Section 3.1.3 was carried out on the samples.

4.3.1 Peak Emission Energy Maps

The peak emission energy at 10K was approximated from the PL spectrum by eye, using a computer x-hair function to read the corresponding values for the x and y co-ordinates at the spectral peak. These results were verified by fitting a Gaussian

equation to the PL spectrum. The peak emission energy b, was determined from a fit to equation 4.1;

$$y = a \exp\left(-\frac{(x-b)^2}{c}\right) \qquad \textbf{Equation 4.1}$$

where a is the amplitude of the PL spectrum, x the emission energy at which the intensity, y, is recorded and c is a broadening parameter related to the FWHM as shown in equation 4.2;

$$FWHM = 2\sqrt{c\ln 2} \qquad \textbf{Equation 4.2}$$

The peak emission energies obtained from the fittings were found to be consistent to within 10meV of the values approximated by eye.

The PL maps of the samples are generated from the peak emission energies obtained. As the network of measured data points is incomplete the computer package Origin 6.0 was used to interpolate values between the results in order to produce the final map. The data was then plotted in the form of a 2-D contour map showing the variation in the peak emission energy across the sample surface. Low temperature PL maps for samples InGaN 131, 85, 331 and 336 are shown in Figures 4.3 to 4.7. Sample InGaN 336 was split into two separate pieces labelled 336A and 336X and the PL map plotted for each piece individually. As some of the sample shapes are irregular, each PL map has been adjusted to maintain the aspect ratio of the sample. Typical peak emission energies obtained from the samples are shown at the appropriate positions on the figures.

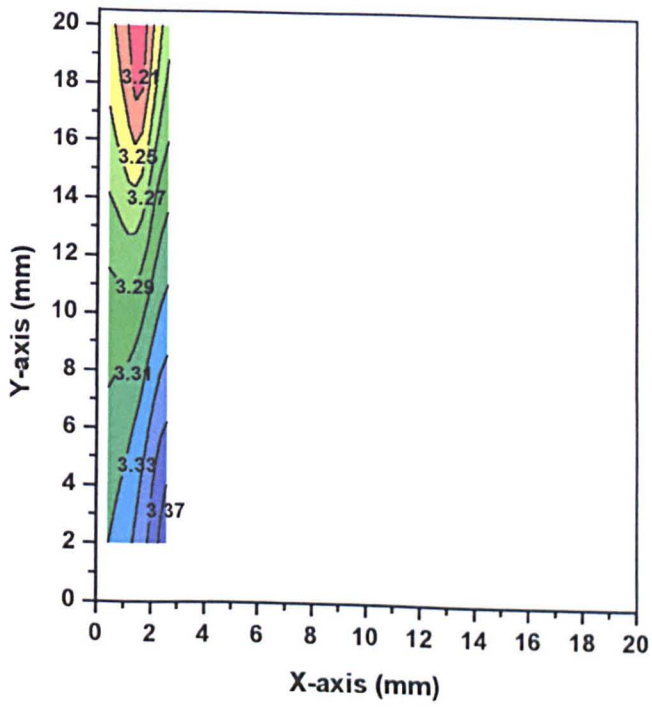

Figure 4.3: Low temperature PL map of sample InGaN 131.

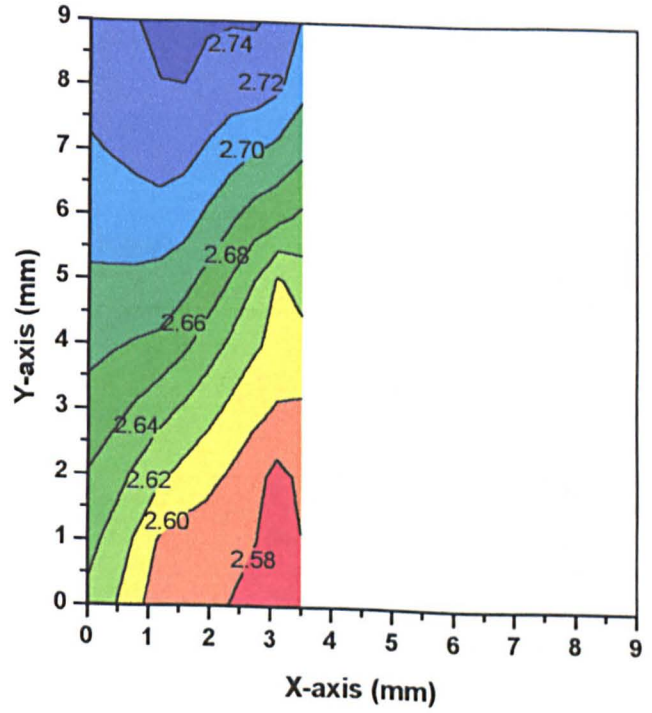

Figure 4.4: Low temperature PL map of sample InGaN 85.

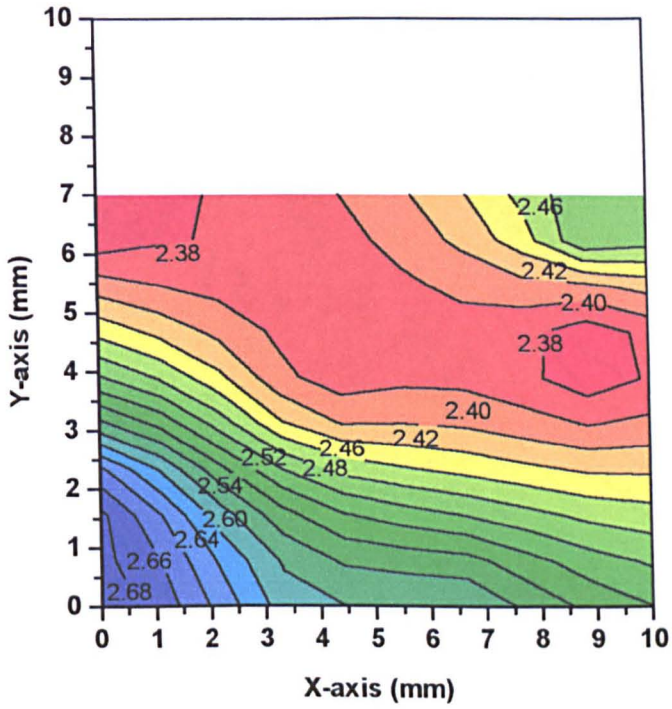

Figure 4.5: Low temperature PL map of sample InGaN 331.

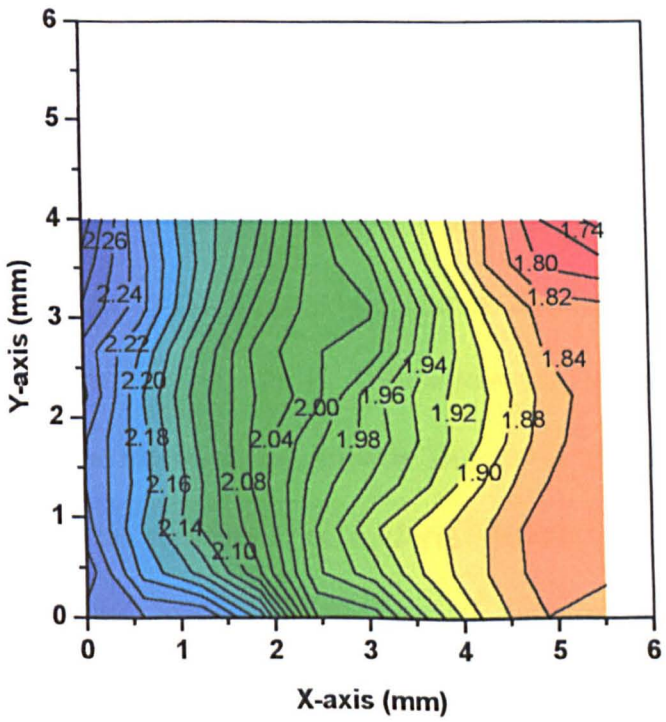

Figure 4.6: Low temperature PL map of sample InGaN 336A.

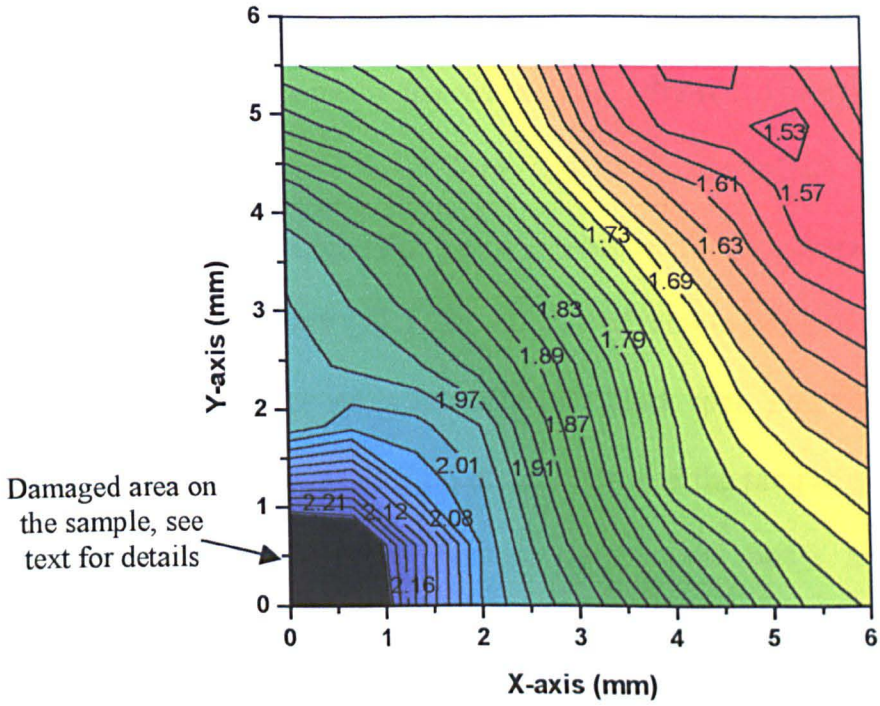

Figure 4.7: Low temperature PL map of sample InGaN 336X.

Figures 4.3 to 4.7 show that each of the InGaN samples exhibits macroscopically inhomogeneous emission. From the PL maps the variation in the peak emission energy appears to be more pronounced in certain directions across the surface. A sequence of peak emission energy contours runs in particular directions over the sample. The patterns in the peak emission energy may be identified with radial variations of the incorporation rate of InN across the sample as a result of a temperature gradient produced during growth. Due to the temperature sensitivity of InGaN composition the realisation of uniform growth over the wafer is very difficult. However, by increasing the sample rotation speed a significant improvement in the uniformity can be obtained [1].

The PL maps in Figures 4.6 and 4.7 for the two pieces of InGaN 336 reveal a unique piece of InGaN that emits in the red and near infra-red. The peak emission energy of InGaN 336A is as low as ~1.74eV and of sample InGaN 336X ~1.53eV. Both samples exhibit peak emission energies well below the generally accepted bandgap energy of InN, ~1.89eV [2]. In the PL map of sample InGaN 336X, a region of very weak or no luminescence is indicated by a black spot. This was caused by the high energy ion beam used in an RBS measurement of the sample. The RBS probe beam, previously reported not to damage the material under investigation [3], has deleteriously affected the emission properties of the sample in the region addressed by the beam.

4.3.2 Integrated Emission Intensity Map of Sample InGaN 336X

During the PL mapping of sample InGaN 336X, it was noted that the luminescence intensity of the emission spectrum varied considerably across the sample surface. The total emission intensity of each spectrum was measured by integrating the area under the PL spectrum. A 2-D contour map of the integrated emission intensity across the sample was plotted as shown in Figure 4.8. An overlay of the intensity map with the peak emission energy map is shown in Figure 4.9.

From Figures 4.8 and 4.9, ignoring the damaged area around the RBS spot, a decrease in the luminescence intensity with increasing peak emission energy is observed going diagonally across the sample from co-ordinates (1, 1) to (6, 5.5). There are also two areas of poorer intensity at co-ordinates (4, 1.3) and (3.9, 3.5).

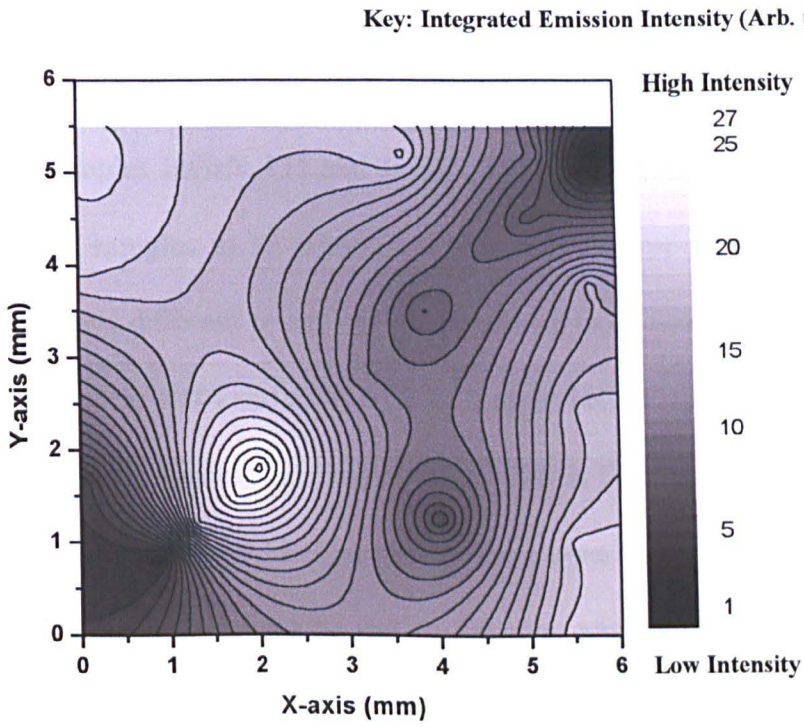

Figure 4.8: Integrated emission intensity map of sample InGaN 336X.

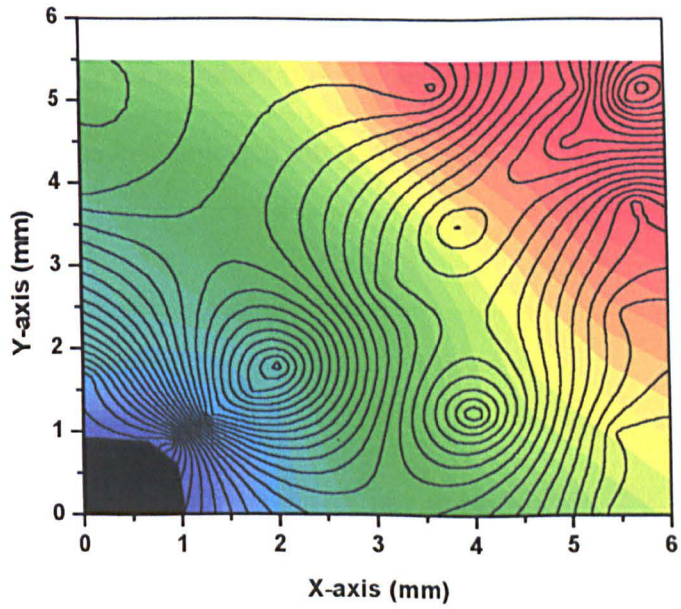

Figure 4.9: Overlay of the integrated emission intensity map contours with the peak emission energy map for sample InGaN 336X.

4.4 Temperature Dependence of PL Spectra Results

Temperature dependent PL measurements were carried out as outlined in Chapter 3, Section 3.1.4 on samples InGaN 131 and InGaN 85. Since PL mapping had shown the emission of the samples to be inhomogeneous, each set of measurements was taken from at least two different points on the sample surface. These points are given by the co-ordinates (1.5, 10.0) and (2.5, 3.0) on sample InGaN 131 shown in Figure 4.3 and (3.0, 8.5), (1.5, 1.0) and (2.0, 0.5) on InGaN 85 in Figure 4.4. The PL results are shown in Figures 4.10 and 4.11. The spectra have been plotted on a log scale to allow them to be viewed more clearly and to examine any additional sidebands in the spectrum. The exciting laser line is present in some of the spectra shown in Figure 4.11 b) and c).

In each set of measurements the spectrum is dominated by a high energy emission peak. With increasing temperature this feature was found to shift in energy, change its width and decrease in integrated intensity.

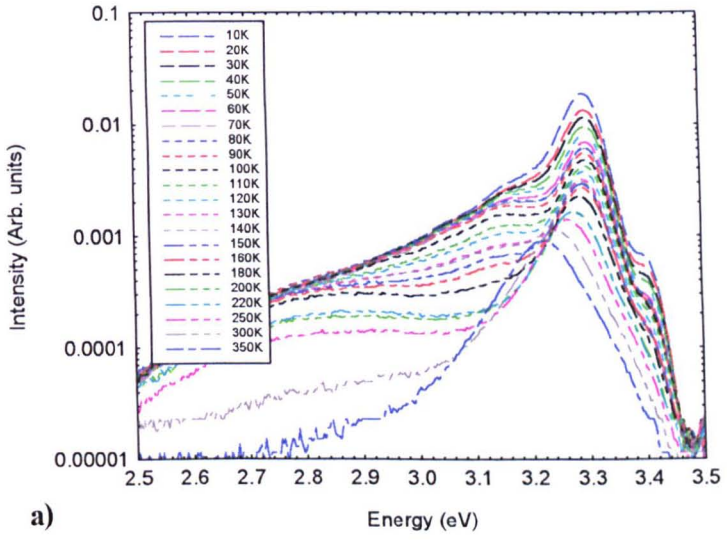

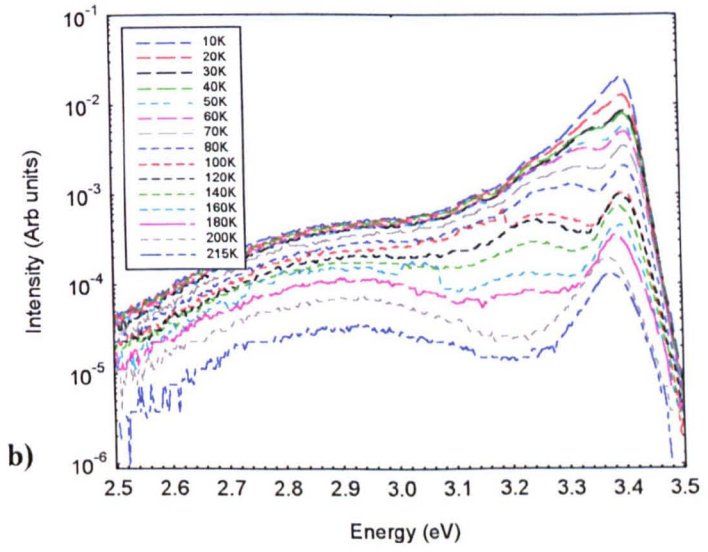

Figure 4.10: Temperature dependent PL spectra from InGaN 131 taken at co-ordinates a) (1.5, 10.0) and b) (2.5, 3.0).

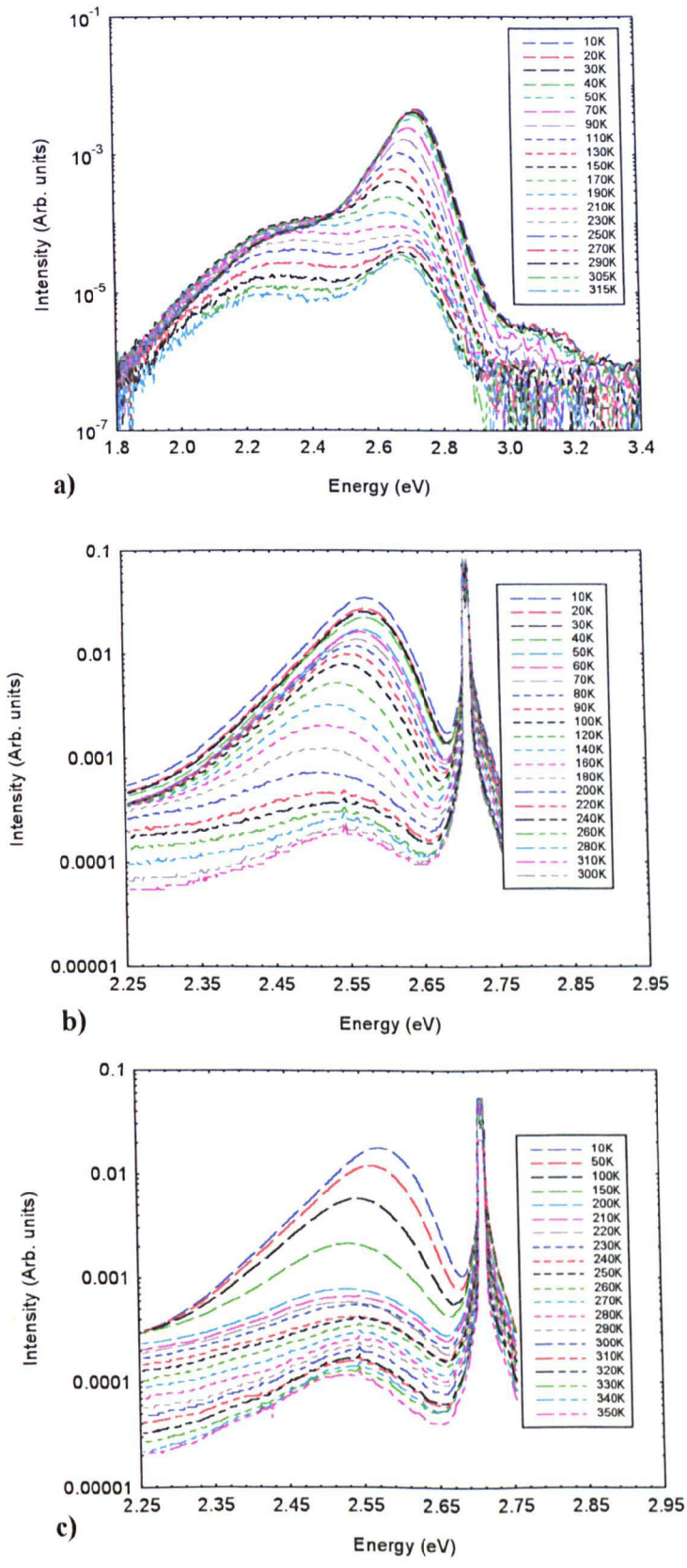

Figure 4.11: Temperature dependent PL spectra from InGaN 85 taken at co-ordinates a) (3.0, 8.5) b) (1.5, 1.0) and c) (2.0, 0.5).

From the PL spectra of InGaN 131, shown in Figure 4.10, weak sidebands were observed on the low energy side of the main peak. These sidebands were found to vary differently with temperature compared to the main feature and in some cases, at sufficiently high temperatures, disappear from the spectrum altogether. In Figure 4.10a) another small peak at 3.40eV indicates that the GaN layer underneath the InGaN is being excited.

From the PL spectra of InGaN 85, shown in Figure 4.11, an additional band can be seen at ~2.25eV in Figure 4.11a); this is the yellow band. The origin of yellow band emission in InGaN remains unclear but it is often found in the emission spectrum from material with poor crystalline quality and is thought to originate in the GaN buffer layer as a result of donor-to-acceptor transitions [4,5]. However, in Figure 4.11 b) and c) there is no evidence of any yellow band emission or additional sidebands. These measurements were carried out using a lower energy exciting laser line than those in a).

4.4.1 Peak Emission Energy as a Function of Temperature

Using the method outlined in Section 4.3.1 the peak emission energy was obtained and plotted as a function of temperature. The results are shown in Figures 4.12 and 4.13.

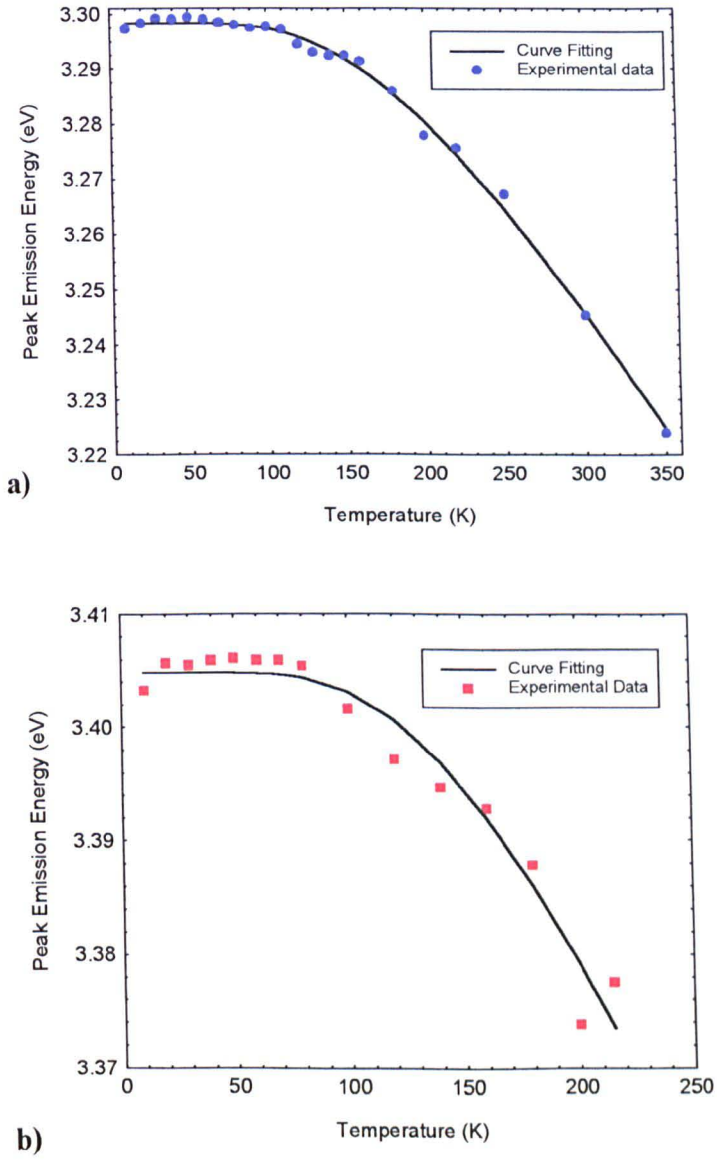

Figure 4.12: Peak emission energy as a function of temperature for sample InGaN 131 taken at co-ordinates a) (1.5, 10.0) and b) (2.5, 3.0).

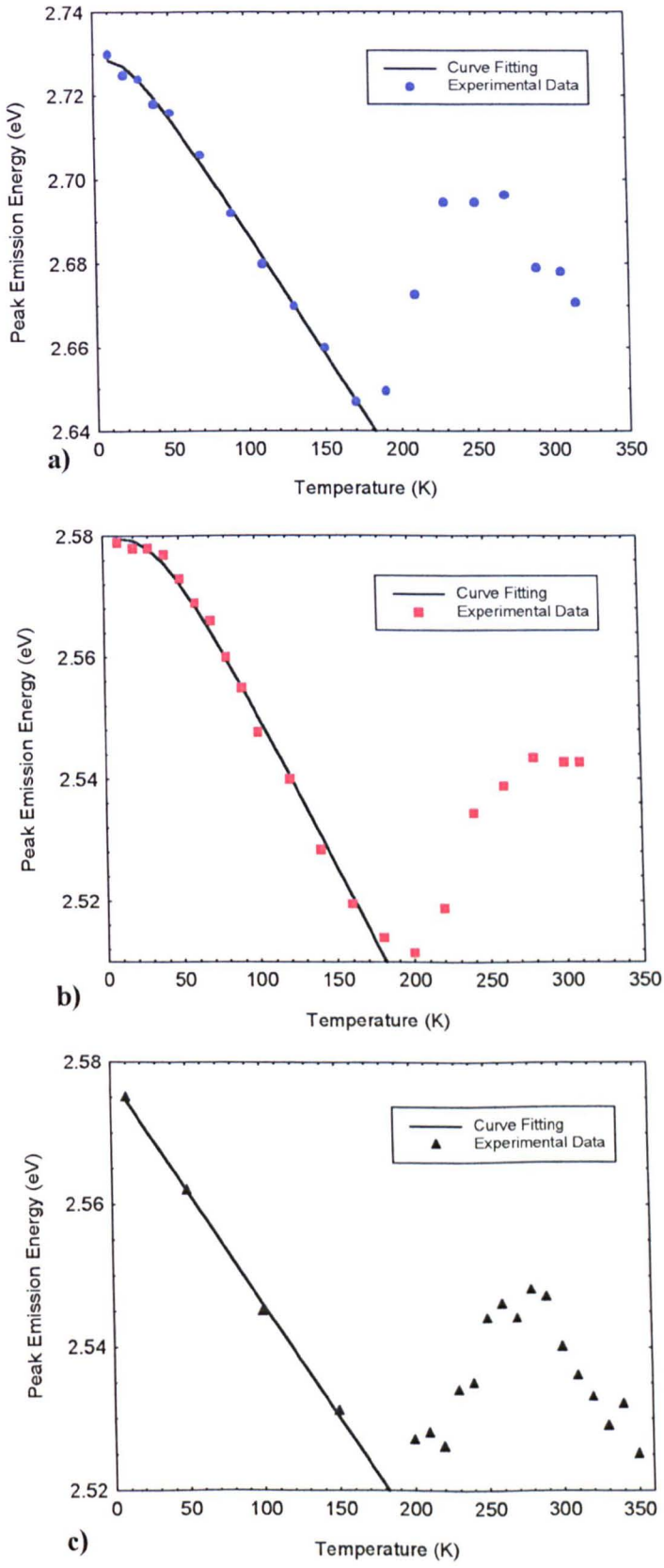

Figure 4.13: Peak emission energy as a function of temperature for sample InGaN 85 taken at co-ordinates a) (3.0, 8.5), b) (1.5, 1.0) and c) (2.0, 0.5).

The relationship between peak emission energy and temperature is very different for the two investigated samples. In sample InGaN 131 the peak emission energy decreases gradually with an increase in temperature, as shown in Figure 4.12. In sample InGaN 85 a variation of peak emission energy with rising temperature is observed. As shown in Figure 4.13 at temperatures up to ~190K an initial redshift is obtained beyond which the peak emission energy begins to blueshift. At temperatures above 280K the peak emission energy then starts to redshift again. This pattern of red-blue-red shift is known as 'S'-shape temperature dependence [6].

4.4.2 FWHM as a Function of Temperature

The FWHM was measured from each spectrum using the method outlined in Section 4.2 and the results plotted as a function of temperature, as shown in Figures 4.14 and 4.15.

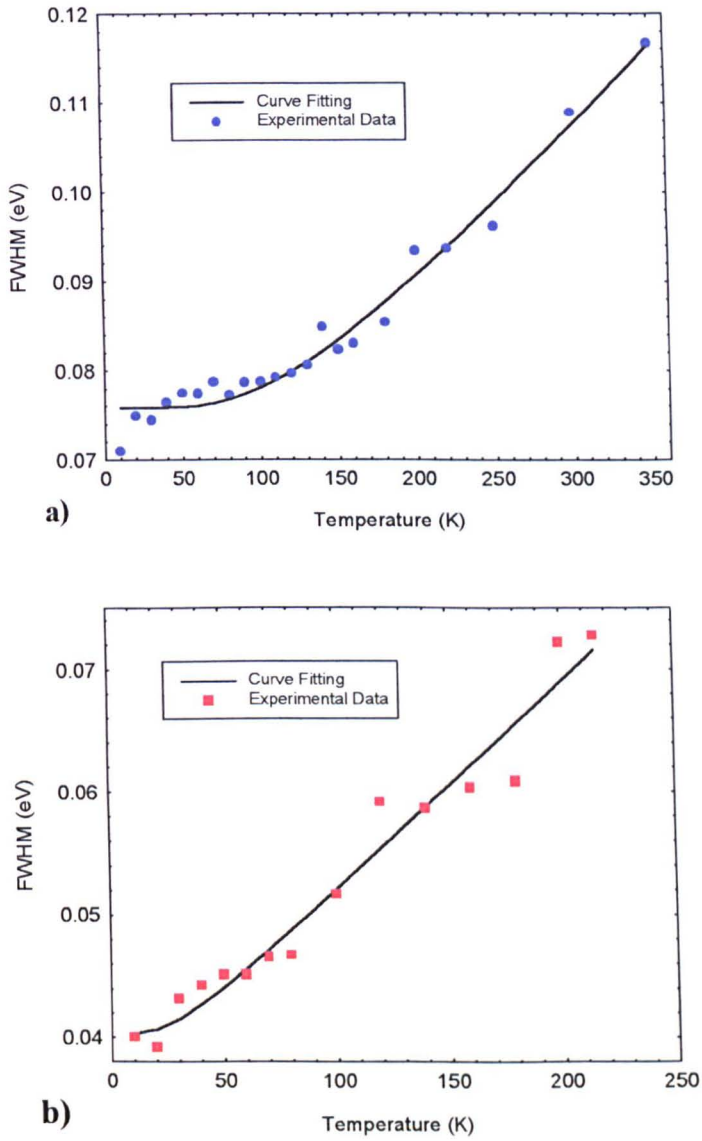

Figure 4.14: FWHM as a function of temperature for sample InGaN 131 taken at co-ordinates a) (1.5, 10.0) and b) (2.5, 3.0).

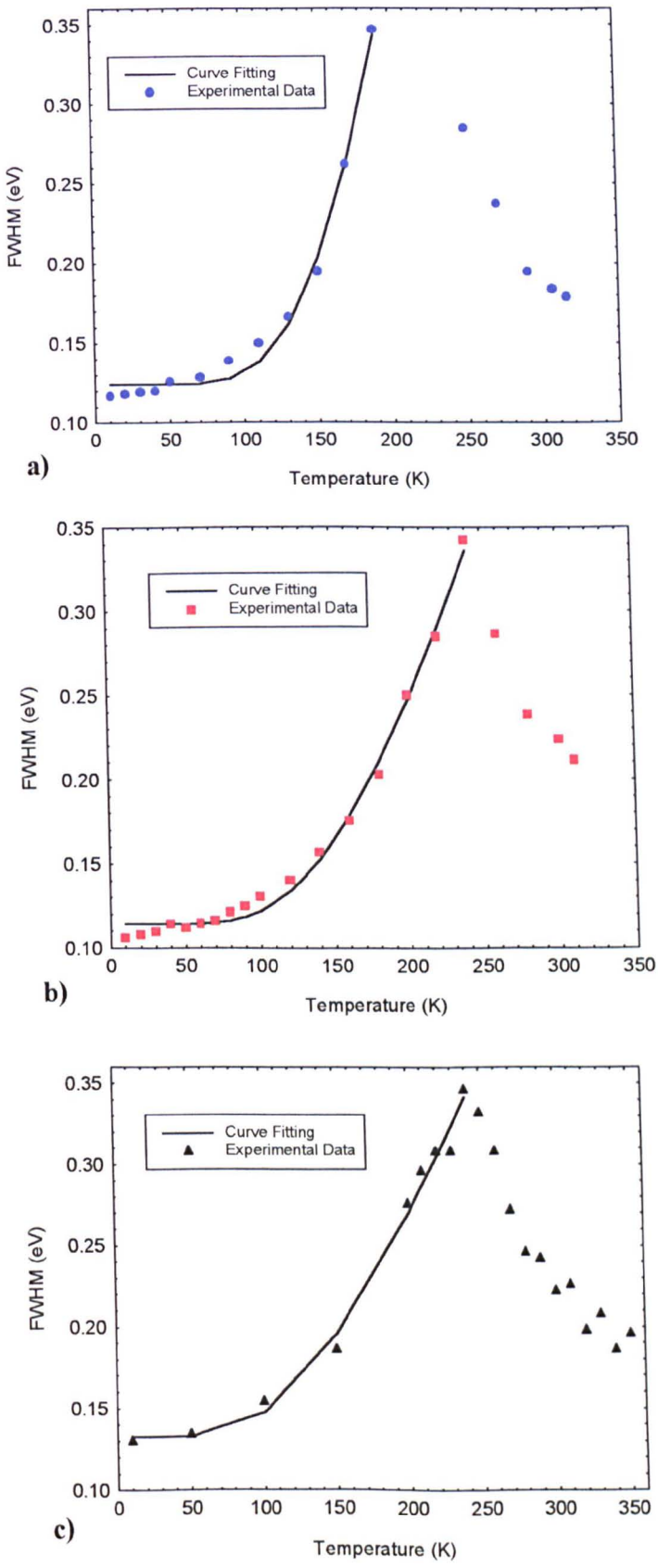

Figure 4.15: FWHM as a function of temperature for sample InGaN 85 taken at co-ordinates a) (3.0, 8.5), b) (1.5, 1.0) and c) (2.0, 0.5).

For sample InGaN 131 the FWHM broadens with an increase in temperature. In addition, on comparing Figure 4.14 a) and b) at a given temperature, a decrease in the FWHM value with an increase in the peak emission energy from Figure 4.12 a) and b) was found. For sample InGaN 85, as shown in Figure 4.15, the FWHM broadens steeply with increasing temperature up to ~240K before dropping sharply. However, it should be noted that in Figure 4.15a), although the same general trend in the FWHM occurs, the temperature at which the FWHM starts to narrow is not clearly defined. This is because the FWHM values at 210K and 230K could not be measured as a result of dominant yellow band emission in the PL spectrum.

4.4.3 Integrated Emission Intensity as a Function of Temperature

The total emission intensity was measured by integrating the area under the PL spectrum using the computer program Easyplot. The laser peak, present in some of the PL spectra, was removed from the data prior to integration by deleting the datapoints making up the peak from the spectrum. The integrated emission intensity was then plotted as a function of temperature as shown in Figures 4.16 and 4.17. An Arrhenius plot of the integrated emission intensity is inset in each of the figures.

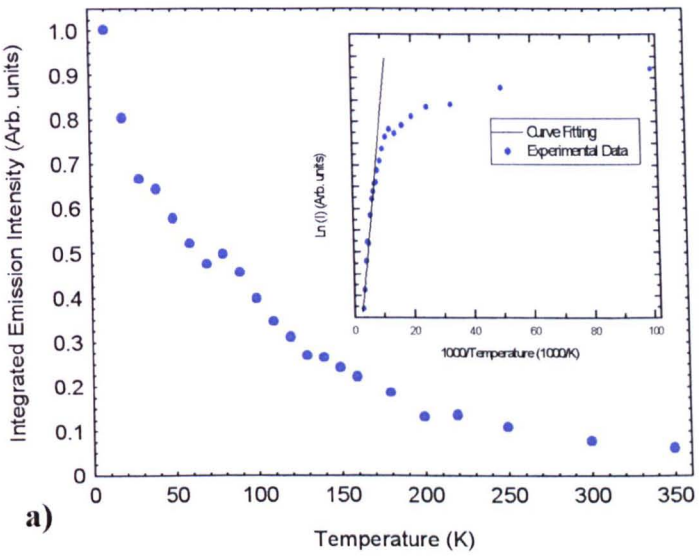

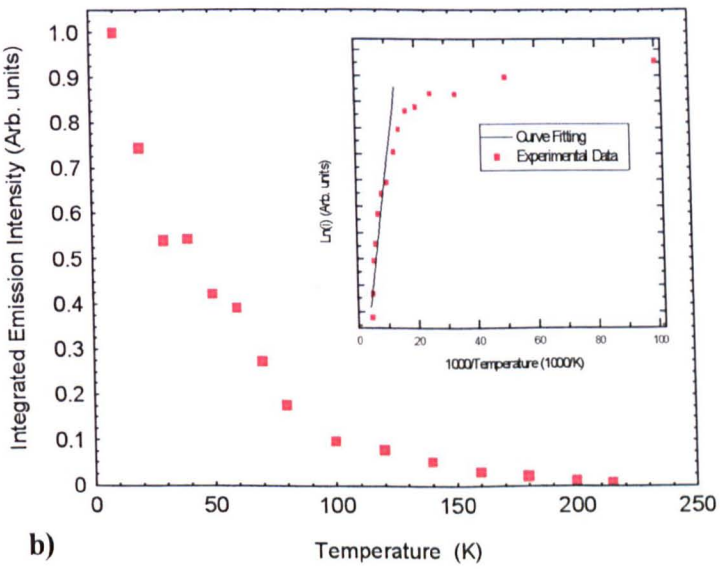

Figure 4.16: Integrated emission intensity as a function of temperature for sample InGaN 131 taken at co-ordinates a) (1.5, 10.0) and b) (2.5, 3.0).

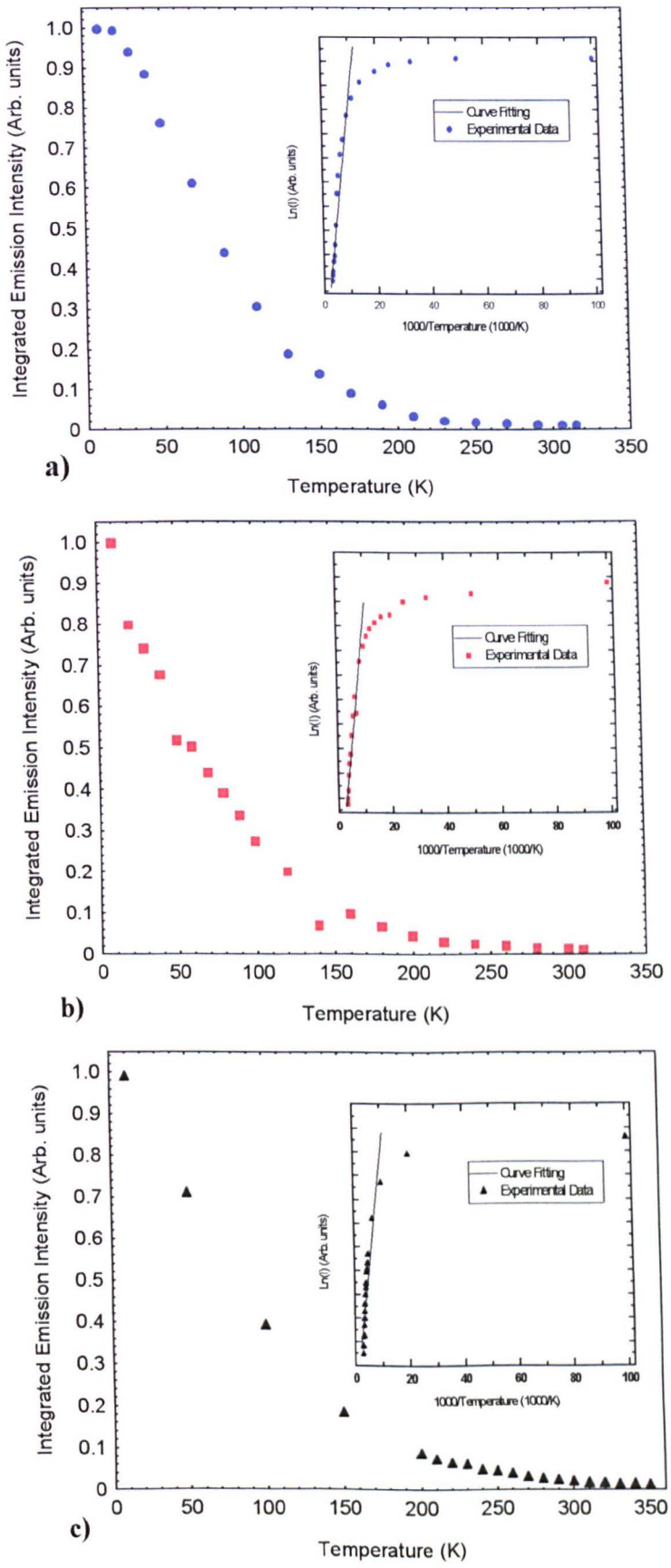

Figure 4.17: Integrated emission intensity as a function of temperature for sample InGaN 85 taken at co-ordinates a) (3.0, 8.5), b) (1.5, 1.0) and c) (2.0, 0.5).

For both samples a fall in the integrated emission intensity with increasing temperature is obtained. This trend can be explained by an increase in the number of non-radiative sites in the material becoming active. Trapping of the carriers by the non-radiative sites will result in a quenching effect on the luminescence intensity. As the quenching effect increases with temperature then the intensity will decrease.

4.5 PL Results Analysis

The PL results are analysed in more detail in the following two sections.

4.5.1 PL Spectra and Mapping Analysis

From the results shown in Figures 4.1 to 4.9 a number of trends were obtained. A broadening of the PL linewidth with decreasing peak emission energy was found. The PL maps exhibited macroscopically inhomogeneous emission from each of the samples investigated and a PL intensity map on one sample showed a reduction in the luminescence intensity with decreasing peak emission energy.

As referred to in Section 4.2 and discussed in detail in Chapter 5, composition measurements taken on some of these samples have shown that a decrease in the peak emission energy scales with the indium nitride content in the material. Considering this relationship, these observed trends may also be described by a change in indium nitride content.

It has previously been reported that linewidth broadening in InGaN occurs due to localisation effects and strain-induced piezoelectric fields [7,8,9,10]. InN-rich QDs formed as a result of phase segregation in InGaN provide efficient centres of localisation. Increasing the indium nitride molar fraction in the material increases the average size of the dots produced and provides a wider distribution of dot sizes. As the emission energy is dependent on the size of the dot, this leads to linewidth broadening in the emission spectrum [7,8]. The scaling factor between indium nitride content and peak emission energy would therefore result in increased linewidth broadening as the peak emission energy decreases. This trend was observed in Figure 4.2.

Strain-induced piezoelectric fields in InGaN become stronger with an increase in the indium nitride content. Any fluctuations in the strain lead to a strongly variable piezoelectric field [9,10]. The resulting QCSE will therefore not only produce a red shift in the emission energy but a broadening of the emission linewidth dependent on the fluctuations in the strain. Less pronounced homogeneous broadening also occurs by decreasing the radiative lifetime of the exciton. The typical exciton recombination energy shift produced by strain-induced piezoelectric fields in InGaN has been shown to be much larger than values obtained from other linewidth broadening factors such as crystal deformation or random alloy fluctuations [9,10].

A change in indium nitride content in the sample can also provide an explanation for the macroscopically inhomogeneous emission shown in the PL maps. The peak emission energy contours observed in Figures 4.3 to 4.7 may be identified with

radial variations of the indium incorporation rate as a result of a temperature gradient across the sample [1].

Moreover, from composition measurement taken on sample InGaN 336 a dependence on the peak emission energy and crystalline quality of the material with a change in the indium nitride content was found; these results will be discussed in Chapter 5. For poorer crystalline quality material it is expected that the emission intensity will be reduced due to a greater number of non-radiative sites. From Figure 4.9 the emission intensity of InGaN 336 was found to lower as the peak emission energy decreases on moving diagonally across the sample.

4.5.2 Temperature Dependence Analysis

Decreasing peak emission energy with increasing temperature can be explained in terms of the effect of temperature on the bandgap energy of a semiconductor [11]. A rise in temperature results in an increase in the number of lattice phonons thermally excited. This in turn reduces the bond energy of the crystal lattice due to electron-phonon coupling. As the bandgap energy reflects the strength of this bond energy, the bandgap energy is reduced with an increase in temperature. The temperature dependence of the bandgap energy may be described the equation;

$$E_g(T) = E_g(0) - S\langle\hbar\omega\rangle\left[\coth\left(\frac{\langle\hbar\omega\rangle}{2kT}\right) - 1\right] \qquad \textbf{Equation 4.3}$$

where $E_g(0)$ is the bandgap energy at 0K, S is a dimensionless parameter that represents a measure of the strength of the electron-phonon coupling, $\langle \hbar\omega \rangle$ is the average phonon energy and k the Boltzmann constant [11].

Thermal expansion effects on the lattice constant may also produce a change in the bandgap energy. However, over the temperature range covered in these measurements, the contributions of thermal expansion effects are relatively small in comparison to the effects of electron-phonon interactions [12].

A fitting of equation 4.3 to the experimental datapoints of InGaN 131 is shown in Figure 4.12. The best fit values of the parameters $E_g(0)$, S and $\langle \hbar\omega \rangle$ are given in Table 4.1. From Figure 4.12a) the curve fitting correlates well with the experimental datapoints and in Figure 4.12b) although the fit is not as good, it still follows the general trend of the experimental results. The decrease in the peak emission energy with increasing temperature for InGaN 131 can therefore be attributed to the effects of temperature on the bandgap of the material.

For sample InGaN 85, due to the 'S'-shape temperature dependence of the peak emission energy it was found that equation 4.3 could only be applied over the temperature range $10K \leq T \leq 170K$. Over this range the curve was found to fit fairly well with the experimental datapoints, although the number of datapoints present in Figure 4.13c) is not really sufficient to provide a good comparison. Between $10K \leq T \leq 170K$ the temperature dependence of the peak emission energy may therefore be

described by the relationship between bandgap and temperature. At T ≥170K this explanation is clearly no longer sufficient to describe the results.

'S'-shape temperature dependence in InGaN was first observed by Cho et al. [6]. From the results of integrated PL intensity and carrier lifetime measurements plotted as a function of temperature, the authors reported that InGaN emission was strongly affected by a change in carrier recombination dynamics with increasing temperature. The emission behaviour was attributed to the effects of inhomogeneity and carrier localisation in InGaN [6]. The red-blue-red shift in the peak emission energy could be thought of as split into three parts. The initial redshift at low temperatures occurs as the radiative recombination processes are dominant and the lifetime of the carriers is long enough to allow them to relax down to lower energy tail states before recombination. At higher temperatures the blueshift occurs, as other non-radiative processes become dominant and the carrier lifetime decreases so that the carriers recombine before reaching lower energy states. Finally, at sufficiently high temperatures the second redshift occurs, as the fall in the carrier lifetime decreases the carriers will be less affected and the blueshift gets smaller. Temperature induced bandgap shrinkage in the material therefore results in an overall redshift in the peak emission energy [6].

Expanding this idea further, the 'S'-shape behaviour can also be described by the localisation effect of InN-rich QDs in InGaN [13,14]. Analysis of the PL results presented in this Chapter and composition measurements taken on the sample, discussed in Chapter 5, indicate the presence of such InN-rich QDs. Furthermore,

the same 'S'-shape temperature dependence relationship was obtained when taken using two different exciting laser lines. This result suggests that the cause of the 'S'-shape is not dependent on excitation energy and is therefore unlikely to be related to any random alloy fluctuations in the sample.

At low temperatures, localisation of the carriers in the InN-rich QDs occurs. The initial redshift in peak emission energy with increasing temperature may be due to the relationship between bandgap energy and temperature, as outlined previously and shown from the curve fittings to the experimental datapoints in Figure 4.13. At sufficiently high temperatures the carriers may then have enough energy that they can leave the InN-rich QD and begin to recombine in regions which are not InN-rich. This produces the blueshift in the peak emission energy. As the temperature continues to rise, some of the carriers may become trapped in other InN-rich QDs and as the effects of temperature on the bandgap starts to influence the PL spectrum again, the resultant peak emission energy redshifts. A certain amount of recombination will occur in both the InN-rich and non InN-rich regions at any given temperature, hence the emission spectrum from the sample can be thought of as made up of two emission bands, one related to emission from the InN-rich regions and one from the non InN-rich regions. The type of emission favoured at a given temperature determines which band is stronger and will therefore dominate the PL spectrum. The red-blue-red shift can then be thought of as a shift between the two emission bands with the changing temperature.

Approximate values for the localisation effects in the material can be obtained from the difference in peak emission energy between the start and end energies of the blueshift. These were found to be 47meV, 32meV and 21meV from the results shown in Figure 4.13 a), b) and c) respectively.

The 'S'-shape temperature dependence from sample InGaN 85 but not from sample InGaN 131 can be explained by the difference in the indium nitride content of the samples. From the PL map of InGaN 131, a much higher peak emission energy is obtained than at any point from the PL map of InGaN 85. Applying the scaling factor in Chapter 5 between peak emission energy and indium nitride fraction, sample InGaN 131 will have a lower indium content than InGaN 85. Consequently, the number of InN-rich QDs in InGaN 131 will be less and the influence of localisation effects on the PL spectrum smaller.

Comparing the results in Table 4.1 for $\langle \hbar\omega \rangle$ there is clearly a difference in the average phonon energies obtained from the two samples. This further indicates a difference in the emission processes of the samples. During the fitting to equation 4.3, $\langle \hbar\omega \rangle$ was set as a free parameter to include both optical and acoustic phonon energies. Typical LO phonon energies from InN ~75meV and GaN ~92meV [15,16]. The fitting values obtained are smaller than either of these values and the results from InGaN 85 are approximately an order of magnitude less than those from InGaN 131.

The FWHM broadening effect with increasing temperature can be described by the equation;

$$\Gamma(T) = \Gamma(0) + \gamma\left[\coth\left(\frac{\langle\hbar\omega\rangle}{2kT}\right) - 1\right] \qquad \textbf{Equation 4.4}$$

where $\Gamma(0)$ is the FWHM at 0K, γ is a dimensionless parameter, $\langle\hbar\omega\rangle$ is the average phonon energy and k the Boltzmann constant. This equation is just the reciprocal of equation 4.3 written in the form of linewidth rather than energy.

Temperature dependent broadening of the FWHM can be explained by a greater number of lattice phonons present at higher temperatures. This increases the probability of interactions between phonons and excitons resulting in a broadening of the PL spectrum. The linewidth of the spectrum increases as the photon energies are redistributed by ± the phonon energies.

In Figure 4.14a) a good correlation between the experimental datapoints and the curve fitting of equation 4.4 is observed for InGaN 131. In Figure 4.14b) the fitting also follows the general trend of the datapoints. The increase in the FWHM over the temperature range investigated was found to be ~46meV and ~34meV for Figure 4.14 a) and b) respectively. These results are comparable with the localisation energies of ~ 30meV and 19meV calculated at the maximum temperature for each set of measurements.

From InGaN 85, a steep rise in the FWHM is obtained up to temperatures of 190K as shown in Figure 4.15a) and 240K in b) and c). At temperatures above these values the FWHM decreases sharply. The same processes outlined in the explanation of the 'S'-shape temperature dependence can describe these effects. Equation 4.4 fits fairly well to the experimental datapoints in Figure 4.15 over the temperature range where the FWHM broadens. The overall increment in the FWHM between 10K and these temperatures is ~230meV, 236meV and 216meV, almost an order of magnitude larger than the total FWHM broadening from sample InGaN 131. The large FWHM broadening effect observed reinforces the idea that there may be two emission bands present in the PL spectrum. The subsequent sharp drop in the FWHM at higher temperatures would then occur as one band decreases at a much faster rate than the other. Comparison with the results in Figure 4.13 suggests that it is the higher energy emission band that decreases more rapidly producing the blueshift in the peak emission energy and the narrowing of the FWHM. However, there is a difference of ~40K between the temperatures at which the blueshift begins and the FWHM starts to narrow. This is tentatively ascribed to the effects of temperature induced phonon broadening merging the transition between broadening and narrowing of the FWHM value as the peak emission energy shifts from red to blue.

The phonon energies from the fitting of equation 4.4, shown in Table 4.1, are smaller in InGaN 131 than from InGaN 85, again indicating that there is a difference in the emission processes of these two samples. Unfortunately, none of the values for the fitting parameters from equations 4.3 and 4.4 can be directly compared with those obtained by Cho et al. as a Varshni equation was used by the authors to fit to

the datapoints [17]. The equation used in this thesis has been shown to have a better numerical fit to the temperature dependence of a semiconductor bandgap for a range of different samples than that of the Varshni equation [11].

The temperature dependence of integrated intensity is most often described by the equation;

$$I(T) = \frac{I_o}{1 + \alpha \exp\left(\frac{-E_a}{kT}\right)} \qquad \textbf{Equation 4.5}$$

where α is the process rate parameter, E_a is the activation energy of thermal quenching and k the Boltzmann constant [18]. The activation energy is usually determined by measuring the slope of a straight line at high temperature in an Arrhenius plot of Ln(I) with the inverse of temperature. This fitting was applied to the results shown in Figures 4.16 and 4.17 for T ≥90K. The activation energies determined are shown in Table 4.1. E_a was found to lie between 30 and 60meV, in agreement with typical values of E_a reported in the literature [6,13]. E_a from sample InGaN 85 is notably higher than that from InGaN 131. The increased activation energy indicates deeper localisation occurring in the sample, this may be due to the increased localisation effects of InN-rich QDs.

Variations and small discrepancies in the PL spectra from the observed trends as discussed may be produced as a result of fluctuations in the intensity of the argon

ion laser used or from small shifts in the position of the sample measured due to expansion effects of the cryostat cold-head with the increasing temperature.

Sample (x, y co-ordinate)	$E_g(0)$ (eV)	S	$\langle\hbar\omega\rangle$ (meV) Equation 4.3	$\Gamma(0)$ (meV)	γ	$\langle\hbar\omega\rangle$ (meV) Equation 4.4	E_a (meV)
InGaN 131 (1.5, 10.0)	3.30	3.17	51	76	0.03	29.5	29(2)
InGaN 131 (2.5, 3.0)	3.41	3.62	45	40	0.01	6	41(6)
InGaN 85 (3.0, 8.5)	2.73	3.38	6	124	4.48	61	45(4)
InGaN 85 (1.5, 1.0)	2.58	3.04	9	115	1.03	48	46.5(5)
InGaN 85 (2.0, 0.5)	2.58	1.84	5	133	0.52	37	46(5)

Table 4.1: Best fit values for the parameters in the fitting equations.

4.6 Summary

In this chapter, photoluminescence spectra from a number of different InGaN epilayer samples were presented and discussed. From the results an increase in the linewidth of the emission spectrum with a decrease in the peak emission energy was determined. PL maps on each sample show macroscopically inhomogeneous emission. The PL maps also revealed a unique piece of InGaN that emits in the red and infra-red. An intensity map of this sample exhibited a reduction in the luminescence intensity with decreasing peak emission energy. These results may all be described by a change in the indium nitride content in the material.

From temperature dependent PL measurements taken on two of the InGaN samples, different relationships in the peak emission energy and FWHM with temperature were obtained. In one sample, a decrease in the peak emission energy with increasing temperature was found and shown to be produced as a result of the reduction in the bandgap energy of the material with increasing temperature. FWHM broadening with increasing temperature from this sample may be due to phonon broadening effects. From the other InGaN sample an 'S'-shape temperature dependence of the peak emission energy was observed. This can be described by localisation effects of InN-rich QDs formed in InGaN. These effects may also explain the variations in the FWHM with increasing temperature. The integrated emission intensity from both samples was shown to decrease with increasing temperature and the activation energies, from an Arrhenius plot of the integrated intensity, found to be consistent with those published in the literature.

4.7 References

[1] Wim Van der Stricht, PhD Thesis, University of Ghent, *Development of group III nitride technology for the realisation of light emitting diodes*, unpublished (1998-1999).

[2] B. Gil and M. Leroux, *Properties of Indium Nitride*, EMIS Datareview 23 (1999).

[3] D. J. Oostra, Philips J. Res. **47**, 315 (1993).

[4] T. Ogino and M. Aoki, Jpn. J. Appl. Phys. **19**, 2395 (1980).

[5] E. R. Glaser, T. A. Kennedy, K. Doverspike, I. B. Rowland, D. K. Gaskill, J. A. Freitas, Jr., M. Asif Khan, D. T. Olson, J. N. Kuznia and D. K. Wickenden, Phys. Rev. B **51**, 13326 (1995).

[6] Y.-H. Cho, G. H. Gainer, A. J. Fischer, J. J. Song, S. Keller, U. K. Mishra and S. P. DenBaars, Appl. Phys. Lett. **73**, 1370 (1998).

[7] R. W. Martin, P. G. Middleton, K. P. O'Donnell and W. Van der Stricht, Appl. Phys. Lett. **74**, 263 (1999).

[8] K. P. O'Donnell, R. W. Martin and P. G. Middleton, Phys. Rev. Lett. **82**, 237 (1999).

[9] P. G. Middleton, K. P. O'Donnell, T. Breitkopf, H. Kalt, W. Van der Stricht, I. Moerman and P. Demeester, Mat. Sci. Eng. B **50**, 285 (1997).

[10] K. P. O'Donnell, T. Breitkopf, H. Kalt, W. Van der Stricht, I. Moerman, P. Demeester and P. G. Middleton, Appl. Phys. Lett. **70**, 1843 (1997).

[11] K. P. O'Donnell and X. Chen, Appl. Phys. Lett. **58**, 2924 (1991).

[12] A. T. Collins, S. C. Lawson, G. Davies and M. Kanda, Phys. Rev. Lett. **65**, 891 (1990).

[13] H. P. D. Schenk, M. Leroux and P. de Mierry, J. Appl. Phys. **88**, 1525 (2000).

[14] M. G. Cheong, H. S. Yoon, R. J. Choi, C. S. Kim, S. W. Yu, C.-H. Hong, E.-K. Suh and H. J. Lee, J. Appl. Phys. **90**, 5642 (2001).

[15] H. C. Yang, P. F. Kuo, T. Y. Lin, Y. F. Chen, K. H. Chen, L. C. Chen and J.-I. Chyi, Appl. Phys. Lett. **76**, 3712 (2000).

[16] D. Kovalev, B. Averboukh, D. Volm, B. K. Meyer, H. Amano and I. Akasaki, Phys. Rev. B **54**, 2518 (1996).

[17] Y. P. Varshni, Physica, **34**, 149 (1967).

[18] D. S. Jiang, H. Jung and K. Ploog, J. Appl. Phys. **64(3)**, 1371 (1988).

CHAPTER 5: COMPOSITION ANALYSIS AND PHOTOLUMINESCENCE OF InGaN EPILAYERS

5.1 Introduction

An experimental technique that provides an accurate measure of composition is necessary if we wish to ascertain the effect of indium nitride content on the optical characteristics of InGaN epilayers. In this chapter, compositional measurements, taken using three different experimental techniques, are related to the PL peak emission energy for a range of samples. The techniques used are Rutherford backscattering spectrometry (RBS), electron probe microanalysis (EPMA) and extended X-ray absorption fine structure (EXAFS). A description of each experimental technique is given in Chapter 3, Section 3.2 and details of the investigated samples in Appendix A, Section A.1.1.

The results of this study are compared with composition measurements on InGaN taken from the literature.

5.2 RBS Results

RBS measurements were carried out on samples InGaN 331 and InGaN 336A. RBS is suitable for the purpose of measuring the composition of InGaN epilayers as it gives direct information independent of the effects of strain in the material.

A typical RBS spectrum from sample InGaN 331, normalised at 1000, is shown in Figure 5.1. The backscattering yield of He^+ ions as a function of particle energy in both the random and aligned directions is plotted on the diagram.

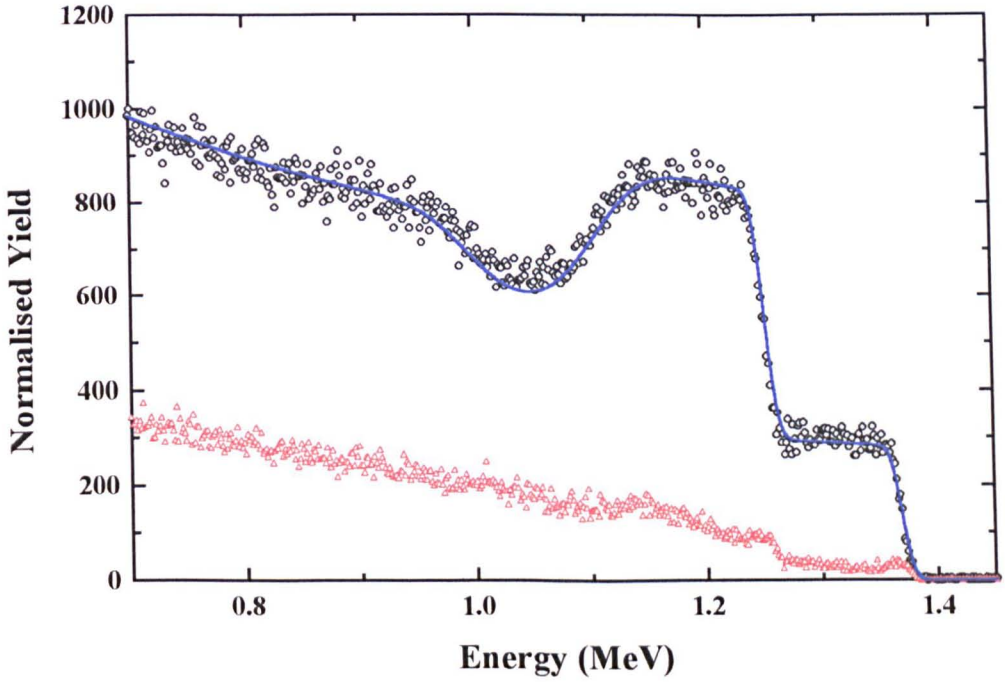

Figure 5.1: RBS spectra of sample InGaN 331. Random (o), c-axis aligned (Δ) and simulated (solid line) RBS spectra are shown.

The indium nitride concentration and InGaN layer thickness were determined by fitting a computer model simulation of the backscattering spectrum of an InGaN alloy to the random RBS spectrum. The crystalline quality, χ_{min}, was calculated as the ratio of the backscattering yield along the aligned direction to that from the random direction, at the near surface region, ~1.36MeV. Lower values of χ_{min} indicate better crystallinity.

Both InGaN samples exhibit a concentration gradient across the sample surface; this allows several different composition measurements to be made from the one sample.

PL spectroscopy measurements were carried out prior to RBS analysis as it was found that the RBS high energy probe beam lowers the luminescent efficiency over the region of the sample addressed. In Figure 5.2, the low temperature PL peak emission energy is plotted against the indium nitride fraction from the RBS measurements taken from equivalent points on the sample. The data is supplemented with results from RBS measurements on indium poor samples provided by McCluskey et al. [1].

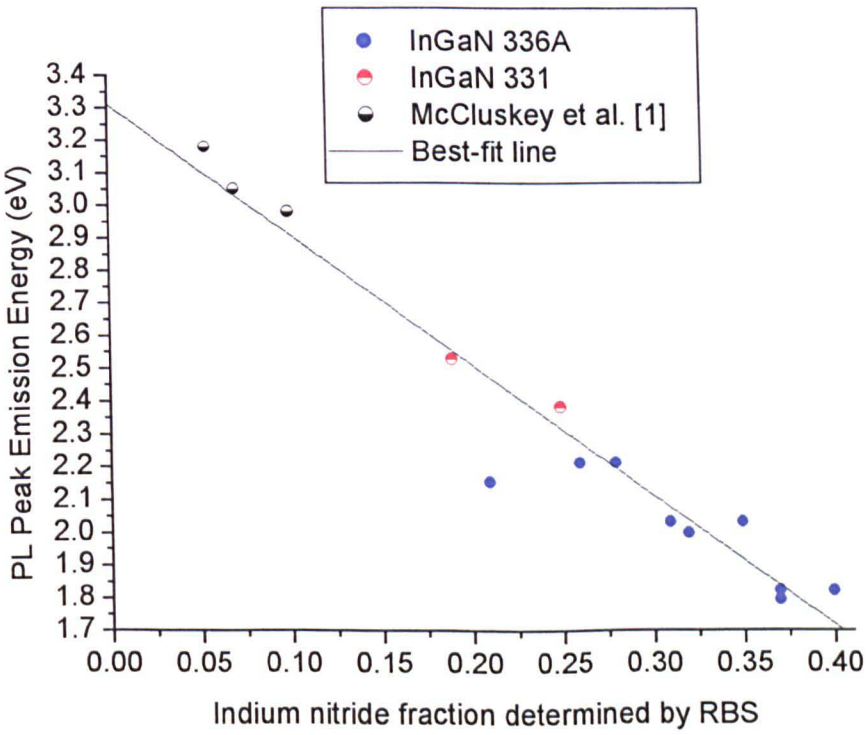

Figure 5.2: PL peak emission energy against indium nitride fraction determined by RBS.

Figure 5.2 shows a decrease in the PL peak emission energy with increasing indium nitride content. A linear relationship between PL peak emission energy, E_p(eV), and indium nitride content, x, is obtained over the composition range $0.05 \leq x \leq 0.40$. The equation of best-fit line (with the error estimates in parenthesis) is given by;

$$E_p = 3.31(8) - 3.98(27)x \qquad \textbf{Equation 5.1}$$

For sample InGaN 336A there is also a corresponding increase in the value of χ_{min}, from 53% to 70% with the increase in indium nitride fraction from 0.28 to 0.40. Sample InGaN 331 has smaller values for χ_{min}, typically ~20%. Both samples therefore have rather poor crystallinity. The thickness of the InGaN epilayers was estimated to be ~270nm for InGaN 331 and ~230nm for InGaN 336A from the RBS fitting.

It was also noted that the nitrogen fraction in InGaN 336A increases from 1.4 to 1.9 as x increases from 0.28 to 0.40. On the other hand, sample InGaN 331 has a nitrogen content of unity as expected for a stoichiometric layer. The nitrogen fraction values of InGaN 336A show that high indium nitride samples may be non-stoichiometric.

5.3 EPMA Results

EPMA was used to carry out composition analysis on sample InGaN 85. EPMA is an ideal technique for use on InGaN as it is non-destructive, has high spatial resolution and the results are independent of any strain effects acting on the material.

In Figure 5.3, the low temperature PL peak emission energy is plotted against the indium nitride fraction determined by EPMA from the same position on the sample.

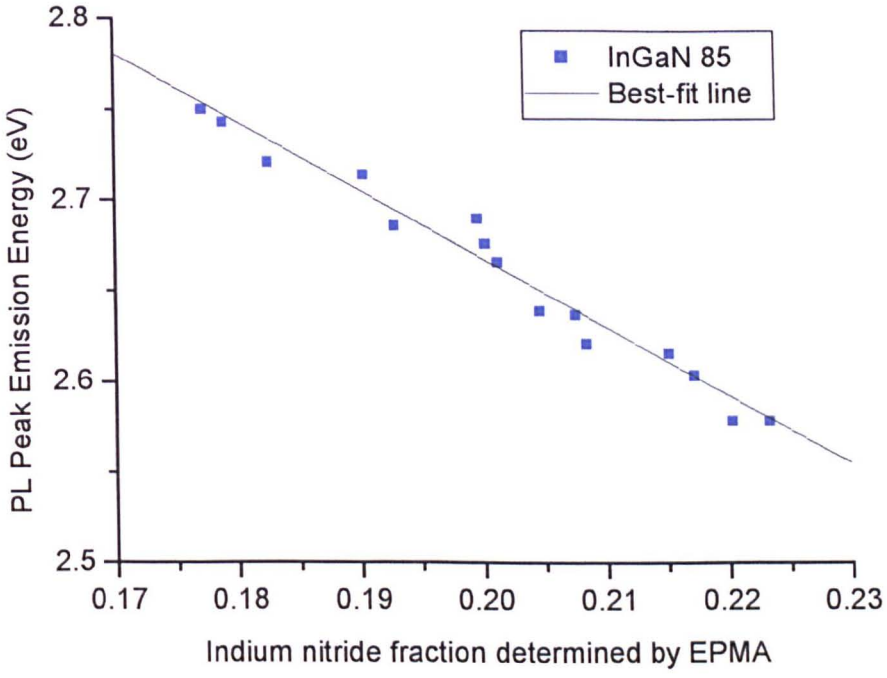

Figure 5.3: PL peak emission energy against indium nitride fraction determined by EPMA.

Figure 5.3 shows a linear dependence of the PL peak emission energy on the indium nitride fraction over the composition range $0.17 \leq x \leq 0.23$. The equation of best-fit plotted through the data is;

$$E_p = 3.42(4) - 3.76(19)x \qquad \textbf{Equation 5.2}$$

The EPMA measurements were taken at 10kV and the composition values calculated using the CAMECA 'Layers' programme in the EPMA, which corrects for the InGaN/GaN bilayer thicknesses in the sample. However, in order to check the consistency of the composition results, measurements and analytical simulations were carried out at two accelerating voltages, 5kV and 10kV. The composition

values for each voltage were found to be comparable to within less than 1% of the cation fraction.

Images from the CCD camera installed in the EMPA showed the surface of the sample to be very uneven and granular in appearance with a number of hexagonal structures present. Cathodoluminescence observed during the EPMA measurements varied from blue to green/blue on moving around the sample.

5.4 EXAFS Results

Extended X-ray absorption fine structure (EXAFS) was used to determine the composition of samples InGaN 85, 336A and 336X. EXAFS is a non-destructive analysis technique from which information on the composition and local structure of the material can be extracted. Typical In-edge EXAFS from an InGaN epilayer sample is shown in Figure 5.4.

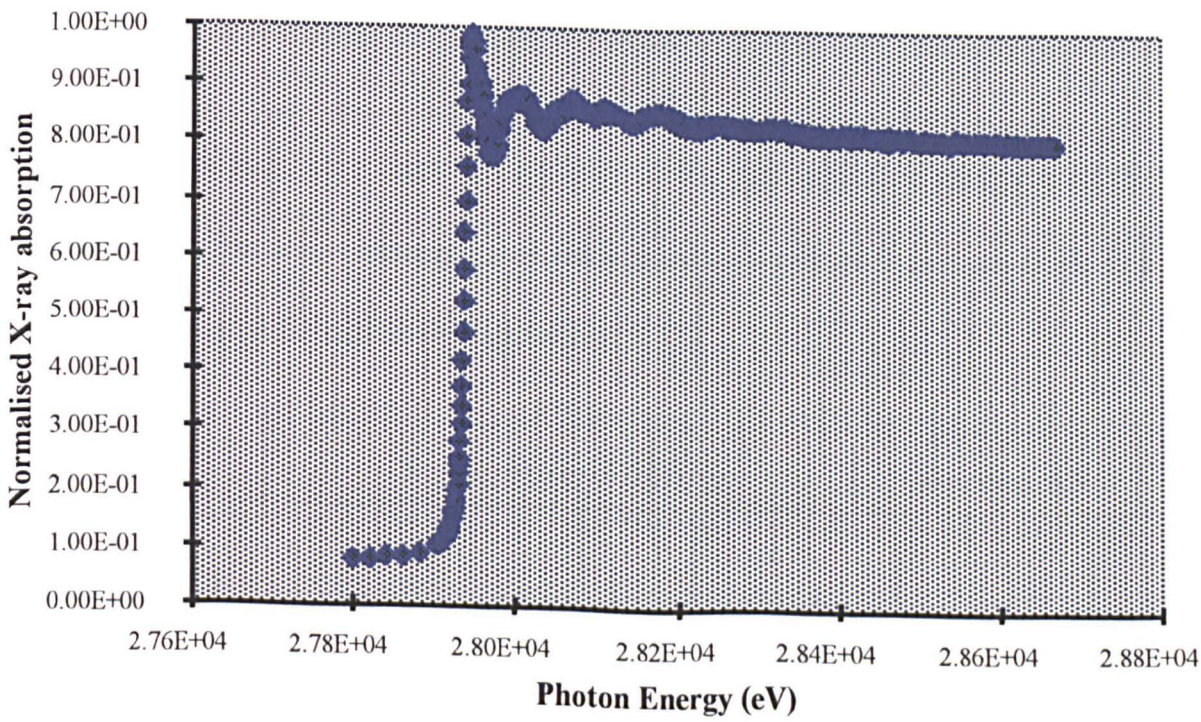

Figure 5.4: In-edge EXAFS from sample InGaN 336A.

In Figure 5.4, the low temperature PL peak emission energy is plotted against the indium nitride composition values derived from EXAFS taken from the equivalent position on the sample.

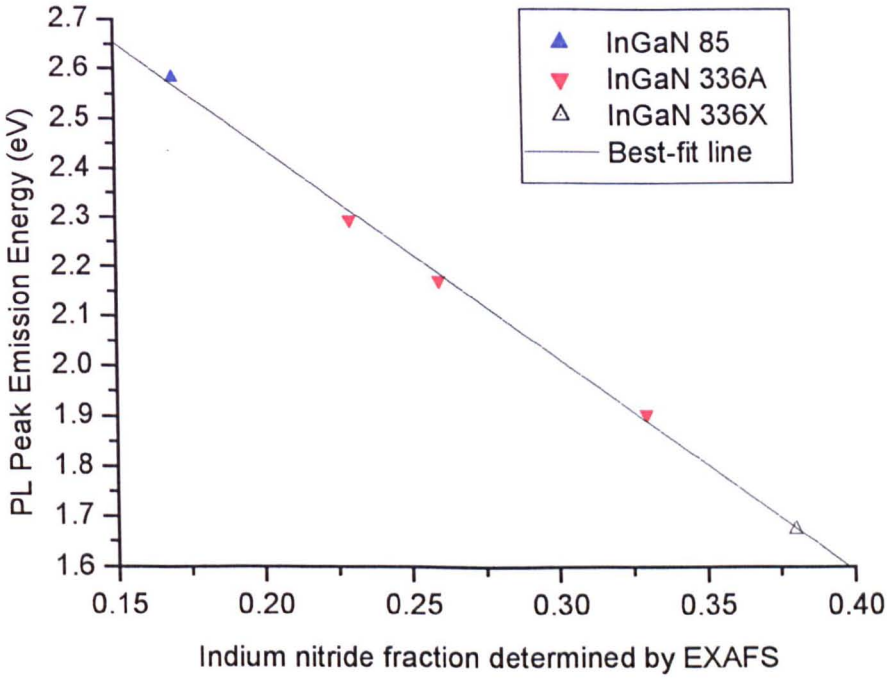

Figure 5.5: PL peak emission energy against indium nitride fraction determined by EXAFS.

As shown in Figure 5.5 a linear dependence of PL peak emission energy with the indium nitride fraction is observed over the concentration range $0.17 \leq x \leq 0.38$. The best-fit line plotted through the datapoints is;

$$E_p = 3.29(3) - 4.24(11)x \qquad \textbf{Equation 5.3}$$

The local structure parameters also obtained from EXAFS measurements are presented and discussed in Chapter 7.

5.5 Summary of Composition Measurements

In Figures 5.2, 5.3 and 5.5, a linear relationship between PL peak emission energy and indium nitride content was observed from the results of each composition analysis technique. In Figure 5.6, all of these results are plotted together.

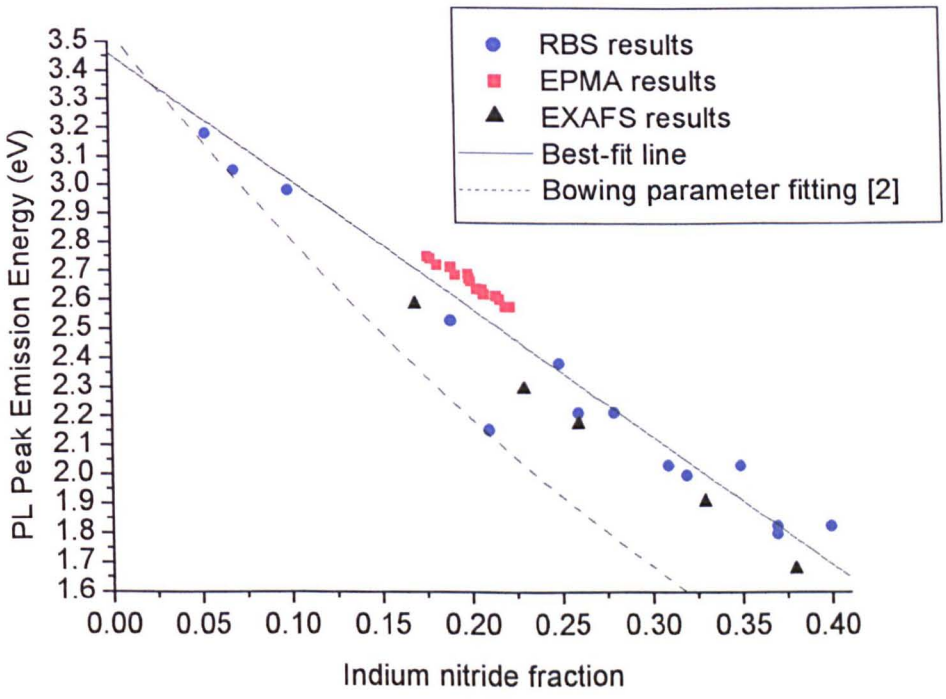

Figure 5.6: PL peak emission energy against indium nitride fraction determined by RBS, EPMA and EXAFS.

As shown in Figure 5.6, the results obtained by different techniques were found to agree fairly well with one another and a linear relationship between PL peak emission energy and indium nitride content may be determined between $0.05 \leq x \leq 0.40$. The best-fit line drawn through the combined datapoints is given by the equation:

$$E_p = 3.46(6) - 4.42(24)x \qquad \textbf{Equation 5.4}$$

The linear relationship between PL peak emission energy and indium nitride content was therefore shown to hold for a number of epilayer samples, using three different analysis techniques based upon entirely different physical principles. There is no evidence of any band bowing from these results, as seen in Figure 5.6, with comparison to the conventional bowing parameter curve fitting found in the literature;

$$E_g(InGaN) = xE_g(InN)+(1-x)E_g(GaN)-bx(1-x) \qquad \textbf{Equation 5.5}$$

where E_g(eV) is the bandgap of the relaxed unstrained alloy with composition x, calculated using a bowing parameter value, b~3.8 [2]. The bowing parameter curve, as shown in Figure 5.6, was calculated for emission energy using the relationship determined between bandgap energy and emission energy [3];

$$E_p = 1.45(3)E_g - 1.54(8). \qquad \textbf{Equation 5.6}$$

Extrapolating the best-fit line through the datapoints out to zero indium content, the line cuts the energy axis at 3.46(6)eV, close to the low temperature bandgap of GaN ~3.5eV, as expected. It was also noted that the EPMA datapoints sit slightly higher on the graph than the RBS or EXAFS results.

5.6 Discussion of Composition Measurements

The linear relationship between PL peak emission energy and indium nitride content for a range of InGaN samples may be explained by exciton localisation in InN-rich QDs formed due to phase segregation effects in InGaN. As described in Chapter 4,

Section 4.5.1, an increase in the indium nitride molar fraction would be expected to increase the diameter of the QDs, this would produce a lowering of the confinement energy and result in a redshift in the emission energy. This was found to be the case as shown in Figure 5.6. In addition, strong luminescence obtained from samples InGaN 331 and InGaN 336A, which have poor crystalline quality, is further evidence for localisation effects in these materials.

The RBS and EPMA measurements show no direct evidence of these InN-rich QDs. However, the area sampled in the RBS measurement is on the mm-scale and in the EPMA measurement on the μm-scale, both of which are considerably larger than the size of a typical InN-rich QD, estimated to be of the order ~1nm [4].

5.7 Comparison with Composition Measurements in the Literature

In Figure 5.7, the experimental results are compared with those taken from the literature. A best-fit line of the datapoints is shown for each set of results. Table 5.1 compares the intercept and slope of the assumed linear fit to the data. The best-fit line for the RBS, EPMA and EXAFS results are included in the table individually as well as in their combined form given by equation 5.4. The range of the indium nitride content values and the temperature at which the PL measurements were carried out are also given in Table 5.1.

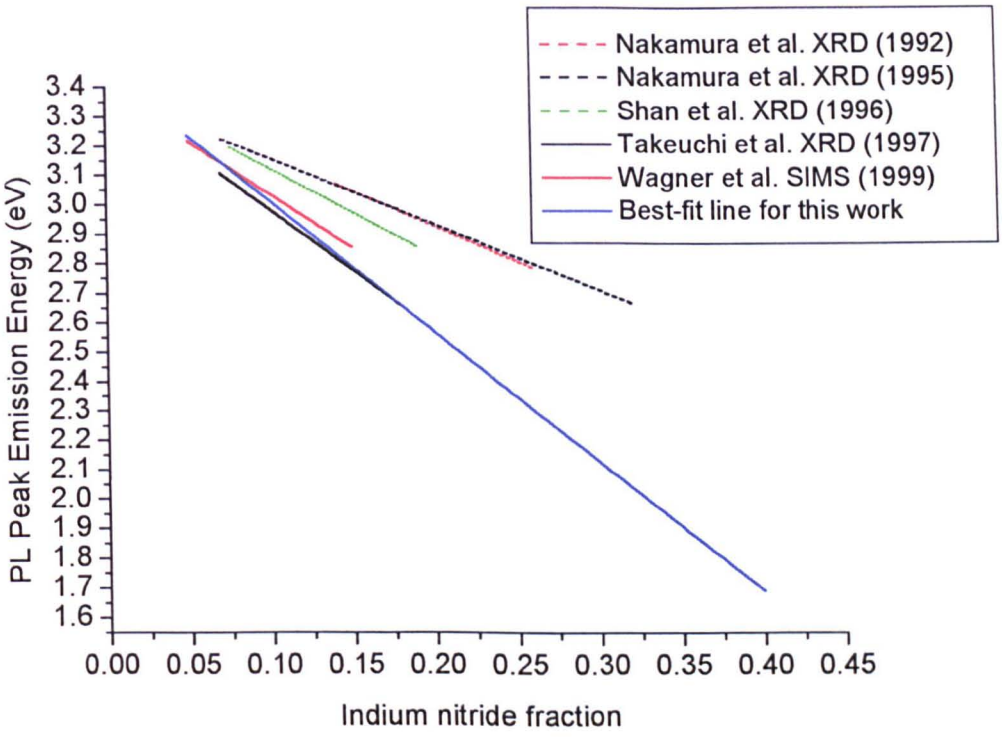

Figure 5.7: Comparison of this work with results taken from the literature (see text for details).

Author Date (Technique)	PL Temperature (K)	Indium Nitride Content	Intercept (eV)	Slope (eV)
Nakamura et al.[5] 1992 (XRD)	Room Temperature	0.14 – 0.26	3.41	-2.36
Nakamura et al.[6] 1995 (XRD)	Room Temperature	0.07 – 0.33	3.38	-2.21
Shan et al.[7] 1996 (XRD)	10K	0.075 – 0.19	3.42	-2.93
Takeuchi et al.[8] 1997 (XRD)	Room Temperature	0.075 – 0.19	3.39	-4.04

Wagner et al.[9] 1999 (SIMS)	Room Temperature	0.05 – 0.15	3.40	-3.59
This work (RBS, EPMA and EXAFS)	10K	0.05 – 0.40	3.46	-4.42
This work (RBS)	10K	0.05 – 0.40	3.31	-3.98
This work (EPMA)	10K	0.17 – 0.23	3.42	-3.76
This work (EXAFS)	10K	0.17 – 0.38	3.29	-4.24

Table 5.1: Parameters of the linear fits obtained for results collected from the literature and this work.

From Figure 5.7 and Table 5.1, there is a substantial measure of agreement between the fits obtained in this work and those in references [8,9]. However, these results appear to disagree with the earlier work published in references [5,6,7]. On comparison, the earlier composition measurements overestimate the indium nitride fraction for a given emission energy by as much as a factor of 2. XRD measures structural parameters in the material directly but is an indirect technique with which to measure composition. It is therefore essential that a sample's state of strain should be taken into account when determining its composition using XRD [10]. A correction for strain was applied to the results in reference [8] but was not included in the analysis of the earlier results nor in many of the results up to ~1998/99 found in the literature. Composition measurements taken by RBS, EPMA, EXAFS and SIMS are independent of the effects of sample strain.

5.8 Summary

In this chapter, composition measurements of MOCVD grown InGaN epilayer samples using RBS, EPMA and EXAFS were presented and related to the PL peak emission energy taken from the equivalent position on the sample. A linear relationship between PL peak emission energy and indium nitride fraction was obtained for each set of results. The results from different analysis techniques were found to agree fairly well and a best-fit line over the range $0.05 \leq x \leq 0.40$ determined. There was no evidence of band bowing from the results. On comparison with composition measurements taken from the literature, the results agree well with composition values obtained using SIMS and XRD measurements, when the latter have been corrected for the effects of strain in the material. Early XRD results, not corrected for the effects of strain, were shown to overestimate the indium nitride fraction by as much as a factor of 2.

5.9 References

[1] M. D. McCluskey, C. G. Van de Walle, C. P. Master. L. T. Romano and N. M. Johnson, Appl. Phys. Lett. **72**, 2725 (1998); PL measurements obtained from M. D. McCluskey, private communication to R. W. Martin (1999).

[2] C. G. Van de Walle, M. D. McCluskey, C. P. Master, L. T. Romano and N. M. Johnson, Mat. Sci. Eng B **59**, 274 (1999).

[3] K. P. O'Donnell, R. W. Martin, C. Trager-Cowan, M. E. White, K. Esona, C. Deatcher, P. G. Middleton, K. Jacobs, W. Van der Stricht, C. Merlet, B. Gil, A. Vantomme and J. F. W. Mosselmans, Mat. Sci. Eng. B **82**, 194 (2001).

[4] K. P. O'Donnell, R. W. Martin and P. G. Middleton, Phys. Rev. Lett. **82**, 237 (1999).

[5] S. Nakamura and T. Mukai, Jpn. J. Appl. Phys. **31**, L1457 (1992).

[6] S. Nakamura, J. Vac. Sci. Technol. A **13(3)**, 705 (1995).

[7] W. Shan, B. D. Little, J. J. Song, F. C. Feng, M. Schurman and R. A. Stall, Appl. Phys. Lett. **69**, 3315 (1996).

[8] T. Takeuchi, H. Takeuchi, S. Sota, H. Sakai, H. Amano and I. Akasaki, Jpn. J. Appl. Phys. **36**, L177 (1997).

[9] J. Wagner, A. Ramakrishnan, D. Behr, M. Maier, N. Herres, M. Kunzer, H. Obloh and K.-H. Bachem, MRS Internet J. Nitride Semicond. Res. **4S1**, G2.8 (1999).

[10] S. Pereira, M. R. Correia, E. Pereira, C. Trager-Cowan, F. Sweeney, P. R. Edwards, K. P. O'Donnell, E. Alves, A. D. Sequeira and N. Franco, Mater. Res. Soc. Symp. Proc. **639**, G3.52 (2000).

CHAPTER 6: CONFOCAL MICROSCOPY AND SPECTROSCOPY OF InGaN EPILAYERS, QWS AND QBS

6.1 Introduction

Confocal microscopy (CM) was used to survey fluorescent InGaN epilayer, QW and QB samples. Fluorescence and reflectance images of the sample surface were obtained at temperatures ranging from room temperature down to ~77K. A crude form of fluorescence spectroscopy was carried out using a series of bandpass filters in the fluorescence channel of the CM. However, later modifications to the CM set-up allowed the photoluminescence (PL) spectrum to be taken directly from a selected area on the sample with simultaneous reflectance imaging.

The results were analysed for trends between luminescence and surface morphology. This may provide an indication as to the origin of InGaN luminescence.

A description of the confocal microscope set-up is given in Chapter 3, Section 3.1.5 and details of the investigated samples in Appendix A.

6.2 Confocal Microscopy Images

Low temperature CM images of several InGaN samples are shown in Figures 6.1 to 6.4. The images have been enhanced by computer generated false colours using the image processing software package PaintShopPro5. To distinguish fluorescence and reflectance images, the fluorescence image is coloured differently to the reflectance image, generally red or orange as opposed to green or blue. On forming a composite

of the two images, regions of dominant fluorescence and reflectance can still be differentiated, as shown in Figures 6.1c), 6.2c) and 6.4. Areas in which fluorescence and reflectance are equally prominent show as a 'mix' of the two colours.

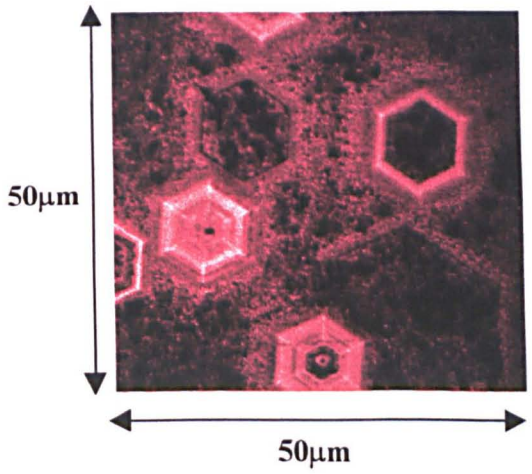

a) Fluorescence image

b) Reflectance image

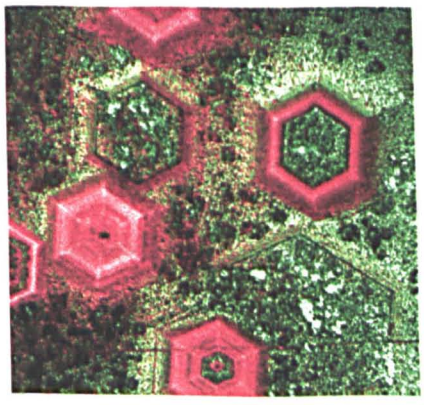

c) Composite image = a) + b)

Figure 6.1: Combining fluorescence and reflectance confocal images from epilayer sample InGaN 331.

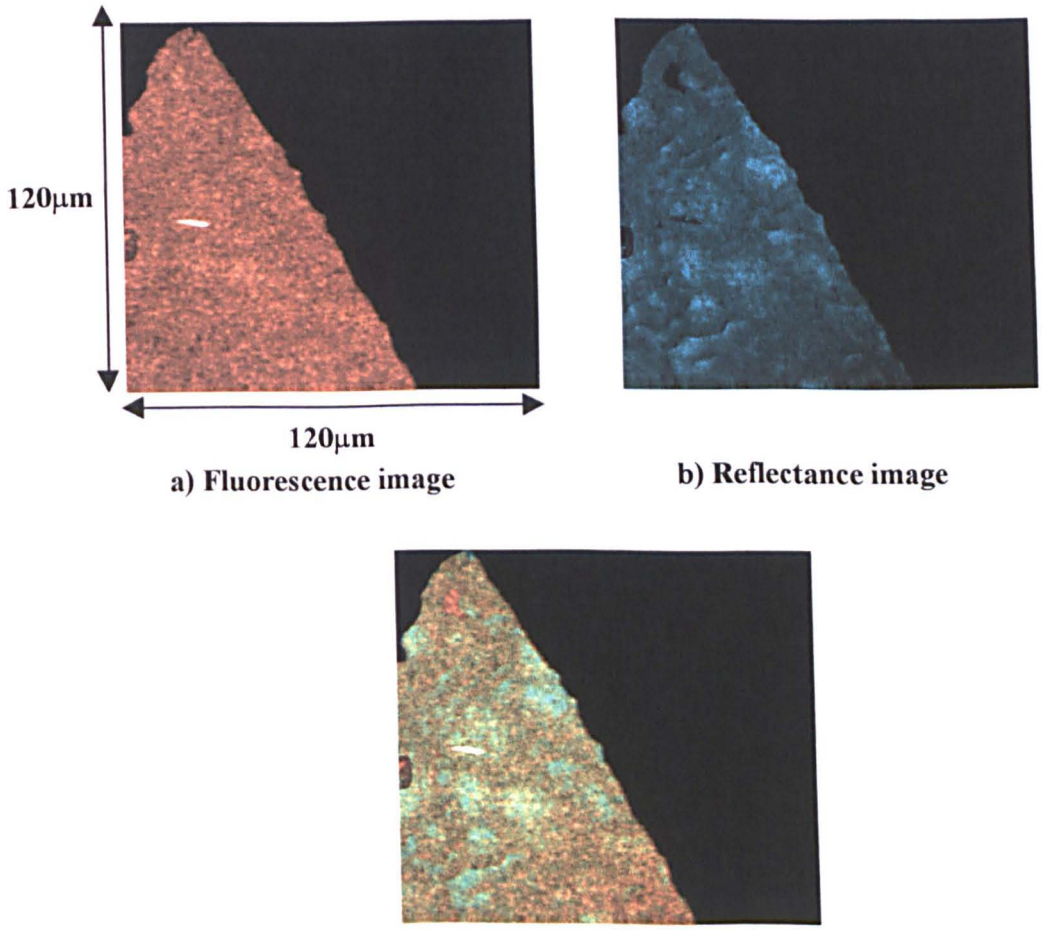

Figure 6.2: Combining fluorescence and reflectance confocal images from Nichia InGaN SQW sample.

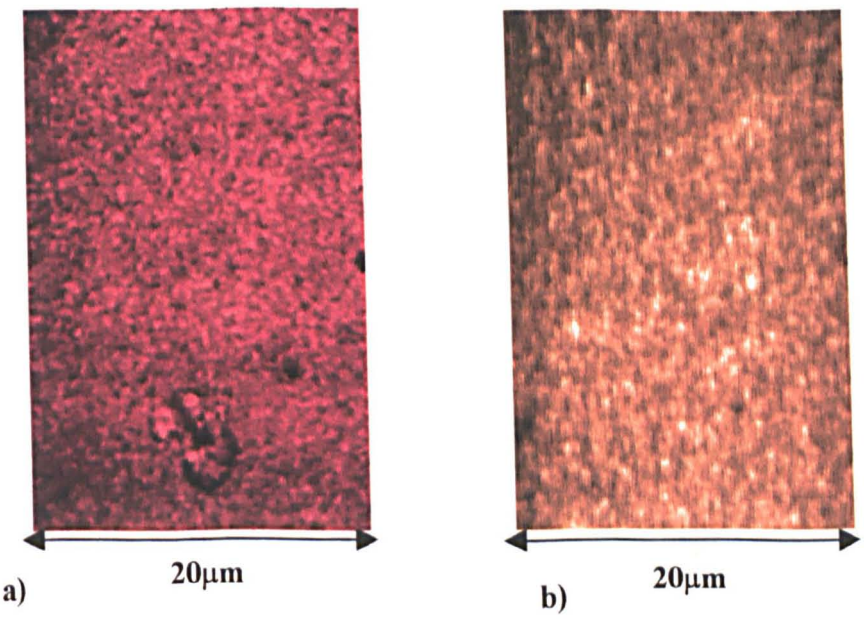

Figure 6.3: Fluorescence images from InGaN QB samples a) N399 and b) N400.

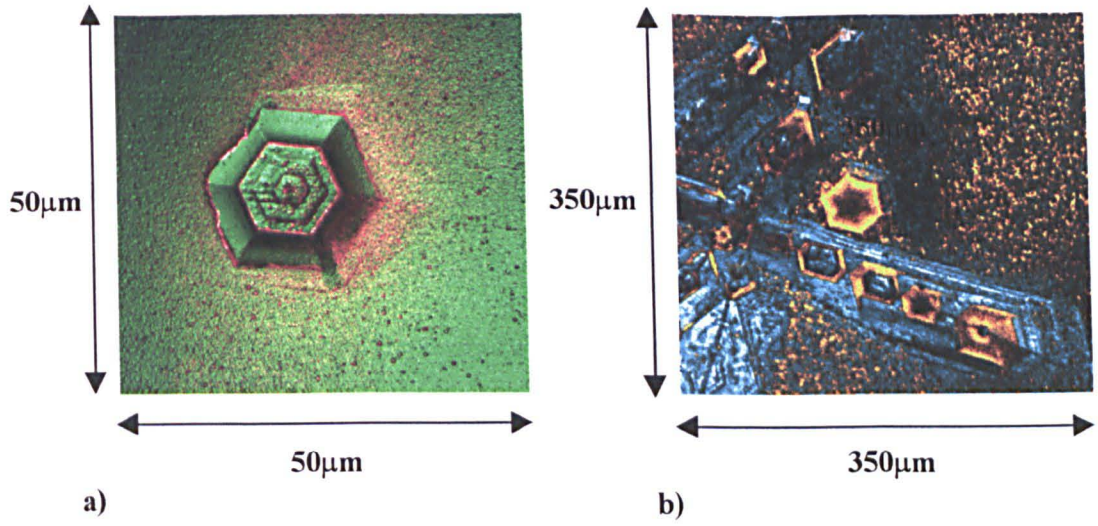

Figure 6.4: Composite confocal images from a) InGaN 85 and b) InGaN 336.

In both fluorescence and reflectance images, the sample surface appears uneven and granular. A variety of different 'textures' were seen on the images, ranging from spotty to zigzag like patterns. On the epilayer samples a large number of hexagonal structures were observed. Comparing Figures 6.1 a) and b), 6.2 a) and b) and in Figure 6.4, the non-reflecting areas of the sample were found to fluoresce strongly and vice-versa; few regions on the sample are found to be bright in both. Combining the fluorescence and reflectance images may therefore form a complete image of the sample surface. Some of the dark spots present in both images may be due to ice-crystals forming on the surface of the sample stage. In addition, scratches, residue vacuum grease and dirt on the sample were observed in a number of the images.

Spatial variation in the fluorescence from hexagonal structures has also been seen in cathodoluminescence studies of InGaN epilayers [1]. Furthermore, the CM reflectance images from InGaN 85 are similar to those obtained from the CCD camera installed in the EPMA, as described in Chapters 3 and 5.

Granular contrast can be observed in these low-resolution images and by changing the magnification of the CM, the surface of the sample may be studied more closely and regions of interested zoomed in on. CM images at various magnifications are shown in Figure 6.5. A larger magnification lens was used in the CM to take these images and glycerol placed between the lens and the sample surface to act as a refractive index matching fluid. The resolution of the system allows individual grains ~1μm in diameter to be distinguished.

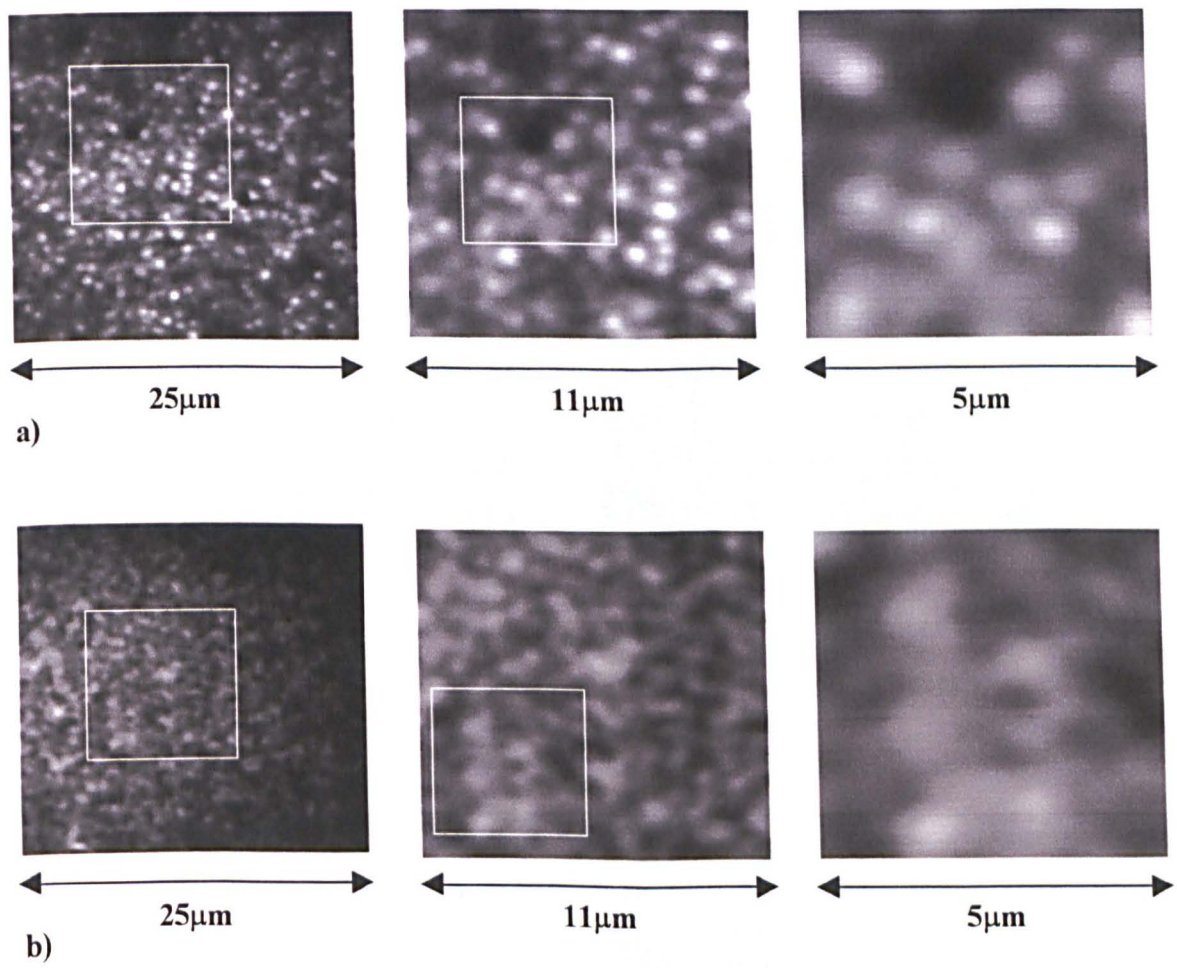

Figure 6.5: Samples a) InGaN 85 (epilayer) and b) N399 (QB) at different magnifications. The white box indicates the region of the sample selected for closer examination.

6.3 Temperature Dependence of the Fluorescence Image Intensity

CM images were taken of the samples at various temperatures using a Linkam HFS91 liquid nitrogen cooled stage to control the temperature. As shown in Figure 6.6, lowering the sample temperature greatly increased the fluorescence efficiency of the material and therefore improves the quality of the image. It was found that an increase in the brightness by a factor of up to ~50 may be obtained between room temperature and 77K. Moreover, in some cases different image features show different temperature dependencies. The reflectance images however, do not change with temperature.

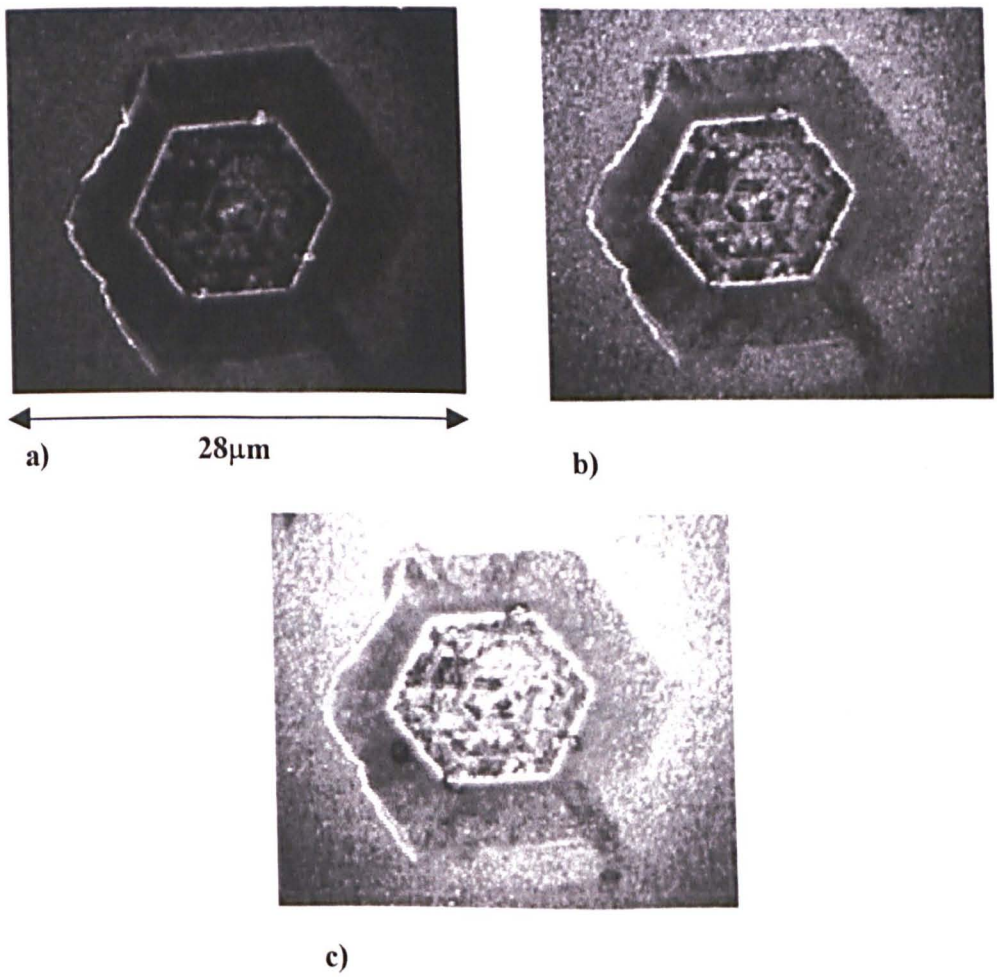

Figure 6.6: Temperature dependence of fluorescence from InGaN 85 captured by CM at a) –50°C, b) –100°C and c) –150°C.

6.4 Confocal Microscopy with Spectroscopy

Photoluminescence spectroscopy measurements were taken in conjunction with the confocal imaging. This was done in two different ways as outlined in the following sections.

6.4.1 Spectroscopic Imaging

Keeping all other conditions constant, an initial and somewhat crude form of spectroscopy was carried out by placing a series of 10nm bandpass filters in the fluorescence channel. Filters from 480nm to 800nm were used. Low temperature fluorescence images for three different bandpass filters centred at 520nm, 580nm and 640nm are shown in Figure 6.7 along with the panchromatic fluorescence image above 515nm, restricted by the response of the dichroic mirror. The low temperature PL spectrum taken from the equivalent position on the sample using an argon ion laser, as described in Chapter 3, Section 3.1.2, is also shown. A change in the intensity of the fluorescence image was observed for different bandpass filters: in Figure 6.7 c), d) and e), the intensity of the image decreases with increasing centre wavelength of the bandpass filter. This result may be expected on comparison with the PL spectrum from the sample as shown in Figure 6.7b). It was also noted that in Figure 6.7 d) and e) there are some luminescent features present that are not seen in Figure 6.7c). These features may be related to yellow band emission from the sample.

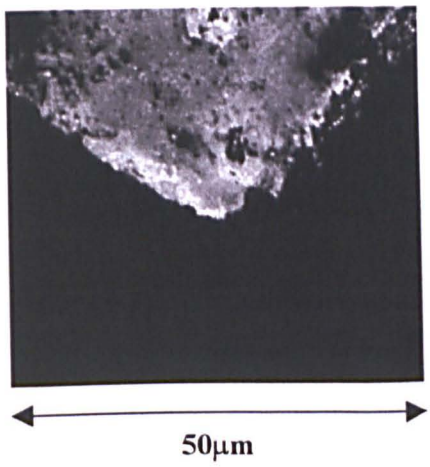

a) Panchromatic above 515nm (no filter)

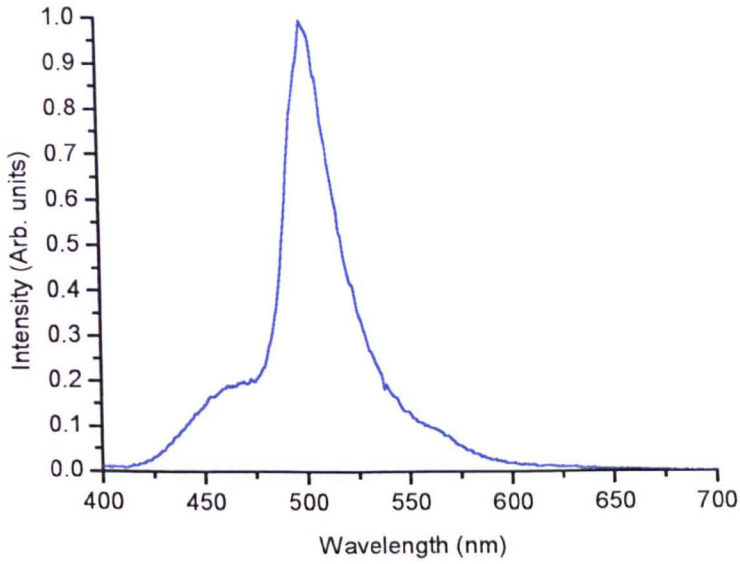

b) PL spectrum, peak emission wavelength ~500nm

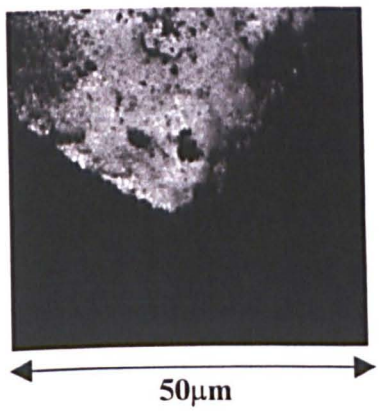

c) 520nm bandpass filter

d) 580nm bandpass filter

e) 640nm bandpass filter

Figure 6.7: Quasi-monochromatic images of InGaN by placing a 10nm bandpass filter in the fluorescence channel.

6.4.2 PL Spectroscopy and Reflectance Imaging

The PL spectrum was recorded by a spectrometer with a CCD detector array in the fluorescence channel of the CM in place of the fluorescence PMT. The spectrometer was calibrated using the 442nm laser line of a HeCd laser and a 632nm laser diode

as reference points. A background spectrum was taken and automatically subtracted from the PL spectrum in order to correct for background light.

Room temperature PL spectroscopy was carried out at various different positions on the sample surface. The reflectance image was also taken and used to indicate any features of interest. As shown in Figure 6.8 a) and b), the PL spectrum was measured over different sized regions of the sample. Furthermore, by stopping the scanning mirrors, PL may be taken at a selected spot, in this case from a bright and a dark spot in Figure 6.8b). From the results in Figure 6.8c) and for a number of other InGaN samples it was found that on examining different regions of the sample only the intensity of the PL spectrum changes; the PL peak emission does not differ.

Fringing present on the PL spectra in Figure 6.8c) is probably due to the effects of the dichroic response function. A low temperature PL spectrum of the sample excited with a HeCd laser using the PL set-up described in Section 3.1.2, Chapter 3 is also shown on the figure for comparison.

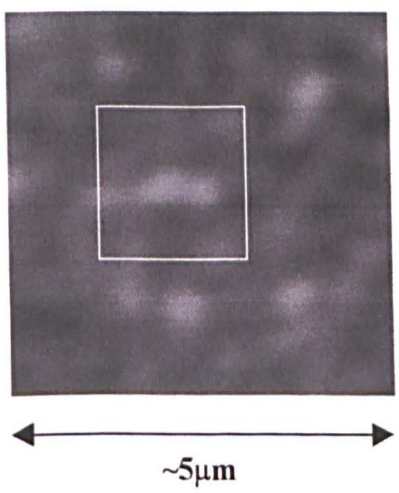

a) Reflectance image from InGaN Str115, the white box outlines the region of the sample selected for closer examination

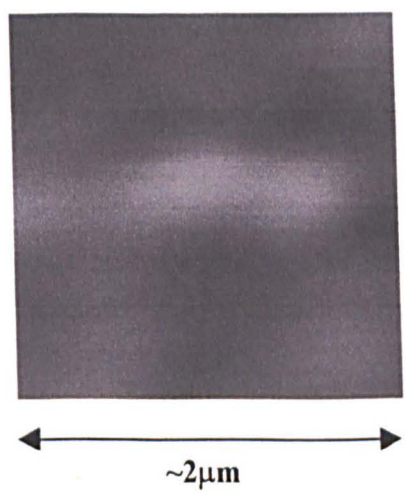

b) Zoom in on reflectance image

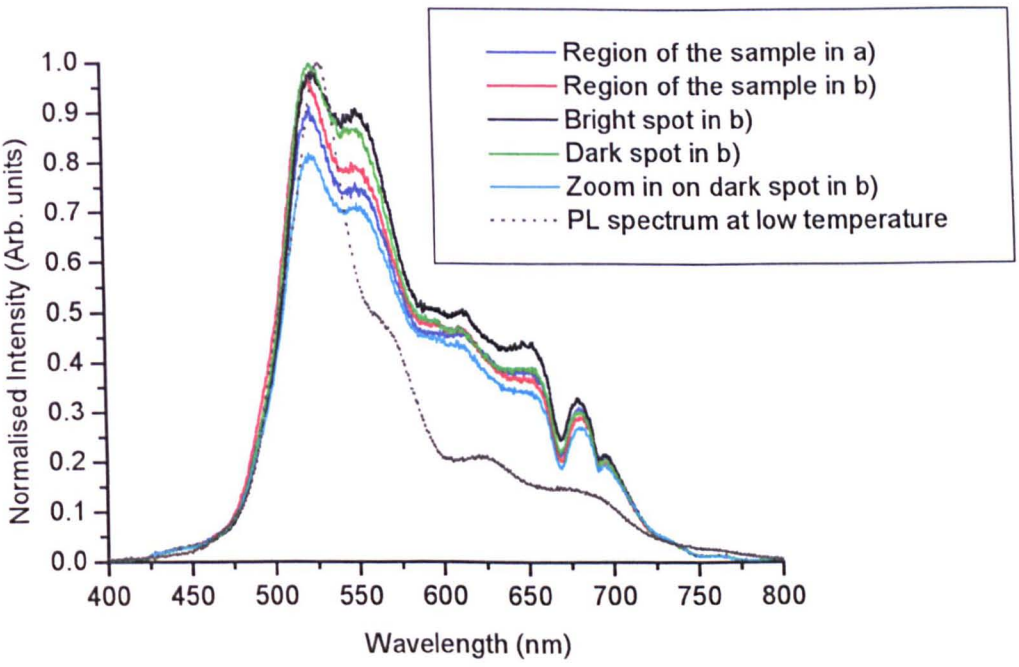

c) PL spectra recorded at different positions on the images shown in a) and b)

Figure 6.8: Reflectance imaging and PL spectroscopy of sample InGaN Str115.

6.5 Analysis of the Confocal Microscopy Results

From the CM images, as shown in Figures 6.1 to 6.5, the surface morphology of the InGaN samples was found to be granular in appearance with hexagonal structures present in some of the samples. The granular appearance in the fluorescence images may be due to luminescence segregation of the material into small bright spots ~1μm to 10μm in diameter separated by surrounding darker regions. This granular appearance in the fluorescence image was seen in all of the epilayer, QW and QB samples.

As shown in Figure 6.6, on lowering the temperature of the sample the luminescence efficiency of the material improves. A similar dependence on the luminescence

intensity with temperature was also observed in the PL spectroscopy measurements presented in Chapter 4, Section 4.4.3. The relationship between luminescence intensity and temperature may be explained by an increase in the number of non-radiative sites in the material becoming active at higher temperatures. The luminescence efficiency is therefore lowered due to the quenching effect of the non-radiative sites. The different temperature dependencies from some of the image features may then be a result of the number of non-radiative sites present at that particular region of the sample.

As described previously in Chapter 4, in conventional PL spectroscopy an average value of the luminescence is recorded over a macroscopic area approximated by the laser spot size. However, by inserting bandpass filters in the fluorescence channel of the CM, spectroscopic information on the material may be determined on a much higher resolution from the quasi-monochromatic fluorescence images of the sample surface. From the results shown in Figure 6.7 and from many other samples, it was found that there is a change in the fluorescence image depending on the centre wavelength of the bandpass filter used [2,3]. The intensity of the image varies with the bandpass filter wavelength and follows the change in intensity as shown by the PL spectrum taken from the equivalent position on the sample. However, direct comparison of the images reveals that despite a few regions where bright spots are found in one image with a corresponding dark spot in all the other images, the majority of spots are evident in all images, with only the intensity of the spots being found to change. This suggests that the fundamental structures responsible for emission in InGaN are smaller than the μm-scale grains observed in the fluorescence

images. Unfortunately, quantitative results are difficult to obtain using this technique and there is at present no data evaluation system available to extract the wealth of information given in a single fluorescence image. The set-up also suffers from calibration problems such as the different responses of the bandpass filters used.

The CCD spectrometer measures the PL spectrum directly from a selected region on the sample. As shown from the results in Figure 6.8, it was found that the intensity of the PL spectrum changes depending on the region of the material addressed. The peak emission energy however does not change and the general shape of the PL spectrum varies very little. This indicates that the origin of InGaN luminescence is smaller than the diffraction limited 1μm laser spot sized used. It also suggests that this fundamental structure is present in both the bright and dark regions seen in the reflectance images.

Although a large quantity of images and data can be obtained using CM, a number of problems limit the usefulness of the CM results. In addition to the difficulties outlined previously, an uneven distribution of light in the field of view makes direct comparison of the intensity of the images and image features difficult. Furthermore, the formation of ice layers on the sample stage obscures the image during low temperature studies of the samples.

6.6 Summary

Confocal microscopy was used to examine InGaN. From the CM images taken on InGaN epilayer, QW and QB samples the surface of the material was shown to be uneven and granular in appearance. Magnification of the fluorescence image revealed that the luminescence may segregate into bright and dark spots, some as small as ~1μm in diameter (the resolution limit of the system). On lowering the temperature of the sample the luminescence efficiency of the material was found to increase. Furthermore, spectroscopic imaging of the samples showed that the intensity of the fluorescence image depends on the centre wavelength of the bandpass filter used, as expected on comparison with the PL spectrum. The majority of bright spots present in a given quasi-monochromatic fluorescence image were also found in all the other fluorescence images from that region of the sample. This indicates that the origin of InGaN luminescence is smaller than the μm-scale spots observed. Moreover, whilst the intensity of the PL spectra taken at different positions on the reflectance image was found to change, the PL peak emission energy did not. This is further evidence that the structure responsible for InGaN luminescence is smaller than each of the μm-scale grains seen and is present in both the bright and dark spots in the reflectance image.

6.7 References

[1] P. G. Middleton, C. Trager-Cowan, A. Mohammed, K. P. O'Donnell, W. Van der Stricht, I. Moerman and P. Demeester, Mat. Res. Soc. Symp. Proc. **449**, 471 (1997).

[2] K. P. O'Donnell, M. J. Tobin, S. C. Bayliss and W. Van der Stricht, Jnl. of Microscopy, **193**, 1 (1999).

[3] K. P. O'Donnell, C. Trager-Cowan, S. Pereira, A. Bangura, C. Young, M. E. White and M. J. Tobin, phys. stat. sol. (b) **216**, 157 (1999).

CHAPTER 7: LOCAL STRUCTURE ANALYSIS OF InGaN EPILAYER AND QB SAMPLES USING EXAFS

7.1 Introduction

EXAFS at the indium K-edge provides a unique tool for characterising the local structure of InGaN. Local structure parameters derived from EXAFS measurements of pure InN, a set of InGaN epilayers grown by MOCVD, with a range of indium nitride content, and an uncapped InGaN QB sample grown by MBE are presented and discussed. The results from the QB sample are compared with those from an epilayer sample of similar nominal indium nitride content and also with the pure InN sample. Information on the local structure of InGaN may yield an indication as to the physical structures responsible for the optical properties of the material.

A description of EXAFS is given in Chapter 3, Section 3.2.4 and details of the investigated samples in Appendix A.

7.2 EXAFS from the InN and the InGaN samples

X-ray absorption spectroscopy was carried out at the Daresbury Laboratories, Warrington, on a series of InGaN epilayers, an uncapped InGaN QB sample and a piece of pure InN thin film, deposited by sputtering on a glass substrate at 500°C and which was used as a calibration standard. A typical X-ray absorption spectrum (XAS) from an InGaN epilayer, showing the EXAFS oscillations above the indium K-edge, was presented in Chapter 5, Figure 5.4. The XAS is a function of photon energy; however, in order to carry out structural analysis, the XAS must first be

transformed into EXAFS, a function of excess photoelectron momentum. This was done by subtracting the edge energy from the XAS spectrum, resulting in an energy value of ΔE which was changed into wavevector notation, k, using equation 7.1;

$$k = \frac{\sqrt{2m\Delta E}}{h} \qquad \textbf{Equation 7.1}$$

where m and h are electron mass and Planck's constant respectively. The background step then was subtracted and equation 7.2 used to weight the spectrum, to emphasise the high-k region;

$$\text{WEIGHED EXAFS} = \text{EXAFS} \times k^n \quad (n = 2 \text{ or } 3) \qquad \textbf{Equation 7.2}$$

EXAFS oscillations for one of the InGaN epilayer samples and a two-shell model fit to the oscillations is shown in Figure 7.1. EXAFS of the model environment were calculated and refined to match the experimental EXAFS spectrum using EXCURV98 [1,2,3].

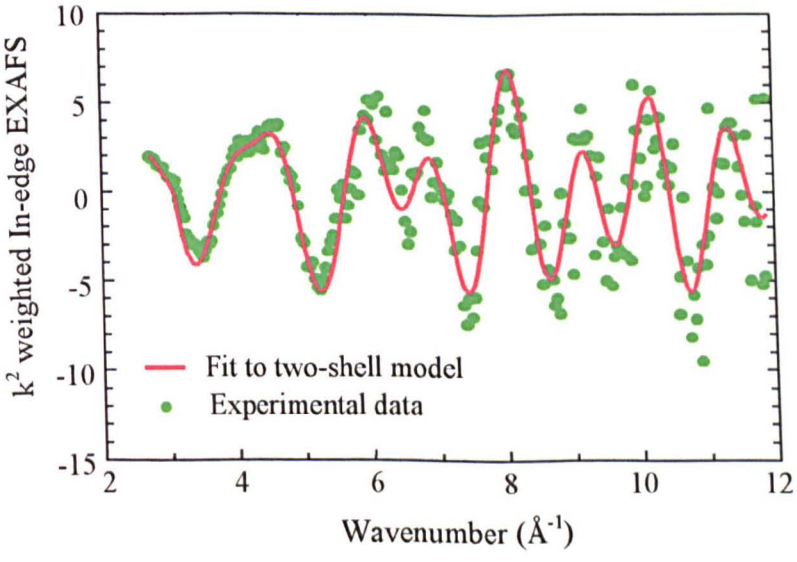

Figure 7.1: EXAFS oscillations derived from the XAS of an InGaN epilayer; a two-shell model fit to the data is also shown in the figure.

The Fourier Transform of the EXAFS spectrum produces an atomic radial distribution function (RDF), which maps the neighbouring atoms in the vicinity of the probe atom as a set of peaks. This provides a visual guide to the radial separation between the neighbouring atoms and the probe atom. However, these values are only an approximation and have been corrected for atomic phase shifts in the local structure parameters as given in Tables 7.1, 7.2 and 7.3. The RDF plot for an InGaN epilayer and the QB sample are shown in Figures 7.2. and 7.3.

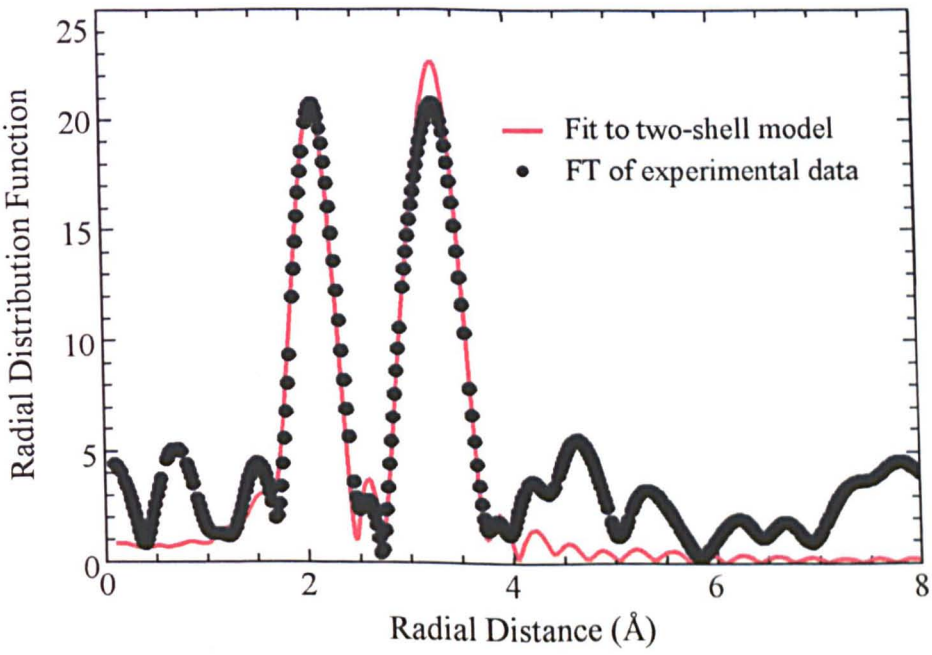

Figure 7.2: RDF function and fit derived from EXAFS of an InGaN epilayer.

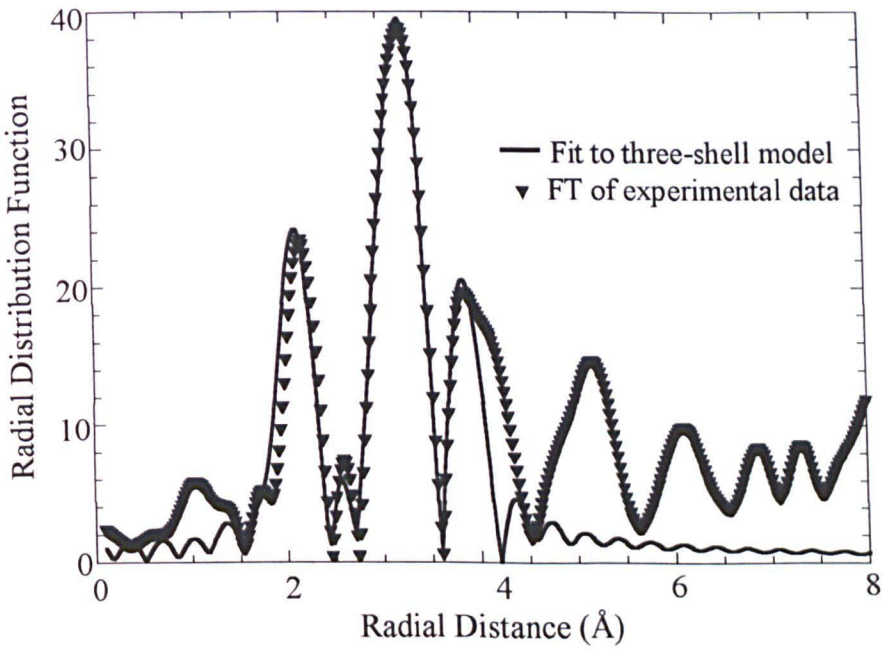

Figure 7.3: RDF function and fit derived from EXAFS of the QB sample.

Local structure parameters derived from the shell model fit to the EXAFS data are presented in Tables 7.1, 7.2 and 7.3 for the pure InN sample, the set of InGaN epilayers and the uncapped InGaN QB sample respectively [3,4]. The fitting model made use of a simple tetrahedral geometry that does not distinguish wurtzite and cubic lattices. The Debye-Waller factor determined for each shell fitting is also given in the tables. This provides a measure of the combined structural and thermal disorder of the neighbouring atom shells.

Sample No. of scans	Atom Type	Number of Atoms	Interatomic Distance (Å)	Debye-Waller Factor ($Å^2$)
InN	N	4	2.16(2)	0.009(1)
2	In	12	3.53(3)	0.018(2)
	In	6	4.97(5)	0.024(3)

Table 7.1: Local structure parameters of InN sputtered layer sample used as calibration standard determined by EXAFS.

Sample No. of scans	Atom Type	Number of Atoms	Interatomic Distance (Å)	Debye-Waller Factor ($Å^2$)
InGaN 85	N	4	2.10(2)	0.011(1)
8	0.83(6) Ga	12	3.26(3)	0.012(1)
	/0.17 In			
InGaN 336A	N	4	2.10(2)	0.006(1)
4	0.77(6) Ga	12	3.28(3)	0.014(2)
	/0.23 In			
	0.77(6) Ga	6	4.85(5)	0.006(1)
	/0.23 In			
InGaN 336A	N	4	2.11(2)	0.007(2)
10	0.74(5) Ga	12	3.28(3)	0.013(2)
	/0.26 In			
InGaN 336A	N	4	2.11(2)	0.009(1)

10	0.67(5) Ga /0.33 In	12	3.29(3)	0.010(2)
InGaN 336X 4	N 0.62(4) Ga /0.38 In	4 12	2.11(2) 3.29(3)	0.007(1) 0.011(2)

Table 7.2: Local structure parameters of the InGaN epilayers determined by EXAFS.

Sample No. of scans	Atom Type	Number of Atoms	Interatomic Distance (Å)	Debye-Waller Factor ($Å^2$)
InGaN N401 220	N Ga In	4 7.4 4.6	2.10(2) 3.22(3) 3.56(5)	0.006 0.008 0.008

Table 7.3: Local structure parameters of the uncapped InGaN QB sample determined by EXAFS.

7.3 Analysis of the Local Structure Parameters Derived from EXAFS

As shown in Table 7.1, the interatomic distance of In-N_1 (where the subscript denotes the shell number) in the InN calibration sample was 2.16(2)Å. This is approximately equal to the experimentally determined value from the literature for bulk InN, ~2.16Å [5].

From the results of the InGaN epilayer samples, in Table 7.2, the radial separation of the atoms surrounding the target indium atom was found to vary little with a change in the indium nitride content. This does not follow the predicted trend as expected from Vegard's Law:

$$c_0(InGaN) = c(GaN) + x(c(InN) - c(GaN)) \qquad \textbf{Equation 7.3}$$

which assumes that the relaxed lattice constant $c_0(x)$ of a binary mixture of compounds scales linearly with the composition value, x.

For the InGaN epilayers with x=0.17 to x=0.38, as shown in Table 7.2, the radial separation between In-N_1 was constant within the measurement error for all the samples, with a mean value of 2.11(2)Å. This value is closer to the interatomic spacing of the pure InN sample (2.16Å) than that of GaN (1.95Å) and is also larger than the radial separation calculated by Vegard's Law, which is estimated to increase from 1.98Å to 2.03Å over the given composition range. The composition values were shown to be comparable with those obtained from the same samples using EPMA and RBS in Chapter 5. Moreover, the radius of the first metal shell derived from the EXAFS increases from only 3.26Å to 3.29Å as compared to 3.25Å to 3.32Å using Vegard's Law. The mean radius of the first metal shell is therefore ~3.28(3)Å, which is closer to that of Ga-Ga in bulk GaN (3.19Å) than that of In-In (3.54Å) in bulk InN [3,5,6].

Similar results have been obtained by Miyajima et al. from EXAFS measurements on a set of InGaN epilayer samples with indium nitride content, x, ranging from 0.01

$\leq x \leq 0.21$ [7]. The authors reported a constant In-N_1 bond length of ~2.10Å. It was also found that for $x<0.16$, the In-In_1 and In-Ga_1 interatomic distances were close to that of the Ga-Ga distance in bulk GaN. Furthermore, the co-ordination numbers found for the number of indium second nearest neighbour atoms to the indium probe atom were consistently higher than estimated for an ideal random InGaN alloy. The results were attributed by the authors to the segregation of indium atoms in InGaN, starting for composition values as low as $x\sim0.01$ [7].

A theoretical study by Matilla and Zunger of the local structure of InGaN alloys using valence force field simulations calculated that the In-N_1 distance should be insensitive to the composition of the material [8]. However, this theoretical value was typically >2.12Å and therefore higher than that obtained from EXAFS. The calculated In-In_1 and In-Ga_1 separations are also higher than the experimental values. The theoretical calculation adheres to Vegard's Law whereas the experimental results do not show any evidence to support this.

From the results as shown in Figure 7.3, EXAFS of the InGaN QB sample can be fitted to at least three shells of neighbours all within a radius of 4Å. The In-N_1 distance, in Table 7.3, was found to be 2.10(2)Å, similar to that in the InGaN epilayer samples. An inner metal shell which contains only gallium atoms was at a distance of ~3.22Å and an outer metal shell with only indium atoms at ~3.56Å.

The fitting parameters from the InN sample, a selected InGaN epilayer and the InGaN QB are compared in Table 7.4. As the QB sample has a nominal indium

nitride fraction of x~0.25, estimated from RHEED intensity oscillations [9], the InGaN epilayer sample with an indium nitride content as close to this value as possible was used in the comparison. In Figure 7.4, the RDF functions for each sample as derived from the EXAFS are plotted together.

Sample (Type)	Atom Type	Number of Atoms	Interatomic Distance (Å)	Debye-Waller Factor ($Å^2$)
InN	N	4	2.16(2)	0.009
(sputtered	In	12	3.53(3)	0.018
thin-film)	In	6	4.97(5)	0.024
InGaN336A	N	4	2.11(2)	0.007
(epilayer)	0.74(5) Ga	12	3.28(3)	0.013
	/0.26 In			
InGaN N401	N	4	2.10(2)	0.006
(QB)	Ga	7.4	3.22(3)	0.008
	In	4.6	3.56(5)	0.008

Table 7.4: Local structure parameters of the InN, InGaN epilayer and InGaN QB sample determined by EXAFS.

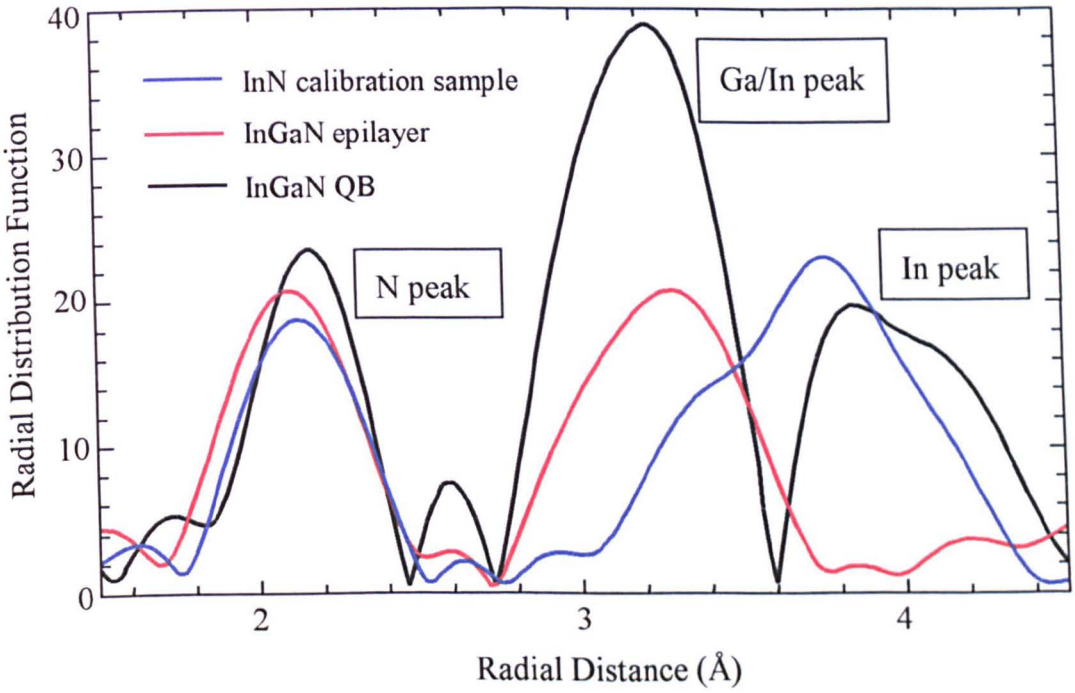

Figure 7.4: Comparison of RDF functions derived from EXAFS of the InN, InGaN epilayer and InGaN QB sample.

As shown in Table 7.4, the In-N_1 interatomic spacing for each sample is similar, and, in Figure 7.4, a peak at ~2.11Å is present for all three samples, close to the In-N_1 distance for bulk InN of ~2.16Å [5]. However, from the metal shell fitting in the QB sample, for a radial distance from the probe indium atom of between 2.7Å and 4.5Å (see Figure 7.4), the QB sample exhibits elements of both the pure InN sample and the InGaN epilayer. These results indicate that there are two distinct environments for the indium atoms in the QB sample; one is InN-like and the other resembles the indium environment in a gallium rich InGaN alloy. The mean second shell separation as shown in Figure 7.4 is ~3.21Å, which is close to the interatomic spacing of Ga-Ga in bulk GaN of ~3.19Å [6]. Using Vegard's Law this value corresponds to an indium nitride content of x~0.06. From the parameters in Table

7.4, the amount of indium in each of the two-phases is in the ratio [InN]:[$In_xGa_{1-x}N$] ~ 2:3. For an indium nitride content of x~0.06, using equation 7.4, the InN phase was calculated to occupy only ~4% of the total volume in the sampled region [4].

$$\text{Filling factor, f.f.} = \frac{2x}{(3-2x)} \qquad \textbf{Equation 7.4}$$

The two-phase mixture in the InGaN QB sample, an InN-like and a gallium rich InGaN alloy may be explained by the presence of InN-rich QDs formed in InGaN as a result of phase segregation. It has been predicted that the InN-rich QDs are embedded in an otherwise gallium rich InGaN matrix [10]. The results obtained from the InGaN QB sample would suggest that this is correct. However, a similar two-phase mixture with InN-like regions may also be expected to occur in the epilayer samples, whereas a single phase resembling a simple InGaN alloy was observed from the EXAFS. This is tentatively ascribed to a smaller quantity of InN-rich QDs forming in the epilayer material which may not be sufficient to be distinguished as a separate phase in EXAFS measurements. Although EXAFS provides microscopic information on the material, it does so through selective sensitivity to purely local interaction and not by addressing a suitably small region of the sample. Therefore, the EXAFS parameters obtained do not necessarily represent an actual spatial object but rather a pattern of resultant interactions [4].

7.4 Summary

In this chapter the local structure parameters derived from EXAFS of an InN sputtered layer thin-film, a set of MOCVD grown InGaN epilayers with different

indium nitride content, and a MBE grown uncapped InGaN QB sample were presented and discussed. The In-N_1 spacing in the epilayers was found to be close to that obtained for the pure InN sample and to that in the literature. This value is higher than that calculated using Vegard's Law and varies much less than predicted over the composition range determined. Furthermore, the interatomic spacing of the first metal shell also varies less than expected from Vegard's Law and has a mean radius value closer to the Ga-Ga separation in bulk GaN than that of In-In in bulk InN. Fitting parameters from other EXAFS measurements taken from the literature agree with these results. However, the values obtained experimentally were found to be lower than those calculated in a theoretical study of the local structure of InGaN alloys.

Comparing the local structure parameters of the InN sample, a selected InGaN epilayer and the InGaN QB sample, it was found that the In-N_1 separation is similar in all three. Nevertheless, the metal shell fitting of the epilayer sample showed a single-phase InGaN alloy while the InGaN QB sample exhibited a two-phase mixture of components, one of which is nearly pure InN. From the parameters the indium nitride content in the gallium rich InGaN alloy was calculated to be only $x \sim 0.06$ and the volume of the material determined to be InN-like ~4%. These results may be explained by the presence of InN-rich QDs in the sample as a result of phase segregation in InGaN. The QB sample, unlike the epilayer, may have sufficient quantities of these QDs such that they can be detected as a separate entity by EXAFS modelling.

7.5 References

[1] Daresbury Laboratories website: http://srs.dl.ac.uk/XRS/Theory/theory2.html.

[2] N. Binsted, EXCURV98, CCLRC Daresbury Laboratories Computer Program (1998).

[3] K. P. O'Donnell, J. F. W. Mosselmans, R. W. Martin, S. Pereira and M. E. White, J. Phys.: Condens. Matter. **13**, 6977 (2001).

[4] K. P. O'Donnell, M. E. White, S. Pereira, J. F. W. Mosselmans, N. Grandjean, B. Damilano and J. Massies, Mat. Sci. Eng. B **93**, 150 (2002).

[5] V. A. Tyagai, A. M. Evstigneev, A. N. Krasiko, A. F. Malakhov and V. Ya, Fiz. Tekh. Poluprovodn. **11**, 2142 (1977).

[6] T. Detchprohm, K. Hiramatsu, K. Ito and I. Akasaki, Jpn. J. Appl. Phys. **31**, L1454 (1992).

[7] T. Miyajima, Y. Kudo, K.-Y. Liu, T. Uruga, T. Asatsuma, T. Hino and T. Kobayashi, phys. stat. sol. (b) **228**, 45 (2001).

[8] T. Mattila and A. Zunger, J. Appl. Phys. **85**, 160 (1999).

[9] N. Grandjean and J. Massies, Appl. Phys. Lett. **72**, 1078 (1998).

[10] K. P. O'Donnell, R. W. Martin and P. G. Middleton, Phys. Rev. Lett. **82**, 237 (1999).

CHAPTER 8: PHOTOLUMINESCENCE EXCITATION SPECTROSCOPY OF InGaN EPILAYERS, QWS AND QBS

8.1 Introduction

Photoluminescence (PL) from InGaN spans the spectral range from the near ultraviolet to the infra-red [1,2]. However, knowledge of the corresponding optical bandgap energy, E_g(eV), is required in order to attain a clear understanding of exciton localisation in this material. Photoluminescence excitation (PLE) spectroscopy was used to investigate the excitation/emission cycle and to measure the optical bandgap of two different sets of InGaN epilayers, both grown by MOCVD, and a set of MBE grown QW and QB samples. PLE was taken at several fixed energies, from the emission peak to the spectral tail, of individual samples. The optical bandgap energies determined from the PLE measurements are compared with the detected emission energies. These results are compared with data from the literature and with previous optical absorption measurements on InGaN.

A description of PLE spectroscopy is given in Chapter 3, Section 3.1.6 and details of the investigated samples in Appendix A.

8.2 PLE Spectroscopy of MOCVD grown InGaN Epilayers

Prior to carrying out PLE spectroscopy, the low temperature (<25K) PL spectrum of each sample was measured as described in Chapter 3, Section 3.1.2, using either an argon ion laser or a HeCd laser as the excitation source. This was done in order to determine the range of detection energies for PLE measurements. The PL from the

two sets of samples show emission peaks ranging from 2.34eV to 1.85eV and from 2.82eV to 1.75eV, for the samples grown at Strathclyde University, and as part of the Brite Euram Project, Rainbow, respectively (Appendix A, Tables A.2 and A.3). Samples Str59, Str115, Str116 and Str117 exhibited two distinct emission peaks, one in either the blue or the green spectral region and one in the red, as shown in Figure 8.1. In such cases, the PLE spectra were recorded with the detection energy, E_{pl}(eV), fixed at both PL peaks and at several other energies, as indicated on the figure. Thin film interference within the layers caused fringing in the spectra of samples with smoother morphologies.

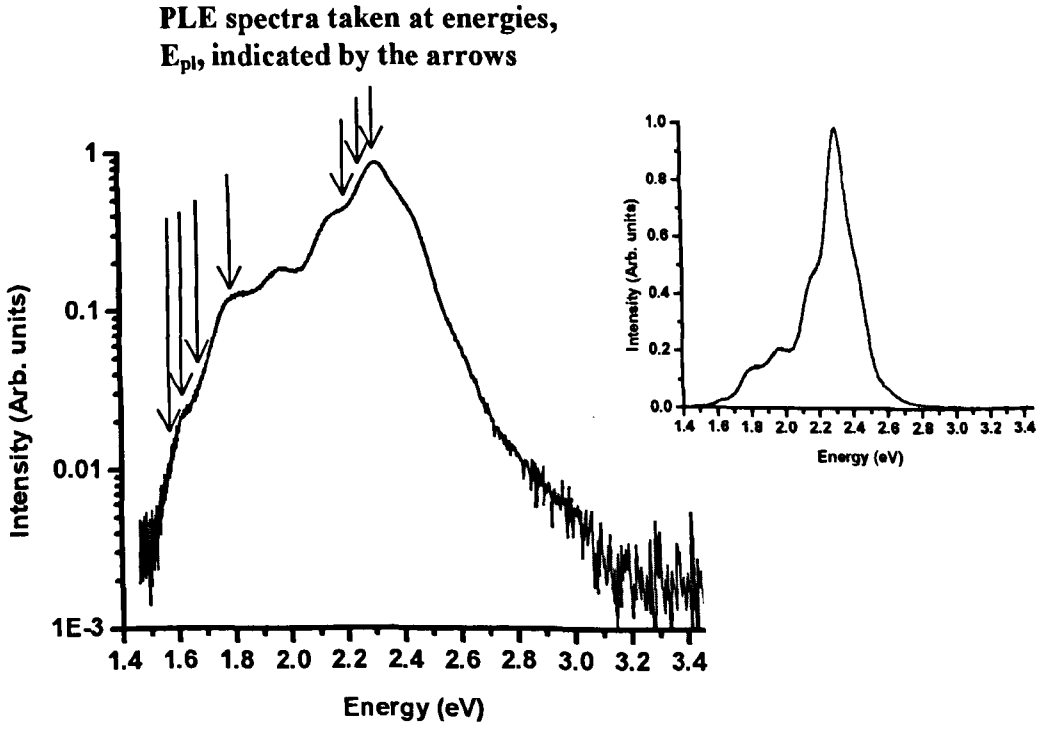

Figure 8.1: PL spectrum of sample Str115, a double-peak sample, showing selected PLE detection energies.

The PLE spectra from all the samples were found to have the same general shape, shown in Figure 8.2. The spectra were corrected for the combined throughput of the xenon lamp and the excitation monochromator, as described in Appendix B, Section B.2. The bandpass of the emission monochromator is ~1nm, which, when used with the front and back slits open 1mm, results in an uncertainty of ~5meV in the E_{pl} value.

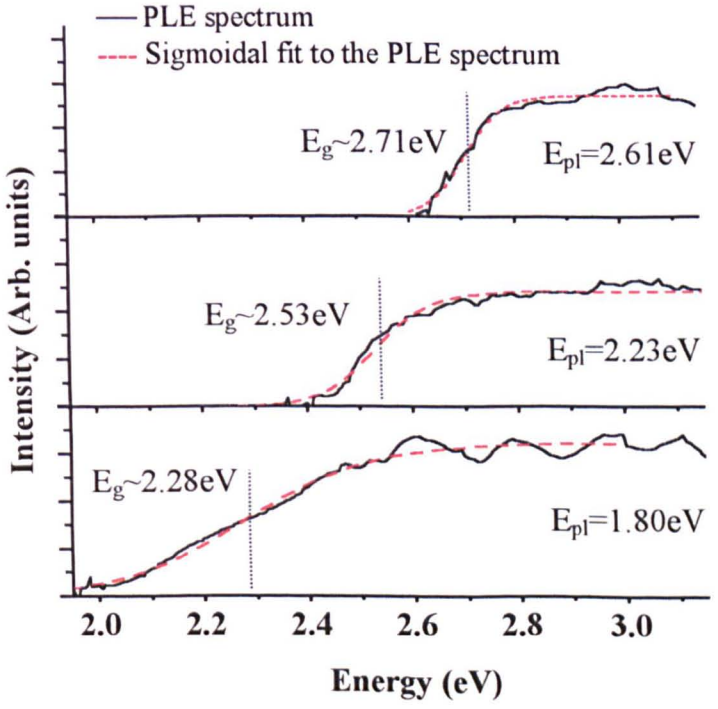

Figure 8.2: Selection of PLE spectra from MOCVD InGaN epilayers, samples S101, Str115 and Str117. The dashed lines (in red) are sigmoidal fits to the data (see text for details) and the dotted lines (in black) indicate E_g on the spectrum.

The bandgap energy, E_g(eV), was determined in each case by a fit to the low energy side of the PLE spectrum of the sigmoidal function [3]:

$$\alpha(E) = \frac{\alpha_0}{1+\exp\left(\frac{E_g - E}{\Delta E}\right)} \qquad \textbf{Equation 8.1}$$

where $\Delta E(eV)$ is a broadening parameter, α_0 is a constant and E(eV) is the excitation energy at which the intensity, α, is recorded.

As shown in Figure 8.2, E_g was found to decrease with the detection energy, E_{pl}. Furthermore, in Figure 8.3, E_g values obtained by monitoring the emission band of an individual sample also decreases with the detection energy.

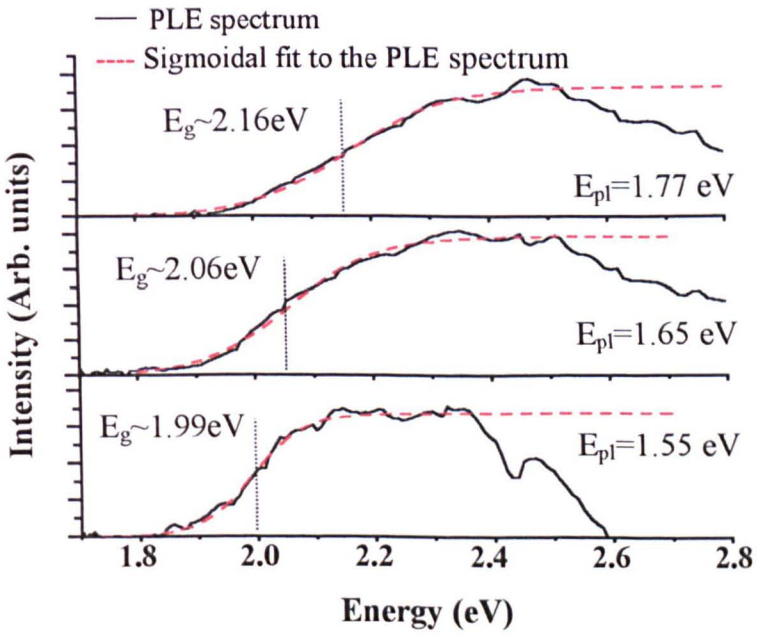

Figure 8.3: PLE spectra from sample Str115, for different detection energies.

Figure 8.4 presents a plot of E_{pl} against E_g for all samples measured. The results follow a linear trend, with a best-fit line;

$$E_{pl} = 1.382(39)E_g - 1.24(10) \qquad \textbf{Equation 8.2}$$

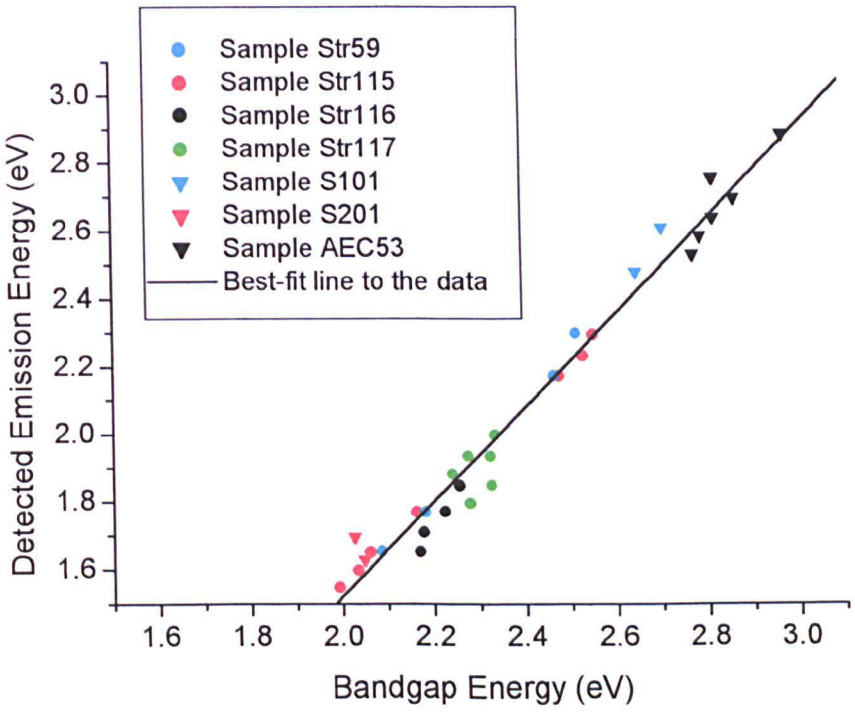

Figure 8.4: Detected emission energy, E_{pl}, against bandgap energy, E_g, for the MOCVD InGaN epilayers.

8.3 PLE Spectroscopy of MBE grown InGaN QWs and QBs

Low temperature (<25K) PL of the MBE samples show emission peaks ranging from 2.86eV to 1.96eV and from 2.78eV to 2.45eV, for the QW and QB samples, respectively (Appendix A, Tables A.4 and A.5). As seen in Figure 8.5, PLE was taken at several fixed energies, from the emission peak to the low energy side of the spectral tail. Moreover, as indicated in Figure 8.6, PLE was also taken at energies on the high energy side of the emission peak. This was done for two of the QW and one of the QB samples.

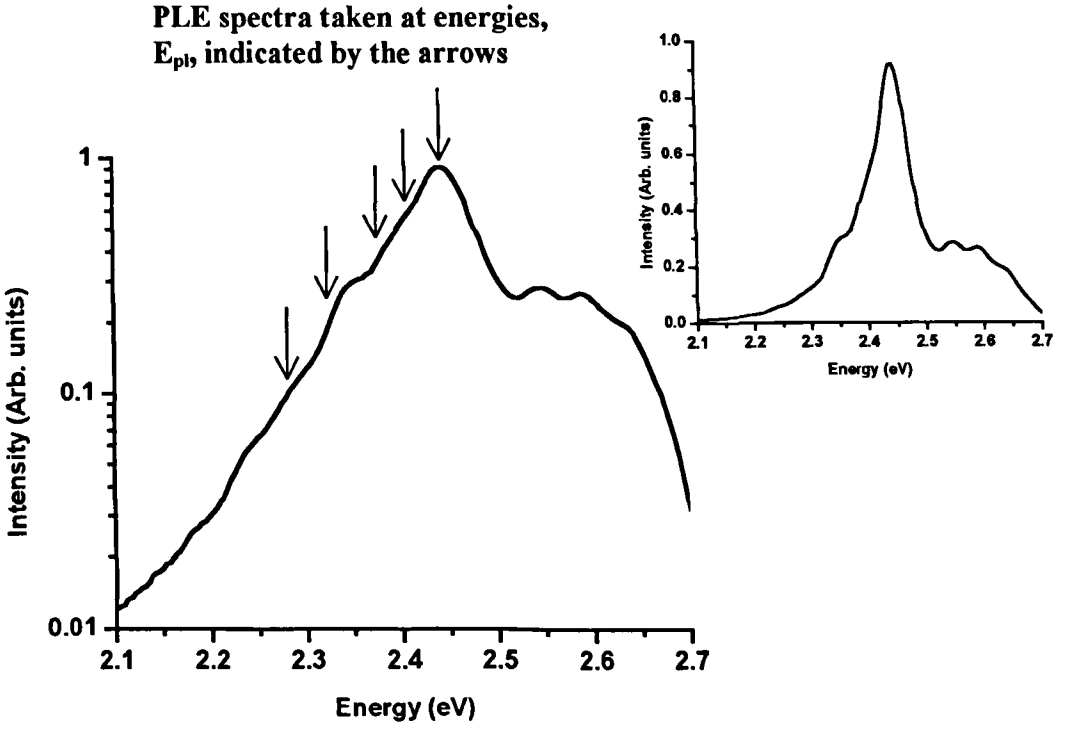

Figure 8.5: PL spectrum of sample N400 (QB), showing selected PLE detection energies.

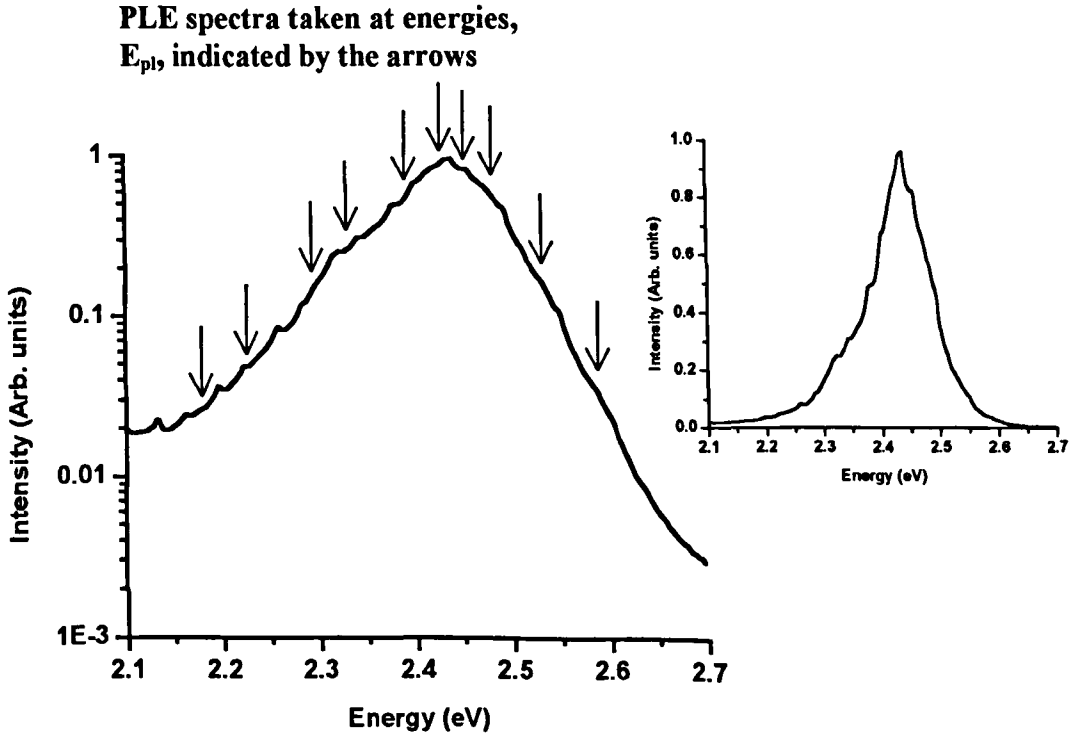

Figure 8.6: PL spectrum of sample N443 (QW), showing selected PLE detection energies.

The PLE spectra obtained from the QW and QB samples were found to have the same general shape (Figure 8.7) as that from the MOCVD samples (Figure 8.2).

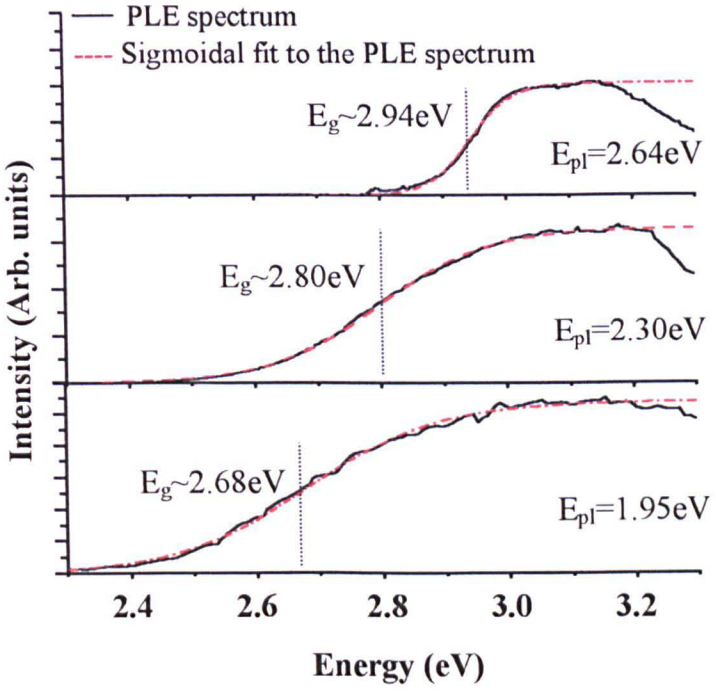

Figure 8.7: Selection of PLE spectra from MBE InGaN QWs and QBs, samples N399, N443 and N446.

The bandgap energy, E_g, was again determined for each spectrum using equation 8.1. As shown in Figure 8.7, E_g was found to decrease with the detection energy, E_{pl}. In Figures 8.8 and 8.9, it can be seen that E_g also decreases with detection energy within the emission band of an individual sample. Similar behaviour was observed for both the QW and QB samples.

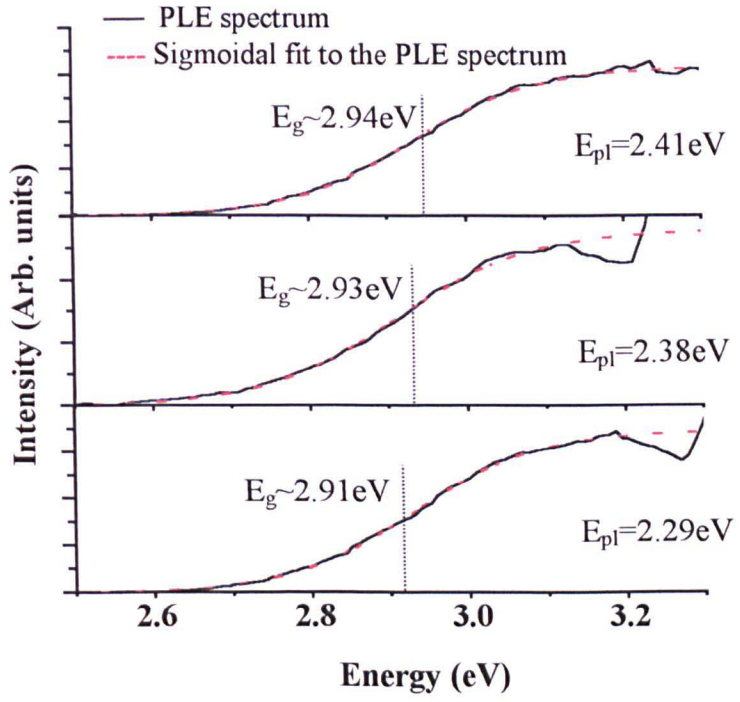

Figure 8.8: PLE spectra from sample N400 (QB), for different detection energies.

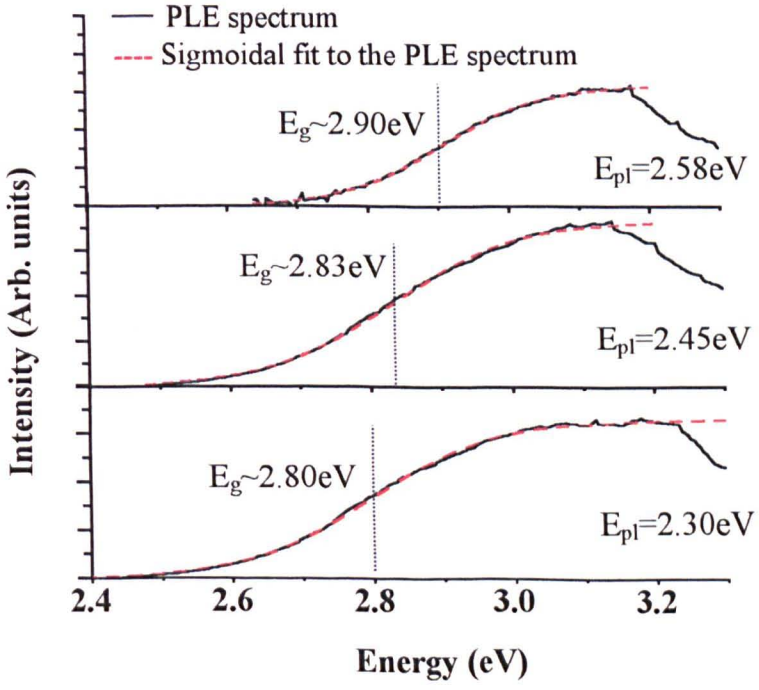

Figure 8.9: PLE spectra from sample N443 (QW), for different detection energies.

Figure 8.10 plots E_{pl} against E_g for the PLE results from the MBE grown InGaN QW and QB samples. The results follow a linear trend and the best-fit line to the data is:

$$E_{pl} = 2.980(30)E_g - 6.11(90) \qquad \textbf{Equation 8.3}$$

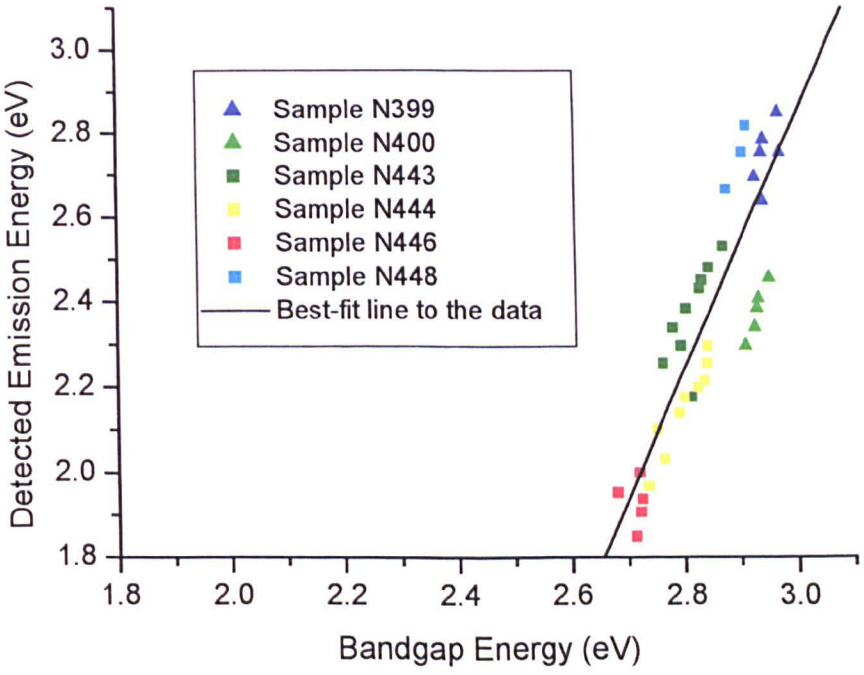

Figure 8.10: Detected emission energy, E_{pl}, against bandgap energy, E_g, for the MBE InGaN QWs and QBs; the QWs are indicated by (■) and the QBs by (▲).

8.4 Analysis of the PLE Results

For MOCVD grown InGaN epilayers, the bandgap energy was found to decrease with the detected emission energy for a given sample, as shown in Figures 8.2, 8.3 and 8.4. This indicates that the sample emission spectrum is inhomogeneously broadened. Furthermore, PLE spectra of epilayer samples with a low energy emission tail yields bandgap energies as low as that of the generally accepted

bandgap of InN ~1.89eV [4]. From the PLE measurements on sample Str115 at E_{pl}=1.55eV, a value of E_g ~1.99eV was obtained.

Using the fitting procedure outlined earlier, data were extracted from previous PLE measurements found in the literature on MOCVD grown InGaN QWs [5,6,7], and compared in Figure 8.11 to our results. The previous PLE measurements were taken on blue emitting InGaN samples with peak emission from ~2.65eV to 3.29eV, whereas the PLE results presented here extend from 2.85eV, in the violet, to 1.55eV, in the infra-red. These results are also compared with a best-fit line to the results of optical absorption measurements taken on MOCVD grown InGaN epilayers and QWs [8]. The line to the absorption data at low temperature is:

$$E_p = 1.453(26)E_g - 1.56(8) \qquad \textbf{Equation 8.4}$$

The PLE and absorption measurements both exhibit a linear relationship between the bandgap and detected emission energies. The PLE results compare fairly well with the absorption measurements and may extend the data range to lower energies. From the optical absorption spectrum of sample Str115, used in Figure 8.1, a bandgap energy of 2.67eV was determined by fitting equation 8.1 to the spectrum. Using equation 8.2 this corresponds to E_{pl}~2.45±(0.20)eV, which agrees within the error range with the experimental emission peak, E_p~2.32eV, as shown in Figure 8.1, and the calculated value of E_p~2.32±(0.15)eV from equation 8.4. This result shows that an optical absorption measurement is consistent with a PLE spectrum taken with the detection energy set to approximately that of the luminescence peak. An equation of best-fit for the combined data-set (PLE and absorption) is:

$$E_{pl} = 1.306(22)E_g - 1.10(6) \qquad \textbf{Equation 8.5}$$

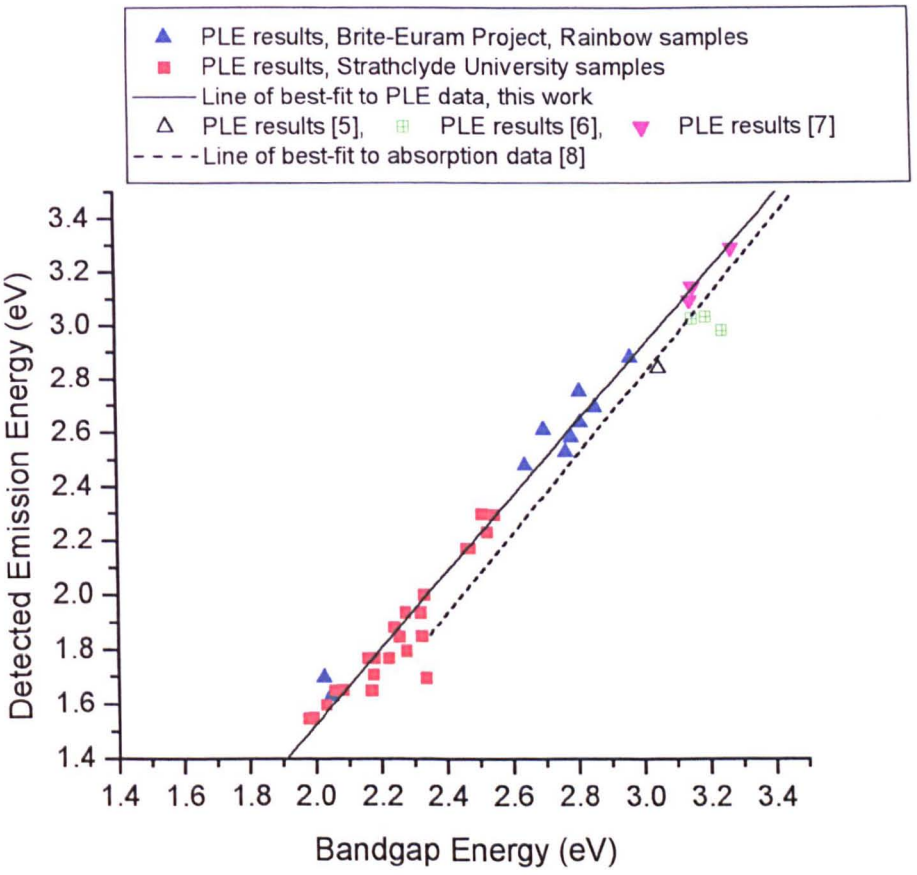

Figure 8.11: PLE results and data taken from previous PLE and optical absorption measurements on MOCVD grown InGaN epilayers and QWs.

From the results of the MBE InGaN samples, as shown in Figures 8.7, 8.8, 8.9 and 8.10, it was found that for the QWs and QBs, E_g obtained at different energies within the emission band of an individual sample decreases with detection energy. The results for both the QW and QB samples suggest that the emission spectrum is inhomogeneously broadened in both cases.

Independent low temperature (~0.35K) thermally detected optical absorption (TDOA) measurements taken on MBE samples N443, N444, N446 and N448

exhibit a linear relationship between the Stokes' shift and the emission energy [9]. A comparison with our results is shown in Figure 8.12. From the PLE results, a linear relationship between Stokes' shift and detected emission energy was observed and values of the Stokes' shift between 860meV and 100meV for detection energies in the range of 1.85eV and 2.82eV were obtained. For a given emission energy, the Stokes' shift from the TDOA measurements are ~10% greater than those from the PLE data on the same sample. This may be due to an underestimation in the bandgap energy determined from TDOA. The bandgap energy was calculated from the TDOA spectrum using a method based on the conservation of absorbed, reflected and transmitted light intensities, assuming that diffusion phenomena can be neglected [10]. In addition, strong thin-film interference in the TDOA spectra due to the flatness of the layers makes it difficult to determine precisely the bandgap energy of the sample.

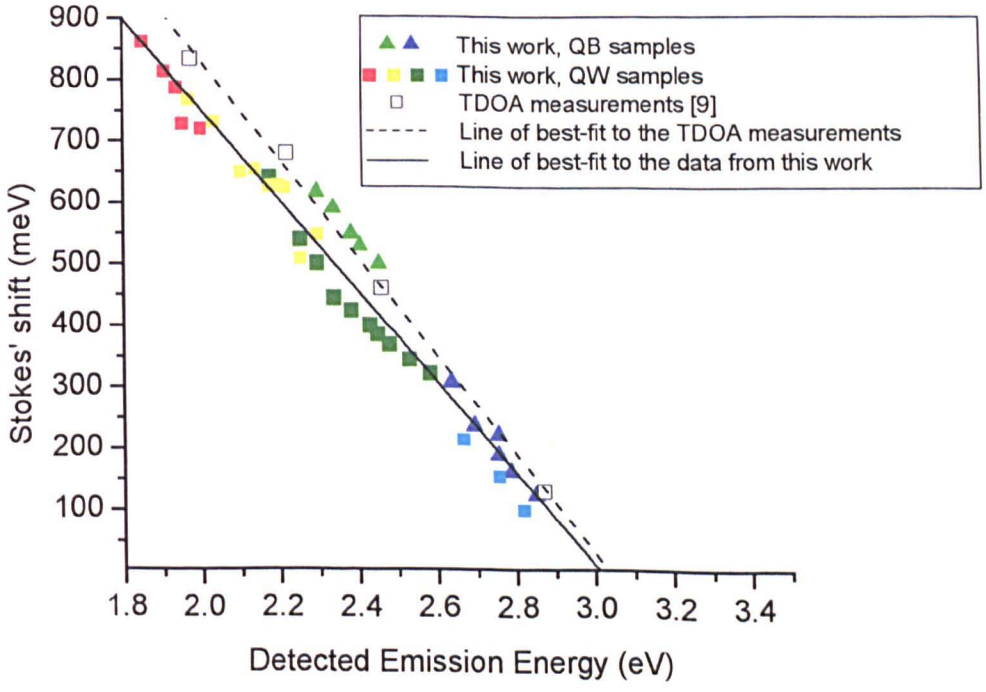

Figure 8.12: Stokes' shift against detected emission energy for the MBE InGaN QWs and QBs (key to QW and QB samples is shown in Figure 8.10).

Comparing a plot of Stokes' shift against detected emission energy from the PLE results on the MBE samples with the MOCVD samples, two very different linear trends are observed. Figure 8.13 presents a plot of the best-fit lines.

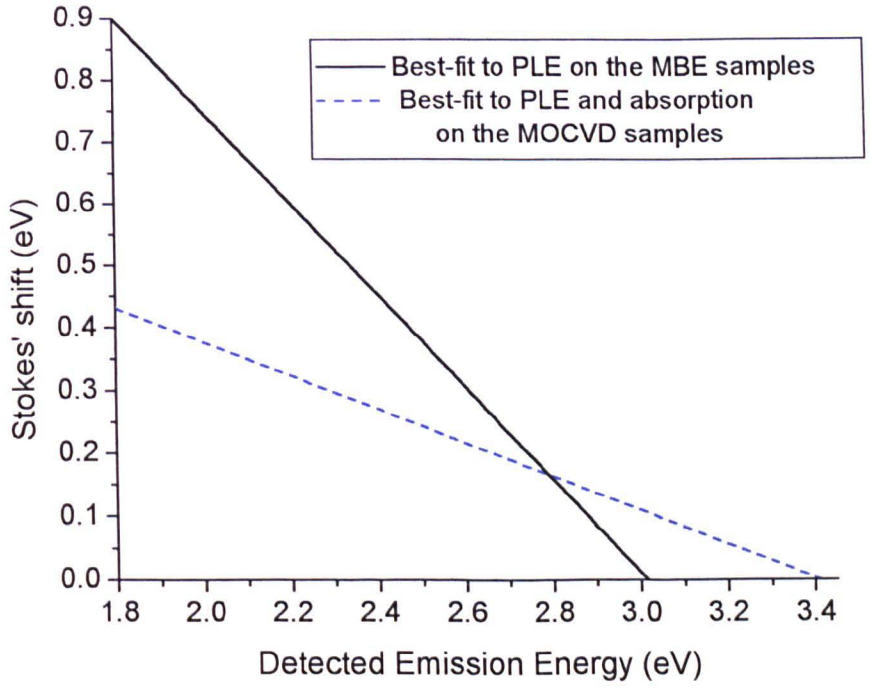

Figure 8.13: Best-fit lines for the Stokes' shift from PLE results on the MBE InGaN samples and the PLE and absorption measurements on the MOCVD InGaN samples.

As shown in Figure 8.13, at E_{pl}<2.80eV, the Stokes' shift from the MBE samples increases more rapidly with decreasing detection energy than for the MOCVD samples. At zero Stoke's shift, the linear trendline through the MOCVD results cuts the axis at emission energy ~3.41eV and the MBE results at emission energy ~3.02eV. The value from the MOCVD results is close to the emission energy of low temperature wurtzite GaN~3.5eV, as expected, but the MBE trendline is closer to the emission energy from low temperature cubic GaN ~ 3.15eV to 3.3eV [11].

However, XRD measurements and electron beam studies of the MBE samples indicate that the MBE, like the MOCVD samples, have wurtzite crystal structure [9].

An additional peak at ~3.5eV (not shown in the figures) is common in many of the PLE spectra. This peak is particularly prominent in the MBE samples, which have a thin nm-scale InGaN layer and suggests that the additional peak may be due to carriers being excited in the GaN layer, which then relax into the InGaN layer and cause an increase in the emission intensity [7].

Strong localisation effects attributed to InN-rich QDs combined with accompanying strain induced piezoelectric fields have been presented to explain the linear trend in the optical absorption measurements shown in Figure 8.11 [3,12]. This argument may also be extended to explain the PLE results. The effects of localisation and piezoelectric fields as discussed previously in Chapter 4, Section 4.5.1, may result in inhomogeneous broadening of the emission spectrum. Furthermore, the linear relationship between E_g and E_{pl}, determined in both the MOCVD and MBE samples, and the trendline plotted in the MBE results, irrespective of whether it is a QW or QB sample, indicates that the excitation/emission cycle of InGaN is dependent on some form of localisation common in all the samples. The different trendlines plotted for the MOCVD and MBE results and the large difference in the Stokes' shifts obtained are likely to be related to the different growth techniques used and the resulting difference in the strain induced piezoelectric fields.

8.5 Summary

In this chapter, PLE measurements from two different sets of MOCVD grown InGaN epilayer samples and a set of MBE grown QW and QB InGaN samples are presented and discussed. It was found that for a given sample the bandgap energy determined from the PLE spectrum decreases linearly with detected emission energy. This indicates that the sample emission spectrum is inhomogeneously broadened.

From the PLE measurements on the MOCVD samples, the lowest bandgap energy obtained was ~1.99eV, close to the generally accepted value for the bandgap of pure InN ~1.89eV [4]. The linear trend of E_g against E_{pl} plotted for the MOCVD results agrees, within the error range, to previous optical absorption measurements and the data range covered by the absorption measurements therefore extended to lower energies by the PLE results.

Stokes' shift values, calculated using the PLE data from the MBE samples, were approximately 10% smaller than those from independent measurements taken by TDOA. On comparing the Stokes' shifts from the MBE samples with those from the MOCVD samples, two very different linear trendlines were obtained. At E_{pl}<2.80eV, the MBE Stokes' shift becomes larger and increases more rapidly with decreasing detection energy than that from the MOCVD samples.

8.6 References

[1] S. Nakamura and G. Fasol, *The Blue Laser Diode*, Springer, Berlin (1997).

[2] K. P. O'Donnell, R. W. Martin, S. Pereira, A. Bangura, M. E. White, W. Van der Stricht and K. Jacobs, phys. stat. sol. (b) **216**, 141 (1999).

[3] R. W. Martin, P. G. Middleton, K. P. O'Donnell and W. Van der Stricht, Appl. Phys. Lett. **74**, 263 (1999).

[4] B. Gil and M. Leroux, *Properties of Indium Nitride*, EMIS Datareview 23 (1999).

[5] H. C. Yang, P. F. Kuo, T. Y. Lin, Y. F. Chen, K. H. Chen and J.-I. Chyi, Appl. Phys. Lett. **76**, 3712 (2000).

[6] Y.-H. Kwon, G. H. Gainer, S. Bidnyk, Y. H. Cho, J. J. Song, M. Hanson and S. P. Denbarrs, Appl. Phys. Lett. **75**, 2545 (1999).

[7] J. A. Davidson, P. Dawson, T. Wang, T. Sugahara, J. W. Orton and S. Sakai, Semicond. Sci. Technol. **15**, 497 (2000).

[8] K. P. O'Donnell, R. W. Martin, C. Trager-Cowan, M. E. White, K. Esona, C. Deatcher, P. G. Middleton, K. Jacobs, W. Van der Stricht, C. Merlet, B. Gil, A. Vantomme and J. F. W. Mosselmans, Mat. Sci. Eng. B **82**, 194 (2001).

[9] B. Damilano, N. Grandjean, J. Massies, S. Dalmasso, J. L. Reverchon, M. Calligaro, J. Y. Duboz, L. Siozade and J. Leymarie, phys. stat. sol. (a) **180**, 363 (2000).

[10] L. Siozade, P. Disseix, A. Vasson, J. Leymarie, B. Damilano, N. Grandjean and J. Massies, phys. stat. sol. (a) **183**, 139 (2001).

[11] J. H. Edgar, *Properties of Group III Nitrides*, No. 11 EMIS Datareview, INSPEC, London (1994).

[12] K. P. O'Donnell, R. W. Martin and P. G. Middleton, Phys. Rev. Lett. **82**, 237 (1999).

CHAPTER 9: CONCLUSIONS AND SUGGESTIONS FOR FUTURE WORK

9.1 Conclusions

This thesis presents work on the optical properties, composition and local structure of InGaN using experimental techniques not commonly applied to III-nitrides.

The thesis was presented in nine Chapters. In Chapter 1, the history of III-nitrides and their applications were given and the properties of InGaN introduced. Chapter 2 outlined the growth and structure of InGaN and presented the main theories currently proposed to explain InGaN luminescence. In Chapter 3, the experimental procedures to be used in this investigation were described. Photoluminescence (PL) mapping of InGaN epilayers and the temperature dependence of the PL spectrum were discussed in Chapter 4. In Chapter 5, the indium nitride content determined from several composition measurements on epilayers was related to their optical properties. Confocal microscopy (CM) images of InGaN epilayers, QWs and QBs were presented in Chapter 6, and in Chapter 7 local structure parameters derived from extended X-ray absorption fine structure (EXAFS) measurements on InGaN epilayers and an InGaN QB sample were given. Finally, Chapter 8 showed the results from photoluminescence excitation (PLE) spectroscopy measurements on MOCVD and MBE grown InGaN epilayers, QWs and QBs.

From PL spectroscopy of InGaN epilayers a number of experimental results were determined (Chapter 4). It was found that the linewidth of the PL spectrum generally

broadens with a decrease in the peak emission energy. PL mapping on a unique piece of InGaN emitting in the red and near infra-red revealed that the luminescence intensity lowers with decreasing peak emission energy. Each of these results could be explained by a change in the indium nitride content in the material. Macroscopically inhomogeneous emission shown in the PL maps can be identified with a variation of the indium incorporation rate as a result of a temperature gradient across the sample formed during growth.

Temperature dependence of the PL of the epilayer samples showed for one sample a decrease in the peak emission energy with increasing temperature, consistent with a reduction in the bandgap energy [1]. For this sample, linewidth broadening of the PL spectrum with increasing temperature was attributed to phonon broadening effects. An 'S'-shape temperature dependence of the peak emission energy as a function of temperature was obtained from a second epilayer sample. This result could not be fully explained by a reduction in the bandgap energy of the material.

For both samples it was found that the emission intensity decreases with increasing temperature. This reduction is generally attributed to thermal quenching of the luminescence by non-radiative sites in the material, which become active at higher temperatures [2]. Activation energies determined from a linear fit to an Arrhenius plot of the intensity data were between 30meV and 60meV, consistent with those reported in the literature for InGaN [3,4].

Composition analysis of the InGaN epilayers (Chapter 5) taken using three different experimental techniques: RBS, EPMA and EXAFS, found that the indium nitride fraction varies linearly with the PL peak emission energy of the sample. The results from different composition analysis techniques agree fairly well with each other and a best-fit linear trendline was plotted for the combined dataset. This best-fit line was also shown to agree with similar published results from SIMS and XRD measurements, where the latter have been corrected for the effects of strain in the material [5,6]. The composition values presented here extend beyond those found in the literature at the time of writing, with an upper limit for the indium nitride content, x, of ~0.40. The experimental data did not follow the bowing curve calculated theoretically.

Confocal microscopy of InGaN epilayer, QW and QB samples (Chapter 6) revealed that InGaN luminescence usually segregates into bright and dark spots, ~1μm in diameter (comparable with the resolution limit of the microscope). The temperature dependence of the bright spots in the fluorescence images was similar to that from the temperature dependence of the PL spectrum (Chapter 4). A crude form of spectroscopic imaging on the fluorescent spots, using 10nm bandpass filters in the fluorescence channel of the CM, showed that the intensity of the image changes depending on the bandpass filter used, as expected. Although some bright spots appeared at a specific wavelength but not others, the majority of bright spots were present in all the fluorescence images from a particular region of the sample. PL spectra taken from bright and dark spots varied in intensity but showed a consistent PL peak emission energy value.

InGaN local structure parameters were derived from EXAFS measurements at the indium K-edge for a set of InGaN epilayers and an InGaN QB sample (Chapter 7). The In-N_1 interatomic spacing in the epilayers was found to be ~2.11(2)Å, which is similar to that for a pure InN sample used as a calibration standard, ~2.16(2)Å and also to the In-N_1 value determined from the literature, ~2.16Å [7]. However, the experimental values obtained were higher than those predicted by Vegard's Law and varied little over the composition range. The interatomic spacing of the first metal shell was closer to the Ga-Ga separation in bulk GaN than the In-In separation in bulk InN. The InGaN QB showed a similar In-N_1 separation to the epilayers. Although the epilayers comprised of a single-phase InGaN alloy, the InGaN QB exhibited two components, one InN-like and another that resembles a gallium rich InGaN alloy. From the parameters derived, the indium nitride content, x, in the gallium rich InGaN alloy was estimated to be ~0.06 and the volume of material which is InN-like ~4%.

Photoluminescence excitation (PLE) spectroscopy of MOCVD InGaN epilayers (Chapter 8) showed that the bandgap energy, E_g, of the material varies linearly with the detected emission energy, E_{pl}. These results were consistent with optical absorption measurements on MOCVD grown InGaN epilayers and QWs. From PLE measurements of MBE grown InGaN QWs and QBs, a linear relationship between bandgap energy and detected emission energy was also observed. Stokes' shifts calculated from the MBE results were ~10% smaller than those obtained by independent TDOA measurements taken on some of the same samples. Comparing the best-fit for Stokes' shift against detected emission energy of the MOCVD and

MBE samples, two very different linear trendlines were produced. At E_{pl}<2.80eV, Stokes' shift from the MBE samples increases more rapidly with decreasing detection energy than for the MOCVD samples.

As discussed in Chapter 2, the emission mechanisms of InGaN are not yet fully understood. There are two main theories currently proposed to describe the influences acting on the exciton recombination process in InGaN. These are localisation effects and the effects of piezoelectric and spontaneous polarisation fields. By analysing and comparing the result presented in this thesis, a more detailed description of the emission mechanisms in InGaN may be deduced.

In Figure 5.6, it was shown that the peak emission energy of InGaN varies linearly with the indium nitride fraction. This demonstrates that the emission mechanism is dependent in some way on InN. Moreover, as the linear relationship is consistent over many different samples, the emission is dependent on a source common to all InGaN. The general linewidth broadening of the PL spectrum with decreasing peak emission energy, as shown in Figure 4.2, suggests that this emission mechanism may also determine the shape of the PL spectrum. It can be concluded from the results that localisation effects are present in these samples as strong luminescence from sample InGaN 331 and InGaN 336 could be obtained, despite the poor crystallinity of the material. Furthermore, emission in the red and near infra-red from sample InGaN 336, as shown in the PL maps in Figures 4.6 and 4.7, indicate that localisation occurs in sites which are either InN-rich or are heavily affected by

strain induced piezoelectric fields. Equally, emission could be due to a combined factor of both.

As discussed in Chapter 4, the 'S'-shape temperature dependence of PL from an epilayer sample, shown in Figure 4.11 and 4.13, can only be fully explained by considering the effects of carrier localisation in the material. This emission behaviour, first observed by Cho et al., was attributed to the effects of inhomogeneity and carrier localisation [3]. The 'S'-shape effect was only seen in one of the two samples tested. The other sample has higher peak emission energy and from the linear relationship in Figure 5.6, would have a lower indium nitride content. The effects of localisation must therefore become greater with an increase in the indium nitride content.

Further investigations on the optical properties of InGaN using confocal microscopy showed that luminescence segregation occurs into bright and dark spots, ~1μm in diameter. The presence of the same luminescent spots in the images when taken using a variety of different bandpass filters indicates that the origin of InGaN luminescence is smaller than the order of 1μm. These results demonstrate that segregation effects do occur in InGaN on the μm-scale. It can also be inferred that segregation effects occur on the sub μm-scale and that the emission mechanisms in InGaN may be a product of segregation in the material.

A linear relationship between E_g and E_{pl}, obtained from the PLE results taken on an individual sample, shows that the emission spectrum of the sample is

inhomogeneously broadened. As the relationships between E_g and E_{pl} for all of the samples were found to follow a given linear trend, seen in Figures 8.4 and 8.10, this again indicates that localisation of the exciton occurs at a source common to all of the samples. The difference in the linear trendline of the MOCVD and MBE samples may be due to the different growth techniques and the subsequent different strain induced piezoelectric fields. The different piezoelectric fields would explain the separate linear relationships obtained and the difference in the Stokes' shifts but not the actual linear trendline.

The local structure parameters derived from EXAFS measurements on the InGaN QB showed that InGaN may exist as a two-phase mixture of components, one of which is InN-like. As InGaN is thermodynamically unstable [8], this two-phase mixture may be due phase segregation effects in InGaN. Although the InGaN epilayers only exhibit a single phase InGaN alloy, the InN-like phase may still exist in these samples but not in sufficient quantity to be determined as a separate entity during modelling of the EXAFS.

On consideration of the accumulated results presented, there is strong evidence to suggest that InGaN luminescence may be related to the combined effects of localisation in InN-rich QDs, formed as a result of nanometric phase segregation, accompanied by strain-induced piezoelectric fields [9,10].

These effects can explain each of the conclusions drawn from the experimental results. InN-rich QDs would provide a source of localisation, common in all InGaN

material, as was demonstrated on analysis of the PL, composition and PLE results. The size and distribution of the InN-rich QDs would vary with the indium nitride molar fraction and can describe the effects of the PL results in Chapter 4 and the linear dependence of PL peak emission energy on the composition measurement as shown in Chapter 5. On increasing the InN molar fraction, the diameter of the InN-rich QDs would be expected to increase. As a larger QD diameter would result in a reduction in the quantum confinement energy, then a shift toward red emission would be obtained in InGaN with higher indium nitride fractions. Furthermore, increasing the indium nitride content would also provide a wider distribution of dot sizes, and, as the emission energy is dependent on the size of the dot, this leads to inhomogeneous linewidth broadening with decreasing peak emission energy [9,10].

The epilayer sample that did not exhibit 'S'-shape temperature dependence has a lower indium nitride content and will subsequently have a lower number of InN-rich QDs with a smaller diameter, therefore the influence of localisation effects on the PL spectrum of this sample would be smaller.

InN-rich QDs are estimated to be on the order of ~1nm, consistent with the sub μm-scale estimated for the origin of InGaN luminescence from CM results. If clustered together, these InN-rich QDs may produce the appearance of luminescence segregation when viewed on the μm-resolution of the CM.

The QB sample was shown to be a two-phase mixture, one InN-like which occupies only 4% of the volume of the material and the remainder a gallium rich InGaN alloy

with an indium nitride content of ~0.06. This agrees completely with the idea of nm-scale InN-rich QDs embedded in a gallium rich InGaN matrix.

However, accompanying strain induced piezoelectric fields acting in the material are also evident from the different linear trendlines produced for the E_g against E_{pl} plots for the MOCVD and MBE samples and from the red and near infra-red luminescence obtained from InGaN 336, well below the generally accepted bandgap of InN ~1.89eV [11].

Effects of strain-induced piezoelectric fields alone cannot fully explain the results obtained in this thesis. Moreover, InGaN alloy composition fluctuations could not explain the two-phase mixture of the QB material. It would also be very difficult to explain the consistent sets of results and relationships determined throughout this work, from many different samples investigated, by a random quantity such as InGaN composition fluctuations. The results clearly indicate that a single source common in all InGaN is responsible for localisation in the material.

It can therefore be concluded that InGaN luminescence may be related to its nanostructure as a result of exciton localisation in nano-scale InN-rich QDs and that the optical properties of InGaN may also be influenced by the effects of strain induced piezoelectric fields in the material.

9.2 Suggestions for Future Work

The data range of the results presented in this thesis could be extended by looking at InGaN samples with a higher indium nitride content, $x \geq 0.4$. However, due to the difficulty of incorporating indium into the material at the high growth temperature required to produce InGaN, such samples are rather hard to obtain. The recent arrival of an EPMA facility at Strathclyde University has provided an opportunity for further investigations on the composition and optical properties of InGaN. The imaging and cathodoluminescence facilities on the EPMA allow for optical, structural and compositional analyses to be carried out simultaneously.

There is a wealth of information on the luminescence properties of InGaN contained in each CM image but at present no data evaluation system is available to make full use of this information. As part of the VISION project at Strathclyde University, the Semiconductor research group has access to a Silicon Graphics, Onyx II, computer. This facility could be used to produce large scale, high definition and fully interactive data visualisations of the CM images. These visualisations would make it possible to generate a 3-D like object formed from a sequence of 2-D images with temperature, bandpass filter or time as the third dimension. Using the Virtual Environment Laboratory (VEL) or displaying remotely on a high specification workstation, it would then be possible to study these images by appearing to travel through them. By selecting a single fluorescent spot on a given image, statistical analysis of the fluorescence intensity or even the size of the fluorescent region could be analysed in great detail.

EXAFS on QW samples would also be of interest to see if they exhibit the single or two-phase mixture, as obtained for the epilayer and QB samples respectively. In addition to EXAFS, techniques such as XEOL could be used where X-ray absorption is monitored by detecting optical luminescence from the sample. This may prove useful as unlike EXAFS, which reflects the average local structure, the XEOL yield represents the luminescent sites and its immediate surroundings [12].

PLE measurements carried out with E_{pl}<1.55eV would determine whether the corresponding E_g value reaches a limit at 1.89eV, the generally accepted bandgap of InN, or continues to decrease. This has already been attempted on sample Str115 with E_{pl} set to ~1.45eV, however, the PLE spectrum was not strong enough in order to unambiguously fit the sigmoidal function.

By compiling more information on the properties of InGaN, perhaps the origin of InGaN luminescence and the physics of this significant semiconductor material will become more apparent.

9.3 References

[1] K. P. O'Donnell and X. Chen, Appl. Phys. Lett. **58**, 2924 (1991).

[2] I. A. Buyanova, W. M. Chen, G. Pozina, B. Monemar, W.-X. Ni and G. V. Hansson, Appl. Phys. Lett. **71**, 3676 (1997).

[3] Y.-H. Cho, G. H. Gainer, A. J. Fischer, J. J. Song, S. Keller, U. K. Mishra and S. P. DenBaars, Appl. Phys. Lett. **73**, 1370 (1998).

[4] H. P. D. Schenk, M. Leroux and P. de Mierry, J. Appl. Phys. **88**, 1525 (2000).

[5] J. Wagner, A. Ramakrishnan, D. Behr, M. Maier, N. Herres, M. Kunzer, H. Obloh and K.-H. Bachem, MRS Internet J. Nitride Semicond. Res. **4S1**, G2.8 (1999).

[6] T. Takeuchi, H. Takeuchi, S. Sota, H. Sakai, H. Amano and I. Akasaki, Jpn. J. Appl. Phys. **36**, L177 (1997).

[7] V. A. Tyagai, A. M. Evstigneev, A. N. Krasiko, A. F. Malakhov and V. Ya, Fiz. Tekh. Poluprovodn. **11**, 2142 (1977).

[8] I.-H. Ho and G. B. Stringfellow, Appl. Phys. Lett. **69**, 2701 (1998).

[9] R. W. Martin, P. G. Middleton, K. P. O'Donnell and W. Van der Stricht, Appl. Phys. Lett. **74**, 263 (1999).

[10] K. P. O'Donnell, R. W. Martin and P. G. Middleton, Phys. Rev. Lett. **82**, 237 (1999).

[11] B. Gil and M. Leroux, *Properties of Indium Nitride*, EMIS Datareview 23 (1999).

[12] I. Coulthard and T. K. Sham, Solid State Communications **110**, 203 (1999).

APPENDIX A: InGaN SAMPLE DETAILS

The MOCVD grown InGaN samples under investigation include epilayers and QWs obtained from five different sources: the University of Ghent, Belgium; the University of Strathclyde, UK; Aixtron AG, Germany; Thomsom-CSF LCR, France and Nichia Chemical Industries, Ltd. Japan. The MBE grown samples include QWs and QBs from CNRS, Valbonne, France. Details of each sample are given in Tables A.1 to A.5.

A.1 MOCVD InGaN SAMPLES

A.1.1 MOCVD InGaN from the University of Ghent

The InGaN samples from the University of Ghent were grown in a Thomas Swan and Co., Ltd rotating-disc reactor. A description of the growth reactor and modifications made to the system can be found in reference [1]. The samples investigated were all InGaN/GaN bilayers grown onto a sapphire substrate. The nominal growth temperature and layer thickness of each sample are presented in Table A.1. Unfortunately, no details are available for sample InGaN 131.

Sample Reference Number	GaN growth temperature (°C)	GaN layer thickness (nm)	InGaN growth temperature (°C)	InGaN layer thickness (nm)
85	1050	2000	850	250-300
131	----	----	----	----
331	1080	2200	780	270
336	1080	2200	780	230

Table A.1: Details of the MOCVD samples from the University of Ghent.

A.1.2 MOCVD InGaN from the University of Strathclyde

InGaN samples were grown at the University of Strathclyde by Dr Ian Watson using an Aixtron 200/4 RF-S reactor. The samples investigated were all InGaN epilayers deposited on a GaN buffer layer on a GaN nucleation layer grown onto (0001) sapphire substrates. The growth temperatures for the nucleation, buffer and InGaN layers were 540°C, 1140°C and 760°C respectively. The thickness of each layer was estimated using the material growth rate as determined from optical reflectometry measurements. Independent Rutherford backscattering spectrometry (RBS) measurements taken on the samples verified the layer thickness [2]. Structures of each sample are presented in Table A.2.

Sample Reference Number	GaN nucleation layer thickness (nm)	GaN buffer layer thickness (nm)	InGaN layer thickness (nm)
Str59	20	1000	220
Str115	20	1100	240
Str116	20	1100	60
Str117	20	1000	120

Table A.2: Details of the MOCVD samples from the University of Strathclyde.

A.1.3 MOCVD InGaN from Aixtron AG and Thomson-CSF LCR

InGaN samples were grown at Aixtron AG, Germany and Thomson-CSF LCR, France as part of the Brite-Euram project, Rainbow. The samples listed in Table A.3 with a reference number pre-fixed by an 'S' were grown by Aixtron AG, in a AIX2000/2400HT reactor; the other material was grown by Thomson-CSF LCR in a home-made MOCVD reactor. All samples were InGaN epilayers grown at temperatures of approximately 800°C. Further details of the structures are outlined in Table A.3.

Sample Reference Number	GaN buffer layer thickness (nm)	InGaN layer thickness (nm)
S101	>1000	120
S201	>1000	350
AEC53	650	75

Table A.3: Details of the MOCVD samples grown as part of the Brite-Euram Project, Rainbow.

A.1.4 MOCVD InGaN from Nichia

The InGaN sample from Nichia Chemical Industries, Ltd was grown using the two-flow MOCVD method [3]. The sample was grown as a SQW structure for use in the fabrication of LEDs [4]. The structure of the sample is as shown in Figure A.1.

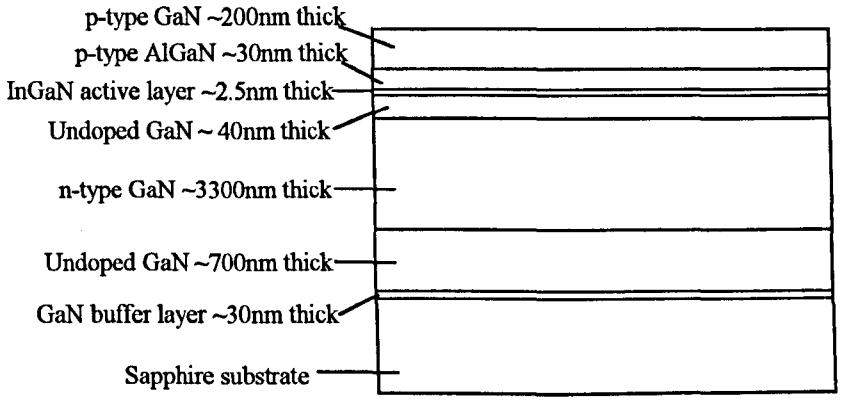

Figure A.1: Structure of InGaN SQW sample from Nichia Chemical Industries, Ltd. (diagram not drawn to scale).

A.2.1 MBE InGaN SAMPLES

MBE InGaN samples were grown at CNRS, Valbonne, France in a Riber 32P reactor, adapted to use NH_3 as the nitrogen source and equipped with RHEED and laser reflectometry facilities. For both the QW and QB samples, an InGaN layer was deposited on a GaN buffer layer grown on top of a GaN nucleation layer on a (0001) sapphire substrate. The sapphire substrate was metallized with molybdenum and mounted in an In-free molybdenum holder to allow the sample to heat effectively during MBE growth. The GaN nucleation layer was grown at 500°C and the GaN buffer and QW layers at approximately 800°C to 820°C. The InGaN layer was grown at 530°C for the QW samples and 550°C for the QBs. The QB GaN capping layer was grown at 800°C.

Growth conditions for QW and QB samples were similar, with the exception of the InGaN growth temperature and the ammonia flux. The ammonia flux was increased from 50sccm, used during QB growth, to 200sccm for the QW growth. This is because the presence of ammonia, or hydrogen radicals at the growth surface is assumed to delay the 2D-3D transition by increasing the surface free energy [5]. The 2D-3D growth transition in the QB was observed using in-situ RHEED and the growth rate of the layers determined from reflectivity oscillations. Sample structures are presented in Tables A.4 and A.5.

Sample Reference Number	GaN nucleation layer thickness (nm)	GaN buffer layer thickness (nm)	QW GaN layer thickness (nm)	QW InGaN layer thickness (nm)	Number of QW layers
N443	25	4700	14.0	3.2	10
N444	25	10500	14.0	4.0	5
N446	25	2400	13.5	5.5	7
N448	25	2900	5.0	1.5	10

Table A.4: Details of the MBE QW samples from CNRS, Valbonne.

Sample Reference Number	GaN nucleation layer thickness (nm)	GaN buffer layer thickness (nm)	Second GaN layer thickness (nm)	InGaN layer thickness (nm)	GaN capping layer thickness (nm)
N399	25	4500	200	2.5	40
N400	25	4500	200	3.5	40
N401	25	4500	----	3.1	Uncapped

Table A.5: Details of the MBE QB samples from CNRS, Valbonne.

A.3 References

[1] Wim Van der Stricht, PhD Thesis, University of Ghent, *Development of group III nitride technology for the realisation of light emitting diodes*, unpublished (1998-1999).

[2] Private communication, Sergio Pereira, Universidade de Aveiro, Portugal.

[3] S. Nakamura and G. Fasol, *The Blue Laser Diode*, Springer, Berlin (1997).

[4] T. Mukai, H. Narimatsu and S. Nakamura, Jpn. J. Appl. Phys. **37**, L479 (1998).

[5] B. Damilano, N. Grandjean, J. Massies, L. Siozade and J. Leymarie, Appl. Phys. Lett. **77**, 1268 (2000).

APPENDIX B: CORRECTION FACTORS APPLIED TO THE PHOTOLUMINESCENCE AND PHOTOLUMINESCENCE EXCITATION SPECTRA

The photoluminescence (PL) and photoluminescence excitation (PLE) spectra presented in this thesis have been corrected for the variation of monochromator throughput and detector response as a function of light wavelength.

B.1 Spectral Correction of the PL Results

The emission spectrum from a known source was taken under the same experimental conditions as the PL spectrum to provide a reference to determine the correction factor for the PL experimental set-up, shown in Figure 3.1. The reference source was a tungsten lamp which, under closely defined operating conditions, has a determined spectral radiance for a given wavelength, $380\text{nm} \leq \lambda \leq 800\text{nm}$, originally measured by the National Physical Laboratory (NPL). However, as the wavelength range given by the NPL datapoints does not cover the entire range of the experimental PL results, a fit of a blackbody emission spectrum to the NPL data was generated in order to extend the range of the calibration. Taking into account the variation of the tungsten emissivity with wavelength and temperature, $\varepsilon(\lambda, T)$, the emission spectrum of the lamp can be described by the equation:

$$\text{Lamp radiance} = \text{emissivity of tungsten} \times \text{radiance of blackbody (Planck's Law)}$$

$$I(\lambda, T) \propto \varepsilon(\lambda,T) \times \frac{1}{\lambda^5\left(\exp^{\frac{hc}{kT\lambda}} - 1\right)} \qquad \textbf{Equation B.1}$$

where h is Planck's constant, c the speed of light, k Boltzmann's constant, λ the wavelength and T the effective temperature of the lamp filament.

As the temperature of the lamp filament is not known, the emissivity of tungsten, given for discrete values of λ and T [1], was fitted to a polynomial equation to determine $\varepsilon(\lambda)$ for an arbitrary value of T [2]. By substituting this function for $\varepsilon(\lambda, T)$ into equation B.1, keeping T as a variable, the spectral radiance for a given wavelength could be calculated and by applying the method of least squares the temperature value adjusted until a fit to the NPL data was obtained. As shown in Figure B.1 the best fit was produced for a temperature of 2755K. Spectral radiance values could then be generated over the required wavelength range.

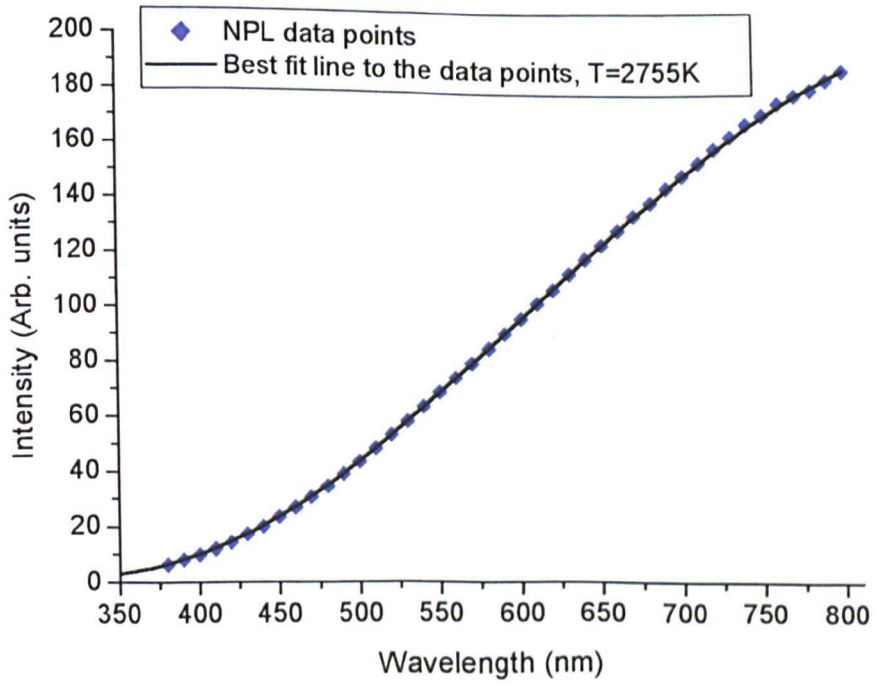

Figure B.1: Showing the best fit line to the NPL datapoints, obtained for T=2755K.

The experimentally obtained tungsten lamp spectrum recorded using the PL set-up, $I_{exp}(\lambda)$, is dependent on lamp radiance, $I(\lambda)$, and the light response of the monochromator and detector, $G(\lambda)$;

$$I_{exp}(\lambda) \propto I(\lambda) \times G(\lambda) \qquad \textbf{Equation B.2}$$

To determine $G(\lambda)$, the experimentally obtained spectrum is divided by the spectrum calculated using equation B.1 for T=2755K.

The system response curve for the PL experimental set-up as a function of wavelength, when using the McPherson 0.67m monochromator with a diffraction grating blazed for the visible wavelength range and the Thorn EMI Gencom Inc 3365 cooled photomultiplier tube as the detector is shown in Figure B.2. The system response curve for the McPherson 0.67m monochromator with the diffraction grating blazed for the infra-red wavelength range and the Edinburgh Instruments EI germanium detector is shown in Figure B.3. The PL spectra were multiplied by $G(\lambda)$ for the corresponding experimental set-up to produce the corrected PL spectrum.

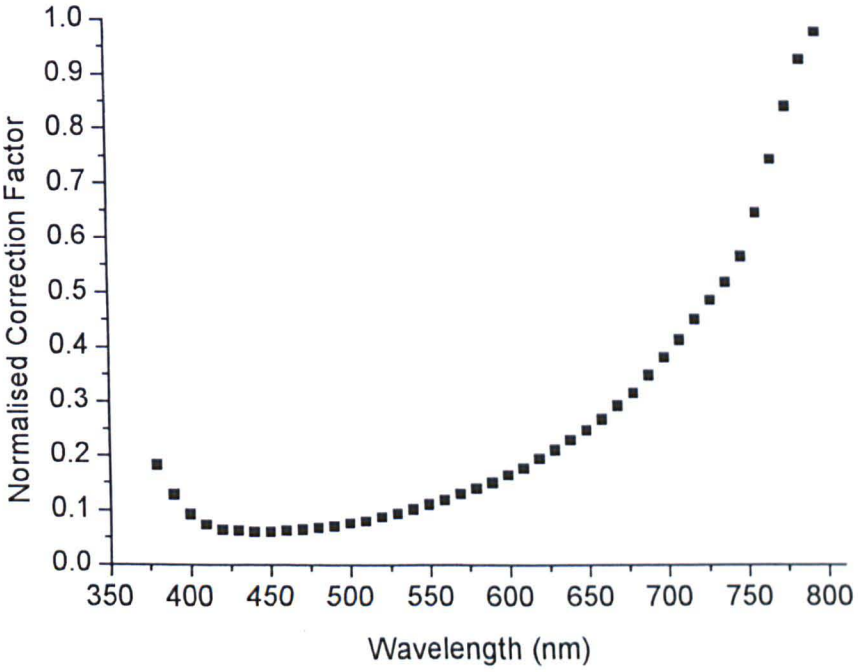

Figure B.2: Correction factor for the McPherson 0.67m monochromator with the visible grating and the Thorn EMI Gencom Inc 3365 cooled PMT.

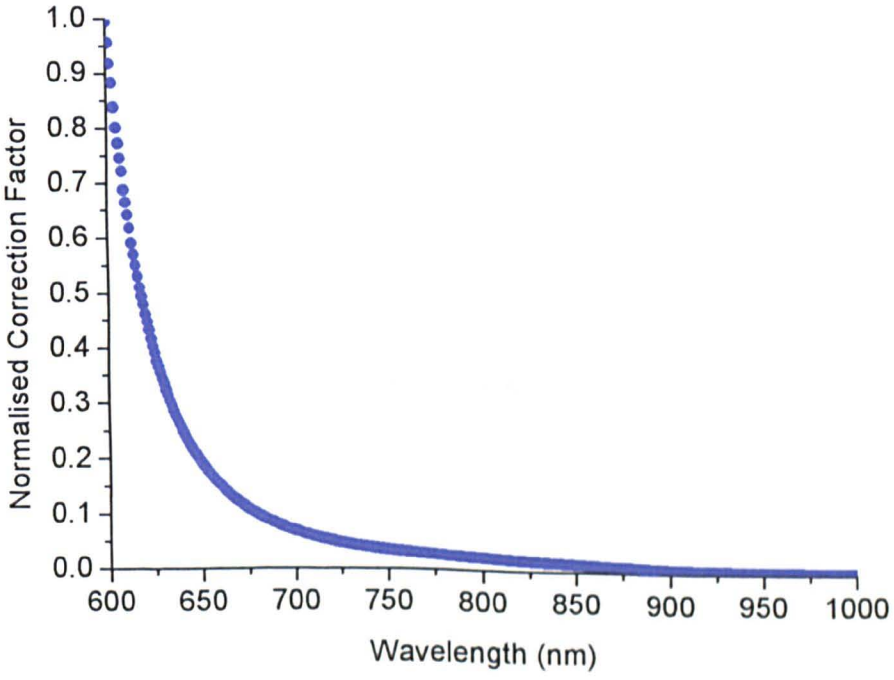

Figure B.3: Correction factor for the McPherson 0.67m monochromator with the infra-red grating and Edinburgh Instruments EI germanium detector.

B.2 Spectral Correction of the PLE Results

The PLE spectra were corrected for the spectral variation of the xenon lamp and the throughput of the excitation monochromator, shown in Figure 3.3. The emission spectrum of the combination was measured using a calibrated photodiode, RS 303-674 and corrected by using the known response curve of the photodiode, indicated in Figure B.4 [3]. Correction of the PLE spectra was made by dividing through by the corrected emission spectrum, shown in Figure B.5.

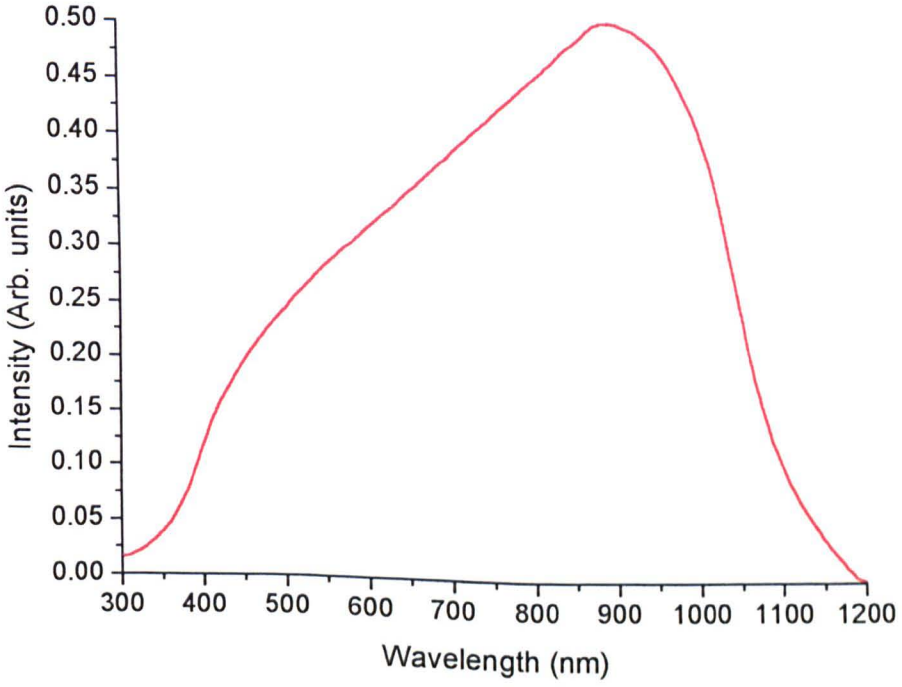

Figure B.4: Response curve of the photodiode RS 303-674 as given by the suppliers.

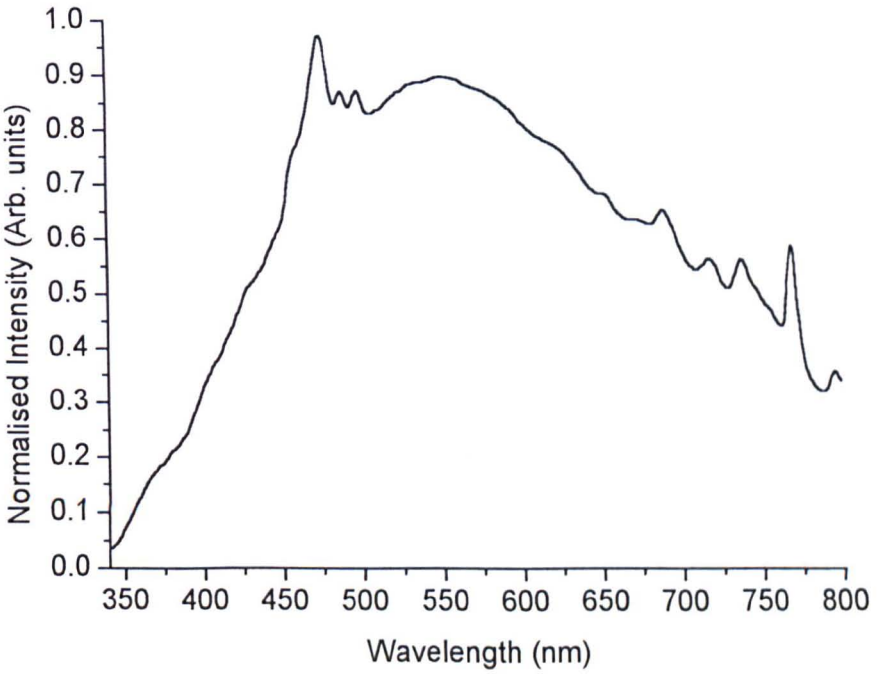

Figure B.5: Output of the xenon lamp and the excitation monochromator as a function of wavelength.

B.3 References

[1] Handbook of Chemistry and Physics, 63rd Edition, CRC Press, E-373 (1982).

[2] Private communication, P. R. Edwards, Calibration Fitting Program (2001).

[3] http://rswww.com, photodiode RS 303-674 technical specifications.

APPENDIX C: LIST OF PUBLICATIONS

M. E. White, K. P. O'Donnell, R. W. Martin, S. Pereira, C. J. Deatcher and I. M. Watson, *Photoluminescence Excitation Spectroscopy of InGaN Epilayers*, Mat. Sci. Eng. B **93**, 147 (2002).

K. P. O'Donnell, M. E. White, S. Pereira, J. F. W. Mosselmans, N. Grandjean, B. Damilano and J. Massies, *In K-edge Extended X-ray Absorption Fine Structure of InGaN Epilayers and Quantum Boxes*, Mat. Sci. Eng. B **93**, 150 (2002).

S. Pereira, M. R. Correia, E. Pereira, K. P. O'Donnell, R. W. Martin, M. E. White, E. Alves, A. D. Sequeira and N. Franco, *Splitting of X-ray Diffraction and Photoluminescence Peaks in InGaN/GaN layers*, Mat. Sci. Eng. B **93**, 163 (2002).

M. E. White, K. P. O'Donnell, R. W. Martin, C. J. Deatcher, B. Damilano, N. Grandjean and J. Massies, *Photoluminescence Excitation Spectroscopy of MBE Grown InGaN Quantum Wells and Quantum Boxes*, phys. stat. sol. (b) **228**, 129 (2001).

K. P. O'Donnell, J. F. W. Mosselmans, R. W. Martin, S. Pereira and M. E. White, *Structural Analysis of InGaN Epilayers*, J. Phys.: Condens. Matter. **13**, 6977 (2001).

K. P. O'Donnell, R. W. Martin, M. E. White, M. J. Tobin, J. F. W. Mosselmans, I. M. Watson, B. Damilano and N. Grandjean, *Luminescence and Structural*

Properties of InGaN Epilayer, Quantum Well and Quantum Dot Samples Using Synchrotron Excitation, Mat. Res. Soc. Symp. **639**, G9.11.1 (2001).

K. P. O'Donnell, R. W. Martin, C. Trager-Cowan, M. E. White, K. Esona, C. Deatcher, P. G. Middleton, K. Jacobs, W. Van der Stricht, C. Merlet, B. Gil, A. Vantomme and J. F. W. Mosselmans, *The Dependence of the Optical Energies on InGaN Composition*, Mat. Sci. Eng. B **82**, 194 (2001).

K. P. O'Donnell, R. W. Martin, M. E. White, K. Jacobs, W. Van der Stricht, P. Demeester, A. Vantomme, M. F. Wu and J. F. W. Mosselmans, *Optical Spectroscopy and Composition of InGaN*, Mat. Res. Soc. Symp. **595**, W11.26.1 (2000).

A. Vantomme, M. F. Wu, S. Hogg, G. Langouche, K. Jacobs, I. Moerman, M. E. White, K. P. O'Donnell, L. Nistor, J. Van Landuyt and H. Bender, *Comparative Study of Structural Properties and Photoluminescence in InGaN Layers with a High In Content*, MRS Internet J. Nitride Semicond. Res. **551**, W11.38 (2000).

K. P. O'Donnell, M. E. White, S. Pereira, M. F. Wu, A. Vantomme, W. Van der Stricht and K. Jacobs, *Photoluminescence Mapping and Rutherford Backscattering Spectrometry of InGaN Epilayers*, phys. stat. sol. (b) **216**, 171 (1999).

K. P. O'Donnell, C. Trager-Cowan, S. Pereira, A. Bangura, C. Young, M. E. White and M. J. Tobin, *Spectroscopic Imaging of InGaN Epilayers*, phys. stat. sol. (b) **216**, 157 (1999).

K. P. O'Donnell, R. W. Martin, M. E. White, J. F. W. Mosselmans and Q. Guo, *Extended X-ray Absorption Fine Structure (EXAFS) of InN and InGaN*, phys. stat. sol. (b) **216**, 152 (1999).

K. P. O'Donnell, R. W. Martin, S. Pereira, A. Bangura, M. E. White, W. Van der Stricht and K. Jacobs, *Intrinsic Infrared Luminescence from InGaN Epilayers*, phys. stat. sol. (b) **216**, 141 (1999).